

# UC San Diego

## UC San Diego Electronic Theses and Dissertations

### Title

Monolayer Stress Microscopy: Developing 3D, Elastographic, and High-Throughput Capabilities

### Permalink

<https://escholarship.org/uc/item/2bc3f7bc>

### Author

Serrano, Ricardo

### Publication Date

2018

Peer reviewed|Thesis/dissertation

UNIVERSITY OF CALIFORNIA SAN DIEGO

**Monolayer Stress Microscopy: Developing 3D, Elastographic, and  
High-Throughput Capabilities**

A dissertation submitted in partial satisfaction of the  
requirements for the degree  
Doctor of Philosophy

in

Engineering Sciences (Applied Mechanics)

by

Ricardo Serrano

Committee in charge:

Professor Juan Carlos del Álamo, Chair  
Professor Shengqiang Cai  
Professor Juan C. Lasheras  
Professor Vishal Nigam  
Professor Yingxiao Wang

2018

Copyright  
Ricardo Serrano, 2018  
All rights reserved.

The dissertation of Ricardo Serrano is approved, and it is acceptable in quality and form for publication on microfilm and electronically:

---

---

---

---

---

Chair

University of California San Diego

2018

## EPIGRAPH

*The secret of life, though, is to fall seven times  
and to get up eight times.*

— Paulo Coelho  
The Alchemist.

## TABLE OF CONTENTS

Signature Page . . . . .	iii
Epigraph . . . . .	iv
Table of Contents . . . . .	v
List of Figures . . . . .	vii
Acknowledgements . . . . .	ix
Vita . . . . .	xii
Abstract of the Dissertation . . . . .	xiv
Chapter 1 Introduction . . . . .	1
Chapter 2 Three-dimensional Monolayer Stress Microscopy . . . . .	5
2.1 Introduction . . . . .	5
2.2 Materials and Methods . . . . .	8
2.2.1 Micropatterned Polyacrylamide Gel Preparation . . . . .	8
2.2.2 Cell Culture . . . . .	9
2.2.3 Imaging . . . . .	10
2.2.4 Image Cross-Correlation for Deformation Measurement . . . . .	10
2.2.5 Traction Force Microscopy . . . . .	18
2.2.6 Equations of Mechanical Equilibrium in the Monolayer . . . . .	18
2.3 Results . . . . .	24
2.4 Discussion . . . . .	44
2.5 Appendix . . . . .	47
2.5.1 Implementation of Gradient Descent Method for Constrained PIV . . . . .	47
2.5.2 Derivation of analytical solutions for validation of the Lateral Problem . . . . .	51
2.5.3 Derivation of analytical solutions for validation of Bending Problem . . . . .	52
2.6 Acknowledgements . . . . .	54
Chapter 3 High-throughput phenotypical Screening of Force and Stifness of Cardiomyocytes . . . . .	55
3.1 Introduction . . . . .	55

3.2	Materials and Methods . . . . .	57
3.2.1	Fabrication of Polyacrylamide Gel Fabrication in 96-well format	57
3.2.2	Differentiation of hiPSCs to Cardiomyocytes . . . . .	58
3.2.3	Preparation of WGA Loading Solution and Benchmark Compounds . . . . .	58
3.2.4	Loading of WGA Dye Solution and Automated Image Acquisition . . . . .	60
3.2.5	Automated Quantification of Deformation in Polyacrylamide Gels . . . . .	61
3.2.6	Dynamic Monolayer Force Microscopy . . . . .	64
3.2.7	Cell Deformation Measurement and Contractility Signal . . .	64
3.2.8	Elastography . . . . .	66
3.3	Results . . . . .	69
3.3.1	Measurement of Drug Response Against Benchmark Compounds . . . . .	71
3.3.2	Comparison of Membrane and Substrate Deformation Measurements . . . . .	71
3.4	Discussion . . . . .	74
3.5	Appendix . . . . .	78
3.5.1	Implementation of Phase Average Algorithm for Parameter Retrieval . . . . .	78
3.5.2	Reconstruction of Phase Averaged Deformation Maps . . . .	79
3.6	User Guide For Contractility Analysis . . . . .	81
3.7	Acknowledgements . . . . .	93
Chapter 4	Concluding Remarks . . . . .	94
	Bibliography . . . . .	98

## LIST OF FIGURES

Figure 2.1:	Sketch of Monolayer Stress From Lateral and Bending Deformation . . .	6
Figure 2.2:	Illustration of the improvement gained by performing multigrid image correlation . . . . .	15
Figure 2.3:	Representation of a cell island in a discretized cartesian grid. . . . .	19
Figure 2.4:	Validation of the lateral problem . . . . .	26
Figure 2.5:	Validation of the bending problem . . . . .	29
Figure 2.6:	Experimental data of traction stresses and intracellular stress in a 45-micron radius cell island . . . . .	33
Figure 2.7:	Experimental data of traction stresses and intracellular stress in a triangular cell island of side 120 microns . . . . .	35
Figure 2.8:	Experimental data of traction stresses and intracellular stress in a 25-micron radius cell island . . . . .	37
Figure 2.9:	Experimental data of traction stresses and intracellular stress in a 65-micron radius cell island . . . . .	39
Figure 2.10:	Profiles representing the average value of: magnitude of tangential, normal traction stress, and intracellular tension due to lateral and bending; with respect to the distance to the edge in circular islands of different sizes.	41
Figure 2.11:	Profiles representing the standard deviation of: magnitude of tangential, normal traction stress, and intracellular tension due to lateral and bending; with respect to the distance to the edge in circular islands of different sizes. . . . .	42
Figure 3.1:	Protocol for the fabrication of a 96 well plate with polyacrylamide gels at the bottom. . . . .	59
Figure 3.2:	Overview of the contractility analysis method from substrate deformation data. . . . .	62
Figure 3.3:	Overview of the contractility analysis method from cell membrane data.	65
Figure 3.4:	Workflow describing crucial steps for elastography. . . . .	67
Figure 3.5:	Example of the intracellular tension fields generated by a point force located at two different edge points. . . . .	68
Figure 3.6:	Validation of the boundary correction method. . . . .	70
Figure 3.7:	Contractility signals, dose response curves, and heatmaps of hiPS-CMs treated with benchmark compounds. . . . .	72
Figure 3.8:	Contractility traces before (gray) and after (red) treatment with MYK-461. Dose concentrations increase by column (Baseline, 0.001 $\mu$ M, 0.01 $\mu$ M, 0.1 $\mu$ M, 1M, and 10M). . . . .	73



Figure 3.9: Contractility traces before (gray) and after (red) treatment with MYK-461. Dose concentrations increase by column (Baseline, 0.001 $\mu$ M, 0.01 $\mu$ M, 0.1 $\mu$ M, 1M, and 10M). . . . .	74
Figure 3.10: Correlation matrix across the metrics retrieved by the contractility analysis and the video analyzed (that of the substrate deformations from the beads images or the cell membrane deformations from the WGA stain). . . . .	75
Figure 3.11: Scatter (A) and Bland-Altman (B) plots, of bulk modulus times divergence ( $k * D$ ) against intracellular tension ( $IT$ ) for all the experiments before drug treatment, at the moment of maximum contraction. . . . .	76
Figure 3.12: Parameter retrieval algorithm for periodic contractility signals. . . . .	80
Figure 3.13: Example of results produced by synchronization algorithm. A) Reconstructed contractility peak signal. B) Maps of divergence at different stages of contraction cycle. . . . .	81
Figure 3.14: Main menu of CCA. . . . .	83
Figure 3.15: GUI to create a new job file. . . . .	84
Figure 3.16: Sample of Job File. . . . .	85
Figure 3.17: GUI to create a new configuration file. . . . .	86
Figure 3.18: Sample of Config File. . . . .	88
Figure 3.19: GUI to create an alias file. . . . .	89
Figure 3.20: Sample of alias file. . . . .	89
Figure 3.21: Main menu of CCA ready to start the analysis. . . . .	90
Figure 3.22: Example of a status file. . . . .	91
Figure 3.23: Example of CCA_results.csv . . . . .	92

## ACKNOWLEDGEMENTS

There are many individuals that I would like to thank for their contribution to the success of my Ph.D. I am grateful to say that this period of my life is ending positively, and that is all due to the incredibly valuable people that I have encountered.

I would like to thank Professor Antonio L. Sánchez for putting me in contact with Professor Juan Carlos del Álamo and Professor Juan C. Lasheras. Antonio widely opened the doors of research to me, and for that, I am thankful.

I would like to acknowledge Professor Juan C. Lasheras for his guidance and advice. His experience and ingenuity have shaped the work put into this dissertation.

There should also be a special mention made to Professor Juan Carlos del Álamo. His passion, intelligence, and curiosity are contagious. He has made me a better version of myself, but to only thank him for his academic contribution would be unfair. I am proud and grateful to have shared many moments with Juan Carlos ranging from an ordinary lunch at Price Center to climbing a 14,000 ft. mountain. It is difficult to be with him and not learn something new or inspired to do so.

I would also like to thank my labmates: Lorenzo, Josh, Shun, and Ernesto for the much-needed doses of humor and research help, Yi-Ting and Ruedi for teaching me what I know about the experimental aspects of our research, and many others including Ashish, Marissa, Effie, Toni, Kristen, María, Stephanie, Amy, and Cathleen. Thank you to all the lab members, past and present, for the environment that you have created. You make coming to work fun and inspiring.

To the many friends that I've made in San Diego - Nelson, Luis, Elynn, Brent, Scott, Hannah, Mike, Han Mee, David, Maggie, Alana, Oliver, Sunny, Sara, Paco, and everyone else- thank you for being there, you never fail to put a smile on my face.

To my group of friends in Spain -Edu, Gonzalo, Isa, Carlos, María, Andrea, Casandra, Lucía- no matter the distance and time, you make me feel supported and loved from the distance.

To Erin, for being the best partner one could ask for. This endeavor has been made

possible thanks to her support and ability to emit peace and calm. Erin knows best when to listen, when to crack a joke, and when to cry together. Your love is an infinite source of strength and happiness that has undoubtedly helped me through my Ph.D. and for that, my work is dedicated to you.

Finally, I would like to thank my family. Thanks to Rafa and Aurora, my siblings. From helping me with homework or giving me a ride, they were always there for everything and always gave without asking for in return. To my parents, thank you for being an example of sacrifice and hard work for our family. Their lives are an example of love and dedication. I can only aspire to make them proud and become like them in the future.

Chapter 2, in part, has been submitted for publication of the material as it may appear in *Biophysical Journal*, 2018, Serrano, Ricardo; Aung, Aereas; Lasheras, Juan C.; Varghese, Shyni; del Álamo, Juan C. The dissertation author was the primary author of this paper.

Chapter 3, in part is currently being prepared for submission for publication of the material. Serrano, Ricardo; McKeithan Wesley; Mercola, Mark; del Álamo, Juan C. The dissertation/thesis author was the primary investigator and author of this material.

## VITA

- 2012                      Graduado (B.S.) in Electronic Engineering and Automation,  
Universidad Carlos III de Madrid (Spain)
- 2013                      M.S. in Engineering Sciences (Applied Mechanics),  
University of California San Diego
- 2013 - 2018              Graduate Research Assistant,  
University of California San Diego
- 2013 - 2018              Teaching Assistant,  
University of California San Diego
- 2018                      Technology Management and Entrepreneurism fellowship pro-  
gram, Institute for the Global Entrepreneur,  
University of California San Diego
- 2018                      Ph.D. in Engineering Sciences (Applied Mechanics),  
University of California San Diego

## PUBLICATIONS

- Banerjee, Indroneal; Carrion, Katrina; Serrano, Ricardo; Dyo, Jeffrey; Sasik, Roman; Lund, Sean; Willems, Erik; Aceves, Seema; Meili, Rudolph; Mercola, Mark; Chen, Ju; Zambon, Alexander; Hardiman, Gary; Doherty, Taylor A.; Lange, Stephan; del Álamo, Juan C.; Nigam, Vishal, “Cyclic stretch of Embryonic Cardiomyocytes Increases Proliferation, Growth, and Expression While Repressing Tgf- $\beta$  Signaling”, *Journal of molecular and cellular cardiology.*, **79**, (2015)
- del Álamo, Juan C.; Lemons, Derek; Serrano, Ricardo; Savchenko, Alex; Cerignoli, Fabio; Bodmer, Rolf; Mercola, Mark, “High Throughput Physiological Screening of iPSC-Derived Cardiomyocytes for Drug Development”, *Biochimica et biophysica acta*, **1863** (2016).
- Lamason, Rebecca L.; Bastounis, Effie; Kafai, Natasha M.; Serrano, Ricardo; del Álamo, Juan C.; Theriot, Julie A.; Welch, Matthew D., “Rickettsia Sca4 Reduces Vinculin-Mediated Intercellular Tension to Promote Spread.” *Cell* **167** (2016).
- Sharma, Arun; Burridge, Paul W.; McKeithan, Wesley L.; Serrano, Ricardo; Shukla, Praveen; Sayed, Nazish; Churko, Jared M.; Kitani, Tomoya; Wu, Haodi; Holmström, Alexandra; Matsa, Elena; Zhang, Yuan; Kumar, Anusha; Fan, Alice C.; del Álamo, Juan C.; Wu, Sean M.; Moslehi, Javid J.; Mercola, Mark; Wu, Joseph C., “High-Throughput Screening of Tyrosine Kinase Inhibitor Cardiotoxicity with Human Induced Pluripotent Stem Cells.” *Science translational medicine* **9** (2017).

Yeh, Yi-Ting; Serrano, Ricardo; François, Joshua; Chiu, Jeng-Jiann; Li, Yi-Shuan Julie; del Álamo, Juan C.; Chien, Shu; Lasheras, Juan C., “Three-Dimensional Forces Exerted by Leukocytes and Vascular Endothelial Cells Dynamically Facilitate Diapedesis.” *Proceedings of the National Academy of Sciences of the United States of America* **115** (2018).

Serrano, Ricardo; Aung, Aereas; Lasheras, Juan C.; Varghese, Shyni; del Álamo, Juan C. “Three-Dimensional Monolayer Stress Microscopy”, (Submitted).

Serrano, Ricardo; McKeithan Wesley; Mercola, Mark; del Álamo, Juan C. “High-Throughput Functional Screening Assay of Force and Stiffness in iPSC Derived Cardiomyocytes”, (In preparation).

## ABSTRACT OF THE DISSERTATION

### **Monolayer Stress Microscopy: Developing 3D, Elastographic, and High-Throughput Capabilities**

by

Ricardo Serrano

Doctor of Philosophy in Engineering Sciences (Applied Mechanics)

University of California San Diego, 2018

Professor Juan Carlos del Álamo, Chair

The collective transmission of forces in multicellular colonies plays an important role in biological processes such as development, endothelial function and wound healing. The quantification of intracellular forces by monolayer stress microscopy (MSM) has improved our understanding of these phenomena, and provides great promise for the functional screening of contractile tissues in the context of drug development. However, current MSM methods present a number of limitations: they assume that the monolayer only deforms laterally, introduce boundary artifacts, and are restricted to low-throughput applications. This dissertation addresses these limitations and provides the first high-throughput quantification of three-dimensional (3D) intracellular stresses in applications relevant to biology and biotechnology, ranging from leukocyte extravasation to high-throughput functional screening of cardiomyocytes.

We introduce a 3D-MSM method that incorporates for the first time monolayer bending. 3D-MSM measures the 3D traction stresses exerted by the cells on a flexible substrate and calculates intracellular stresses by imposing equilibrium of forces and moments in the

monolayer. We present 3D-MSM measurements in micropatterned cell islands of different sizes and shapes. We show that intracellular stresses caused by lateral deformation are transmitted across long distances, whereas bending-induced stresses remain confined to 1-2 cell lengths from bending sites. We hypothesize that the localized effect of bending-induced stresses may be important in processes such as cellular extravasation, which are accompanied by large 3D deflections of the endothelium and require localized permeability changes. Overall, these results suggest that bending and lateral stresses can propagate mechanical signals at different length scales, and reveal that the transmission of forces across cell junctions is more three-dimensional and complex than previously believed.

We also present a novel high-throughput functional screening assay that quantifies cardiomyocyte force generation and stiffness changes during the cardiac cycle. The method jointly measures the intracellular stresses within cardiomyocyte monolayers and their elastic modulus. The main novelty of this method is that it utilizes the forces generated by the cells themselves to probe their material properties and is, thus, fully non-invasive. We present the proof-of-concept application of our method with dose-response measurements of a series of benchmark compounds tested on monolayers of hiPSC cardiomyocytes.



# Chapter 1

## Introduction

The transmission and orchestration of forces across a cell monolayer plays an important role in many key biological processes such as tissue morphogenesis, vascular homeostasis, and cell extravasation [1–3]. Throughout these events, cells interact mechanically with their environment by either exerting forces on the extracellular matrix (ECM), or a neighboring cell.

In the early 2000s, scientists developed Traction Force Microscopy (TFM) to study how single cells interact mechanically with the ECM [4, 5]. TFM has arguably become the golden standard procedure to measure traction stresses at the cellular level [6]. Its experimental application has deepened our understanding of a broad array of biological processes such as stem cell differentiation [7], cell locomotion [8], and cell adhesion [9]. Traction stresses have been shown to be dynamic and three dimensional [10, 11], and as of today, we are still discovering new ways traction forces interplay with cellular processes.

However, in a collective of cells, mechanical interactions not only occur at the cell-substrate interface -i.e. traction forces- but rather one must also consider cell-cell force transmission. Researchers have identified cell-cell forces as a driver for tissue morphogenesis [1], homeostasis [3], and mechanotransduction [12]. The spatial orientation and magnitude of traction stresses determines how forces are transmitted from one cell to another through their junctions, building up as intracellular stress similarly to how tension builds up on a rope during a tug-of-war game [13]. Given its relevance, several groups have tackled the

problem of quantifying and characterizing intracellular stress maps, giving rise to an array of different approaches.

Hur et al.[14] proposed a method to calculate intracellular stress at cell-cell junctions from a control volume approach. In summary, their method is based upon the fact that the junctional tension between cells must balance the net force arising from the traction stresses under one cell. The implementation of their method is straightforward and allows for the consideration of a three dimensional traction stress field. However, it does not provide stress maps that are spatially resolved. This approach allowed to find that the directionality and magnitude of intracellular stress transmission at endothelia cell junctions was modulated by their exposure to shear stress, which in turn, affected their susceptibility for atherogenesis.

Trepat et al. [15] proposed taking a differential formulation to the study of intracellular stress. Based on Kirchoff-Love theory, the monolayer is approximated to a thin layer of elastic material with uniform Young's Modulus and Poisson's ratio. Within that framework, one can establish a force balance between the traction force and change in intracellular stress on a differential element. This methodology, referred as Monolayer Stress Microscopy (MSM), yields maps of the stress tensor within the cell collective. In its first application, MSM served to reveal that the motion of a cell within a collective aligns with the direction of minimum shear.

A variety of other MSM methods have been proposed ever since. Zimmerman et al. [16] modeled the cells as particles that can exert forces on other particles according to a potential, and have used Hardy's stress formula [17] to infer the continuum stress distribution in the monolayer from the inter-particle forces. More recently, Nier et al. [18] proposed a Bayesian inference method to effectively replace explicit compatibility and boundary conditions by a set of sound assumptions about the symmetry and statistical noise of the intracellular stress tensor. These methods have been shown to yield results that are generally in good agreement, but, as of today, there are still many open challenges for MSM.

Current MSM methods work on the assumption that the cells forming the monolayer exert only two dimensional (2D) traction stresses. This assumption is however compromised in certain scenarios. For instance, during morphogenesis the developing tissue undergoes

a series of events like invaginations, folds, and tube formation [19]. These events occur in three dimensions (3D), resulting from 3D interactions of the cells with the ECM matrix and other cells. Even after development, the cells in our body are constantly exerting and sensing forces that are three dimensional. A remarkable example is leukocyte extravasation where the endothelial cell barrier undergoes significant out-of-plane deformation while the leukocyte is going through a small gap in the endothelial cell monolayer [20]. Chapter 2 of this thesis introduces the mathematical framework, and numerical solution of intracellular stress maps that arise from a 3D traction stress field.

MSM relies on the solution of a system of partial differential equations with their corresponding boundary conditions. We can prescribe physically realistic conditions for the intracellular stress in those areas where we see the edge of the monolayer -for instance the leading edge of a wound closing experiment or the perimeter around a micropatterned cell island. However, if the cell monolayer extends beyond the imaged region, we lack information about the state of the intracellular stress at that edge -i.e. we don't know how the forces coming from the cells outside the imaged region are influencing the region that we are observing. As a consequence, the boundary conditions are based on assumptions that, in turn, introduce artifacts in the recovered stress maps [21]. Chapter 2 of this dissertation describes a new way to incorporate boundary conditions in micropatterned cell islands, where the periphery of the monolayer is within the imaged region. Chapter 3 proposes a method for the correction of monolayer stress at the boundary combining traction force stress maps together with cell deformation measurements.

Techniques such as TFM and MSM present the potential to characterize mechanical phenotypes in high-throughput. High Content Screening systems have automatized to large extent the process of microscopy imaging, required to obtain data for TFM and MSM. However, there are two key missing elements for this adaptation to happen. The first one is that TFM/MSM require the cells to be seeded on a soft deformable substrate of known properties. Such substrates must contain some tracer -for instance fluorescent particles- that allow to measure the deformation of the substrate under the forces of the cells. Secondly, the software for TFM/MSM analysis must be user-friendly and adapted to work on large

batches of data so that non-experts can make use of these tools. Today, the solutions to these two issues are not perfect. There are commercially available multiwell plates (SoftTrac, Matrigen) with soft substrates -made out of polyacrylamide hydrogels- that are ready to be seeded with cells but at a price that prohibits their use in everyday experiments. There are TFM programs with a user friendly interface and good documentation but they do not offer to be run in batches [22]. As a consequence, force-based functional assays are far less used than their biochemistry counterparts. Chapter 3 describes a way to fabricate a 96 well device with hydrogels that can be used for TFM and MSM experiments, and that only requires instruments already present in many biology labs. In addition, we have developed software tools to automatize TFM and MSM experiments for large datasets. An example application of both the device and software is illustrated with dose-response curves of changes in force and dynamics of contractility in hIPS derived cardiomyocytes.

Another aspect of cell mechanics involves the measurement of the material properties of the cell. Cardiac diseases such as heart failure with preserved ejection fraction are being associated with myocardial stiffness [23]. Currently at the cellular level, the established methodologies for measuring cell material properties are atomic force microscopy [24] and magnetic tweezer rheology [25]. In these techniques the cells are mechanically probed at a very specific location, resulting in an invasive, low resolution and low-throughput procedure. At tissue level however, elastography methods [?] provide stiffness maps based on simultaneous knowledge of stress and strain maps of the material. Typically, sound waves are employed to exert a known force on the tissue while the resulting deformations are imaged either with MRI [26] or ultrasound [27]. Chapter 3 studies the relationship between simultaneous measurements of cell deformation and forces in hIPS cardiomyocytes. The main novelty of this method is that it employs the contractile forces of the cells themselves to probe their material properties. This method allows for the evaluation of the validity of the linear elasticity assumption in MSM and yields an estimate of the bulk modulus of the cells.

# Chapter 2

## Three-dimensional Monolayer Stress Microscopy

### 2.1 Introduction

Cells interact with their environment via biochemical and biophysical signals, including mechanical signals mediated by contractile forces [8]. When a cell contracts, it builds up intracellular stresses that can be transmitted to the extracellular matrix and to adjacent cells. This collective generation and transmission of intracellular stress in thin multicellular colonies plays an important role in biological processes such as development [28], endothelial function [29] and wound healing [30]. The development of microscopy methods for the measurement of intracellular stresses has improved our fundamental understanding of these biological processes [14, 15]. Furthermore, the high-throughput quantification of intracellular stresses provides great promise in the functional screening of contractile tissues for drug development [31, 32].

Monolayer Stress Microscopy (MSM) quantifies the spatial distribution of intracellular stress in confluent few-cell-thick cultures [14–16, 18, 31, 33]. Most MSM methods rely on a priori knowledge of the traction stresses that the cells exert on their substrate, which are conceptualized as loads acting on the monolayer by Newton’s third law [14, 15]. Several alternative models have been proposed to formulate the calculation of intracellular stresses in closed mathematical form. Pioneering MSM methods prescribed a compatibility condi-

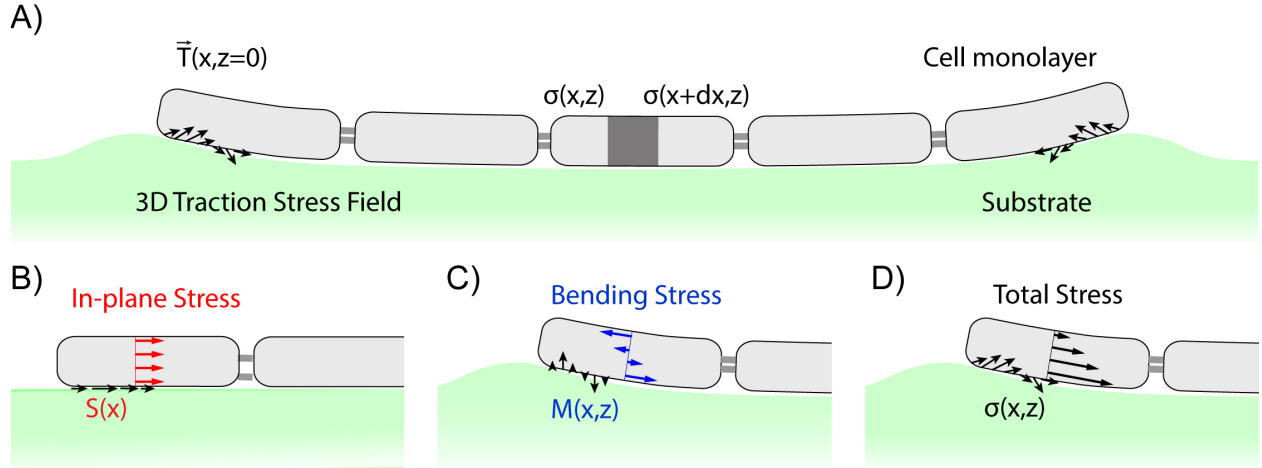


Figure 2.1: (A) Sketch of a cell monolayer exerting 3D traction stresses (arrows) on a deformable substrate. (B) Distribution of lateral stresses resulting from tangential component of traction stress. (C) Distribution of bending stresses resulting from normal component of traction stress. (D) The monolayer stress field is a combination of both lateral and bending effects.

tion consistent with a linearly elastic constitutive relation for the monolayer, as well as the boundary loads at the edges of the domain [15]. Subsequent efforts [16] have modeled cells in the monolayer as a set of particles that can exert forces on other particles according to a potential, and have used Hardy’s stress formula [17] to infer the continuum stress distribution in the monolayer from the inter-particle forces. More recently, Bayesian inversion has been proposed to effectively replace explicit compatibility and boundary conditions by a set of sound assumptions about the symmetry and statistical noise of the intracellular stress tensor [18]. These methods have been shown to yield results that are generally in good agreement, but they all neglect the contribution of bending moments and normal traction stresses.

A cell monolayer subjected to three-dimensional external loads can undergo bending due to the normal (i.e. out-of-plane) loads in addition to the lateral deformation caused by tangential (i.e. in-plane) loads ( Figure 2.1 A-C) [20, 34]. In principle, both the bending and the lateral deformations can cause intracellular stress (Figure 2.1 D). Existing MSM typically assume that the contribution to intracellular stress from bending and normal traction stresses is negligible. This assumption contrasts with experimental evidence that cell monolayers generate significant normal traction stresses [14, 35]. One of the arguments for neglecting

bending-induced stresses in cell monolayers is that the average stress across the thickness of the monolayer is zero [21]. This argument is based on the fact that internal stresses caused by bending in a thin plate of uniform mechanical properties vary linearly between  $-\sigma_{max}^{ben}$  and  $\sigma_{max}^{ben}$  across the plate thickness. However, the absolute value of these stresses may reach significant values. Additionally, the average stresses across monolayer thickness need not be zero if the mechanical properties of the monolayer are not uniform [36]. The relative contribution of bending to the total intracellular stress in cell monolayers has not been measured experimentally yet.

This paper has two main parts. The first part introduces a new MSM method that accounts for bending effects to derive the intracellular stresses in a cell monolayer from the three-dimensional (3D) traction stresses generated by the monolayer. In the second part, this new technique is applied experimentally to multicellular micro patterned islands of different sizes and shapes. Three-dimensional MSM infers the intracellular stresses caused by lateral deformation from the tangential traction stresses exerted by the cells on their substrate, while the intracellular stresses caused by monolayer bending are obtained from the normal traction stresses. The problem is formulated mathematically as a set of partial differential equations by modeling the cell monolayer as a thin linearly elastic plate, and by imposing equilibrium of forces and moments. The numerical integration of the equilibrium equations is carried out using a Fourier-Galerkin method, which allows for seamless integration with the 3D Fourier traction microscopy method used to measure the traction stresses at the interface between the cells and the substrate [37, 38]. An immersed interface method is used to apply the boundary conditions at the edges of the cell islands, which are defined implicitly using a level set function [39]. This numerical integration procedure is validated using the known analytical solutions of a family of synthetic deformation fields that is representative of our experimental measurements.

Our experimental results indicate that lateral intracellular stresses are collectively transmitted across long distances within the monolayer, consistent with previous observations [40]. They increase towards the inner side of the island until they reach a plateau value that is independent of island size. On the other hand, bending-induced intracellular

stresses are more concentrated spatially, and co-localize with sites of high normal deformation of the monolayer. The bending-induced intracellular stresses are particularly large at the edges of the cell islands, where they can exceed the intracellular stresses caused by lateral deformations. The effect of the localization of bending stresses might be relevant in processes like neutrophil extravasation or cancer cell invasion where a cell disrupts an endothelial monolayer locally by exerting forces that are normal to the monolayer and its substrate [20, 41, 42]. Overall, these results suggest that bending and lateral stresses can propagate mechanical signals at different length scales, and reveal that the transmission of forces across cell junctions is three-dimensional and more complex than previously believed.

## 2.2 Materials and Methods

### 2.2.1 Micropatterned Polyacrylamide Gel Preparation

Square #1 glass coverslips of 22-mm in size were activated with a drop of 0.1M NaOH on a plate at 90 °C until drop evaporation. The coverslips were then washed with distilled water, dried and treated with 3-aminopropyl-trimethoxysilane for 3 min. These coverslips were rinsed with distilled water, dried and treated with 0.5% glutaraldehyde for 30 min. The activated surfaces were rinsed with distilled water and kept at room temperature for their use within the same day. Round 12-mm glass coverslips were pretreated in a UV Ozone (UVO) box for 5 min. The coverslips were then incubated with a 110  $\mu$ L drop of 0.2 mg/mL PLL-PEG for 30 min at room temperature. The chrome face of the photomask (Advance Reproductions, North Andover, MA) was activated by UVO for 3 min. The PLL-PEG coated coverslips were attached to the activated side of the photomask by sandwiching a 2.5  $\mu$ L drop of distilled water between both surfaces. The assembly of the photomask and coverslips was then exposed to UVO light for 7 min. The photomask was detached from the coverslips by adding distilled water and then dried by aspirating excess water. A 110  $\mu$ L drop of 50  $\mu$ g/mL fibronectin (FN, Sigma-Aldrich, St. Louis, MO) was placed on the PLL-PEG coated surface of the coverslip and incubated for 40 mins. A thin film of FN was deposited on the areas of the coverslips that had been exposed to UVO light, whereas PLL-PEG prevented



FN adhesion to the glass surface in the shadowed areas [43].

The polyacrylamide gels were fabricated with a mixture of acrylamide and bis-acrylamide following a well-established method [10, 14, 38, 44–48]. Fluorescent 0.2  $\mu\text{m}$  diameter beads were added to the mixture for later use as fiduciary markers of gel deformation. To promote bead distribution towards the surface of the gel, phosphate-buffered saline (PBS) was used instead of distilled water. The Young’s modulus was controlled via the amount ratio of acrylamide and bis-acrylamide as previously described [49]. Once both coverslips were ready, freshly made 10% ammonium persulfate (APS) and tetramethylethylenediamine (TEMED) were added to the polyacrylamide and bis-acrylamide mixture to initiate gel polymerization. Immediately after, a 2.5  $\mu\text{L}$  drop of the mixture was put on the treated 22-mm square glass coverslip and topped with the FN patterned surface of the 12-mm round coverslip. The assembly was polymerized for 45 min before removing the round coverslip. The unpolymerized acrylamide was removed by rinsing twice with PBS. The resulting patterned gels were sterilized under 354 nm light for 5 min prior to adding the cells. The cells were seeded on top of the gels and allowed to adhere for 30 min. Unattached cells were washed off to avoid overgrowth of the patterns. The medium was reconstituted and the cells were incubated overnight until they reach confluency in the patterned regions.

### 2.2.2 Cell Culture

Human vascular umbilical endothelial vein cells (HUVECs) purchased from Lonza (Basel, Switzerland) were cultured on M199 supplemented with 10% (v/v) endothelial growth medium (Cell application, San Diego, California), 10% (v/v) FBS (Lonza), 1% sodium pyruvate, 1% L-glutamine and 1% penicillin-streptomycin (Gibco, Waltham, MA ). The cell plasma membranes were stained with CellMask (Thermo Fisher, Waltham, MA) to corroborate that the cells were forming an island of the desired size and shape.

### 2.2.3 Imaging

We acquired z-stacks of fluorescent images with 560-605 TRITC filter containing 40 planes with a separation of 0.2  $\mu\text{m}$  between planes. In addition, we acquired a 650-684 Cy5 image to confirm that the cells were restricted to the patterned area. For the acquisition, we used a confocal scanning microscope (Olympus IX81, Shinjuku, Tokyo, Japan) with a cooled CCD (Hamamatsu, Hamamatsu, Shizuoka, Japan) using Metamorph software (Molecular devices, Sunnyvale, California) and a 40 X NA 1.35 oil immersion objective. After image acquisition, the cells were detached using trypsin.

When imaging cell islands larger than the field of view of the microscope (i.e. 170 $\mu\text{m}$  x 170 $\mu\text{m}$ ), we acquired several stacks to cover the whole micro patterned area. A 20% overlap in x and y was used between neighboring stacks to facilitate a posteriori merging. Overlapping stacks were combined using the "Grid/Collection stitching" plug-in of ImageJ (NIH).

### 2.2.4 Image Cross-Correlation for Deformation Measurement

We measured the deformation of the substrate in three dimensions by cross-correlating each fluorescence z-stack with a reference z-stack in which the substrate was not deformed, similar to del Álamo et al [38]. The fluorescence z-stack in the deformed state was compared with a reference z-stack which was recorded at the end of experiment, after the cells were detached and the elastic substrate recovered its undeformed state. The comparison between the deformed and undeformed (reference) conditions was performed by dividing both z-stacks into 3D interrogation boxes and maximizing the cross-correlation between each pair of interrogation boxes. The accuracy of the image cross-correlation method used in del Álamo et al's [38] was refined here by introducing two improvements in their algorithm. First, we implemented the well-established multi-grid approach in which the correlation algorithm is run several times with interrogation boxes of progressively smaller sizes [50]. In this multi-grid approach, the results from each correlation pass are used to displace the interrogation box of the reference z-stack prior to image correlation. This method significantly increases the

overlap between deformed and reference interrogation boxes, and allows for using smaller interrogation boxes without compromising the signal-to-noise ratio, which increases the spatial resolution. Second, we adopted a novel variational approach to enforce the condition of global mechanical equilibrium of forces and moments. For a linearly elastic substrate, force equilibrium implies that the average of the measured deformation field must be zero in the x-y plane [5, 51]. This condition is typically enforced prior to recovering the traction stresses by subtracting the average value of the measured deformation, which can be non-zero due to image drift and other experimental noise sources. While this step effectively enforces global mechanical equilibrium, it modifies the measured deformation by the same value in all the interrogation boxes of each z-stack, regardless of local image quality in each box. A sounder approach consists of formulating the maximization of the cross-correlation function as a constrained optimization problem. At a given interrogation box with x-y coordinates given by indices  $i$  and  $j$ , the cost function of the problem is

$$J_{i,j} = C_{i,j}(u_x, u_y, u_z) + \frac{\lambda_x}{N_x N_y} \sum_{i=1}^{N_x} \sum_{j=1}^{N_y} u_{x_{i,j}} + \frac{\lambda_y}{N_x N_y} \sum_{i=1}^{N_x} \sum_{j=1}^{N_y} u_{y_{i,j}} + \frac{\lambda_z}{N_x N_y} \sum_{i=1}^{N_x} \sum_{j=1}^{N_y} u_{z_{i,j}}, \quad (2.1)$$

where  $C_{i,j}$  is the cross-correlation function between the deformed and undeformed interrogation boxes,  $u_x$ ,  $u_y$  and  $u_z$  are the displacement components in the x, y and z directions, and  $\lambda_x$ ,  $\lambda_y$  and  $\lambda_z$  are the Lagrange multipliers introduced to enforce that the spatial averages of  $u_x$ ,  $u_y$  and  $u_z$  are zero. To illustrate the method without loss of generality, we consider the one-dimensional case where

$$J_i = C_i(u_i) + \frac{\lambda}{N} \sum_{i=1}^N u_i \approx C_{0,i} - a_i (u_i - u_{0,i})^2 + \frac{\lambda}{N} \sum_{i=1}^N u_i, \quad (2.2)$$

where the rightmost side of the equation includes a quadratic polynomial fit to the correlation function used for sub-pixel interpolation, and  $u_{0,i}$  is the deformation value that would be obtained for each box without enforcing global equilibrium. In this polynomial fit, the constant  $C_{0,i}$  represents the maximum value of  $C_i(u_i)$ , whereas  $a_i > 0$  indicates its convexity. If the signal-to-noise ratio of the image within an interrogation box is low, then

$C_i(u_i)$  has a shallow peak and therefore  $a_i$  is small. Conversely, for interrogation boxes in regions of the image with high signal-to-noise, the correlation function has a sharp peak and the corresponding value of  $a_i$  is large. Minimizing  $J_i$  with respect to  $u_i$  yields

$$u_i = u_{0,i} + \frac{\lambda}{2Na_i}. \quad (2.3)$$

In order to find the value of the Lagrange multiplier, we enforce the global equilibrium condition  $\sum_{i=1}^N u_i = 0$ , which results in  $\lambda = -2N \sum_{i=1}^N u_{0,i} / \left( \sum_{i=1}^N a_i^{-1} \right)$ . Plugging this result into equation 3 provides the solution to the constrained optimization problem,

$$u_i = u_{0,i} - \frac{\frac{1}{a_i}}{\frac{1}{N} \sum_{i=1}^N \frac{1}{a_i}} \cdot \frac{\sum_{i=1}^N u_{0,i}}{N}. \quad (2.4)$$

This result differs from the conventional method of removing the average, i.e.  $u_i = u_{0,i} - \frac{\sum_{i=1}^N u_{0,i}}{N}$ , which applies the same correction to the displacement for all interrogation boxes. The variational approach proposed here applies a small correction in those interrogation boxes with higher signal-to-noise ratio, where  $1/a_i$  is smaller than its average value across the whole image,  $\frac{1}{N} \sum_{i=1}^N \frac{1}{a_i}$ . In the ideal case of an image of constant  $a_i$ , the variational approach becomes equivalent to removing the average deformation. It is important to note that the variational approach can be embedded into the sub-pixel interpolation routine and does not require additional calculations of the cross-correlation function. Thus, it does not imply a significant increase in image processing cost.

Equilibrium of moments can be enforced in a similar way by including additional Lagrange multipliers in the cost function. To illustrate the procedure, we consider the moment around the y-axis caused by normal stresses  $T_z$  over the whole field  $\Omega$ , which is

$$M_y = \int_{\Omega} x T_z(x, y) dx dy = 0. \quad (2.5)$$

In Fourier space, this equation becomes [5]

$$\hat{M}_y(k_x, k_y) = -\frac{i}{2} \frac{\partial \hat{T}_z(k_x, k_y)}{\partial k_x} \Big|_{(k_x, k_y)=(0,0)} \quad (2.6)$$

where  $\hat{M}_y$  and  $\hat{T}_z$  are the Fourier coefficients of  $M_y$  and  $T_z$ ,  $(k_x, k_y)$  is the wavenumber vector in the x and y directions, and  $i$  is the imaginary unit. The Fourier coefficient of the traction stresses is equal to the product between the coefficients of the measured deformation vector,  $\hat{\mathbf{u}}(k_x, k_y)$ , and the tensorial Green's function of the problem,  $G(k_x, k_y)$ . The latter were given in closed analytical form by del Álamo et al [38]. Using the chain rule of derivation, the moment equilibrium constraint can be expressed as

$$\hat{T}_x(k_x, k_y) = \hat{G}_z(k_x, k_y) \cdot \hat{\mathbf{u}}(k_x, k_y) \xrightarrow{\partial k_x|_{(k_x, k_y)=(0,0)}} \left. \frac{\partial \hat{T}_z}{\partial k_x} \right|_{0,0} = \left. \frac{\partial \hat{G}_z}{\partial k_x} \right|_{0,0} \cdot \hat{\mathbf{u}}(0,0) + \hat{G}_z(0,0) \cdot \left. \frac{\partial \hat{\mathbf{u}}}{\partial k_x} \right|_{0,0}. \quad (2.7)$$

Force equilibrium implies that  $\hat{\mathbf{u}}(0,0) = \mathbf{0}$ , so the first term in the right-hand side of this equation vanishes. Bringing the remaining term back into physical space, we obtain the following expression for the spatial average of the y-moment,

$$M_y = \frac{(1-\nu)E}{(1+\nu)(1-2\nu)h} \int_{\Omega} x u_z(x, y) dx dy, \quad (2.8)$$

where  $u_z$  represents the normal deformation and  $G_{zz}(0,0) = \frac{(1-\nu)E}{(1+\nu)(1-2\nu)h}$  is the only non-zero term of the Green's function for  $T_z$  [38]. The above expression allows us to compute  $M_y$  directly from the measured deformation without having to solve for the traction force field. This is convenient in order to impose the constrain  $M_y = 0$  in our variational method via an additional constraint,

$$\frac{\mu_{zx}}{N_x N_y} \sum_{i=1}^{N_x} \sum_{j=1}^{N_y} x_{i,j} u_{z,i,j}, \quad (2.9)$$

where  $\mu_{zx}$  is the corresponding Lagrange multiplier. The same reasoning can be followed to calculate all the contributions to the x and y moments from all the components of the measured deformation vector. Adding Lagrange multipliers to enforce that all these contributions are zero leads to the following cost function:

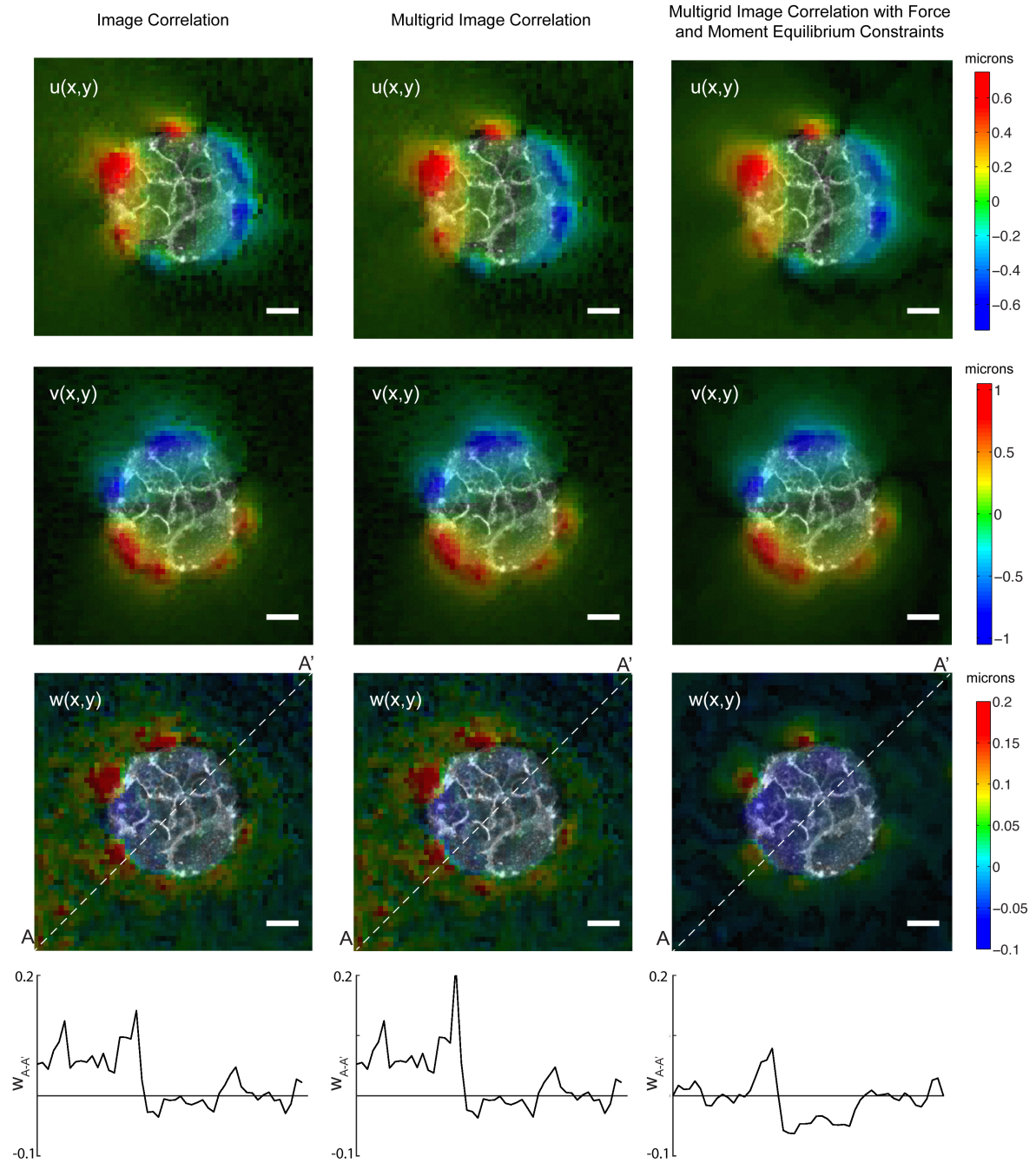
$$\begin{aligned}
J_{i,j} = & C_{i,j}(u_x, u_y, u_z) + \frac{\lambda_x}{N_x N_y} \sum_{i=1}^{N_x} \sum_{j=1}^{N_y} u_{x_{i,j}} + \frac{\lambda_y}{N_x N_y} \sum_{i=1}^{N_x} \sum_{j=1}^{N_y} u_{y_{i,j}} \\
& + \frac{\lambda_z}{N_x N_y} \sum_{i=1}^{N_x} \sum_{j=1}^{N_y} u_{z_{i,j}} + \frac{\mu_{xy}}{N_x N_y} \sum_{i=1}^{N_x} \sum_{j=1}^{N_y} y_{i,j} u_{x_{i,j}} + \frac{\mu_{yx}}{N_x N_y} \sum_{i=1}^{N_x} \sum_{j=1}^{N_y} x_{i,j} u_{y_{i,j}} \\
& + \frac{\mu_{zx}}{N_x N_y} \sum_{i=1}^{N_x} \sum_{j=1}^{N_y} x_{i,j} u_{z_{i,j}} + \frac{\mu_{zy}}{N_x N_y} \sum_{i=1}^{N_x} \sum_{j=1}^{N_y} y_{i,j} u_{z_{i,j}},
\end{aligned} \tag{2.10}$$

This cost function was minimized numerically using a gradient descent method in MATLAB (Mathworks, Natick, MA). See Appendix for a more detailed explanation.

Figure 2.2 compares substrate deformations obtained by standard image correlation, multigrid image correlation, and variational image correlation with force and moment equilibrium constraints. Representative examples obtained for two different island sizes (50- and 90-micron diameter) are shown. Of note, the lateral deformations ( $u$ ,  $v$ ) obtained by standard correlation have discontinuities in some regions, which appear as "holes" or sharp changes in the sign of the deformation. These regions are indicated by arrows in Figure 2.2 and coincide with locations of large  $u$  and  $v$ , where a significant fraction of the fluorescent markers in each interrogation box move beyond the boundaries of the box as the substrate is deformed. Consequently, standard image correlation yields spurious results in these regions, whereas multigrid image correlation is able to better capture the large motion of the markers by progressively resizing and displacing the interrogation boxes. Additionally, both the standard and multigrid image correlation methods yield appreciable tilt in the normal deformation ( $w$ ), which is evidenced by non-zero values of  $w$  outside and far from the edges of the cell islands and also in the profiles of normal deformation ( $w$ ) along the cross-section denoted by the white dashed line. Figure 2.2 shows that these artifacts disappear if the correlation between the deformed and deformation-free reference image stacks is maximized subject to force and momentum equilibrium constraints.

Figure 2.2: Illustration of the improvement gained by performing multigrid image correlation (center columns) and multigrid image correlation with force and momentum equilibrium constraints (right columns) compared to standard image correlation (left columns) for (A) a 50-micron diameter island and (B) a 90-micron diameter island. The measured displacement components in the x-direction  $U$ , y-direction  $V$ , and z-direction  $W$  are shown as first, second, and third rows respectively. The fourth row represents a side view of the measured  $W$  displacement along the line A-A' (white dashed line in third row).

# A) 45-micron island





## B) 65-micron island

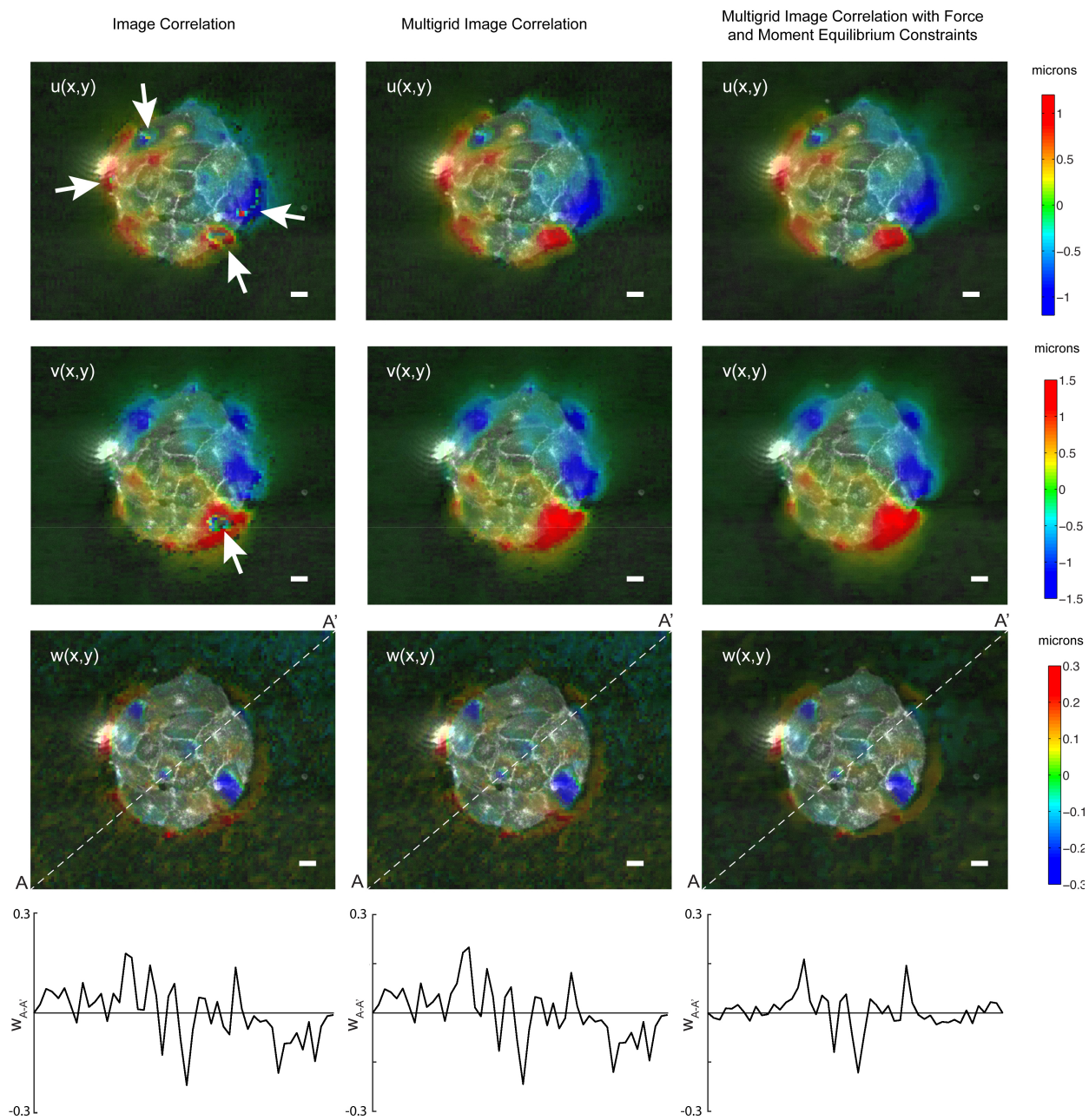


Figure 2.2: Illustration of the improvement gained by performing multigrid image correlation (center columns) and multigrid image correlation with force and momentum equilibrium constraints (right columns) compared to standard image correlation (left columns), continued.

## 2.2.5 Traction Force Microscopy

The 3D deformation of the PA substrate was measured at its top surface on which the cells were attached, following the method described above. Using these measurements as boundary conditions, we computed the three-dimensional deformation field in the whole polyacrylamide substrate by solving the elasto-static equation as previously described [38]. We then computed the traction stress vector exerted by the cells on the substrate,  $\bar{\mathbf{T}} = (T_x, T_y, T_z)$ . The spatial resolution of  $\bar{\mathbf{T}}$  was 2.7  $\mu\text{m}$ .

## 2.2.6 Equations of Mechanical Equilibrium in the Monolayer

### Lateral Deformation Problem:

The computation of the intracellular stresses induced by lateral deformation follows the mathematical model formulated by Tambe et al [21]. The monolayer is assumed to be a thin, linearly elastic plate of uniform thickness  $h$  and Poisson ratio  $\nu$ . We use a coordinate system in which the  $x$  and  $y$  directions are parallel to the monolayer plane, while  $z \in [-h/2, h/2]$  denotes the distance across the monolayer thickness (Figure 2.1 A). Static equilibrium of forces in  $x$  and  $y$  yields

$$\nabla_{2D} \cdot \bar{\bar{\Sigma}} - h^{-1} \bar{\mathbf{T}}_{2D} = \bar{\mathbf{0}} \quad (2.11)$$

in the domain  $\Omega$  occupied by the monolayer. In this equation, the tensor  $\bar{\bar{\Sigma}} = \begin{bmatrix} \sigma_{xx} & \sigma_{xy} \\ \sigma_{xy} & \sigma_{yy} \end{bmatrix}$  represents the intracellular stress induced by the lateral deformation of the monolayer, and the vector  $\bar{\mathbf{T}}_{2D} = (T_x, T_y)$  represents the tangential traction stresses at the interface between the cell monolayer and the substrate. The problem is closed via the Michel-Beltrami compatibility condition for continuity of deformation,

$$\nabla_{2D}^2 (\sigma_{xx} + \sigma_{yy}) = (1 + \nu)^{-1} \nabla \cdot \bar{\mathbf{T}}_{2D}. \quad (2.12)$$

Researchers are often interested in computing just the intracellular tension induced

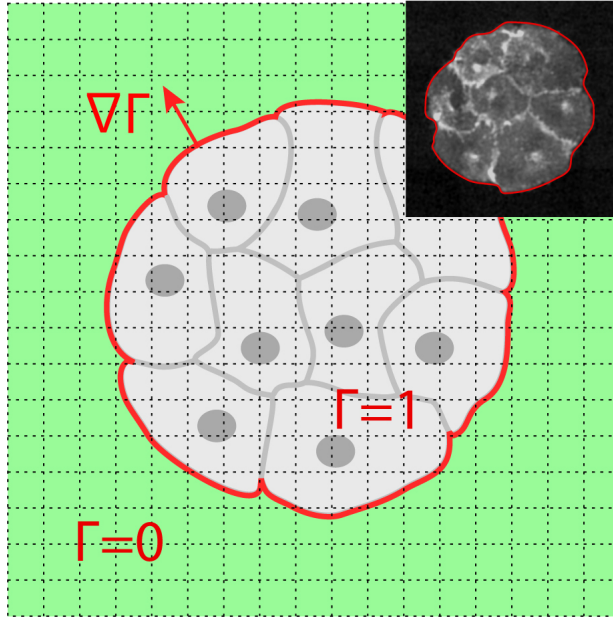


Figure 2.3: Representation of a cell island (gray) in a discretized cartesian grid. The red line represents the edge of the monolayer that separates the interior of the island  $\Gamma = 1$ , from the outside  $\Gamma = 0$ .  $\nabla\Gamma$  is defined as a unitary normal vector pointing outside of the cell domain. Inset: example of the specified outline (red) in an experiment.

by in-plane monolayer deformation, i.e. the first invariant of  $\bar{\bar{\Sigma}}$  defined as  $\Sigma = \text{trace}(\bar{\bar{\Sigma}}) = \sigma_{xx} + \sigma_{yy}$ , instead of the whole intracellular stress tensor [52, 53]. In that case, the Michel-Beltrami condition provides with a scalar Poisson equation to compute  $\Sigma$  from the traction stresses in an inexpensive manner. Stress-free boundary conditions are prescribed at the edge of the cell aggregate (Figure 2.3),

$$\bar{\bar{\Sigma}} \cdot \bar{\mathbf{n}} = \Sigma_s \bar{\mathbf{s}} + \Sigma_n \bar{\mathbf{n}} = \bar{\mathbf{0}} \quad (2.13)$$

where  $\bar{\mathbf{n}}$  and  $\bar{\mathbf{s}}$  are respectively unit vectors normal and tangential to the edge of the monolayer, and  $\Sigma_n$  and  $\Sigma_s$  are the normal and tangential components of the stress vector. This boundary condition implies that  $\Sigma_n = \Sigma_s = 0$ .

## Bending Problem.

In a uniform thin elastic plate subject to both lateral deformation and bending, the intracellular tension is given by

$$IT(x, y, z) \equiv \frac{\Sigma(x, y)}{h} + \frac{12M(x, y)}{h^2} \frac{z}{h} \quad (2.14)$$

According to this expression, the intracellular tension caused by lateral deformation is constant across the shell thickness and proportional to  $\Sigma$ . In addition, bending has a contribution that varies linearly with  $z$  and is proportional to the moment function  $M = \text{trace}(\bar{\mathbf{M}})/(1 + \nu)$ , where  $\bar{\mathbf{M}} = \begin{bmatrix} M_{xx} & M_{xy} \\ M_{xy} & M_{yy} \end{bmatrix}$  is the bending moment tensor [34]. To compare the magnitudes of the intracellular stresses caused by lateral deformation and by bending, it is useful to rewrite the above equation as

$$IT(x, y, z) = IT_{xy}(x, y) + IT_z(x, y) \cdot \frac{4z}{h} \quad (2.15)$$

where  $IT_{xy}$  are the intracellular stresses caused by lateral deformation, and

$$IT_z(x, y) = \frac{2}{h} \int_0^{\frac{h}{2}} \frac{12M(x, y)}{h^2} \frac{z}{h} dz = -\frac{2}{h} \int_{-\frac{h}{2}}^0 \frac{12M(x, y)}{h^2} \frac{z}{h} dz \quad (2.16)$$

Thus,  $IT_z(x, y) = 3M(x, y)/h^2$  represents the average magnitude of the bending-induced intracellular stresses across the top and bottom halves of the shell. The calculation of  $IT_z$  is based on the equation of mechanical equilibrium of bending moments [34],

$$\nabla_{2D}^2 M + T_z = 0, \quad (2.17)$$

which relates the bending-induced intracellular tension to the normal traction stresses. The boundary conditions for this Poisson equation are obtained by imposing zero effective transverse shear stress ( $V_n = \partial_n M + \partial_s M_{sn} = 0$ ), and zero twisting moment ( $M_{sn} = 0$ ) at the free edge of the monolayer [54]. These edge constraints are expressed mathematically as a homogeneous Neumann condition,  $\partial_n M = 0$ , since the zero-twist condition implies that the

tangential derivative of  $M_{sn}$  is zero along the free edge of the monolayer. For this Neumann boundary condition to be compatible with the Poisson equation (17), the cell monolayer must be in equilibrium of normal forces. Integrating (17) over the domain  $\Omega$  occupied by the cells, and applying Gauss' divergence theorem, we obtain

$$\int \int_{\Omega} T_z dx dy = \oint_{\partial\Omega} \partial_n M ds = 0, \quad (2.18)$$

where  $ds$  is an element of line along the boundary of the cell domain,  $\partial\Omega$ , and we have taken advantage of the fact that the closed-line integral  $\oint_{\partial\Omega} \partial_n M ds$  is zero. This result implies that the bending problem is not solvable unless  $T_z$  has zero average in the cell domain, and underlines the relevance of variational image correlation methods that enforce global mechanical equilibrium of forces and moments (see section 2.4).

### Numerical implementation of boundary conditions at the edges of the monolayer

A level-set immersed interface method was used to enforce the boundary conditions at the edges of the monolayer [39]. This procedure allows for the numerical implementation of boundary conditions on arbitrary geometries while keeping a uniform Cartesian grid, which facilitates the discretization of the MSM equations by Fourier expansions. The Fourier discretization is computationally efficient and makes MSM interface easily with previous Fourier traction force microscopy methods [5, 37, 38, 48, 55, 56]. In the immersed interface method, the geometry of the cell monolayer is defined implicitly through the introduction of a level set function,  $\Gamma(x, y)$ , that takes different values the interior and exterior of the monolayer. In our calculations, we used a Heaviside function with  $\Gamma = 1$  inside  $\Omega$  and  $\Gamma = 0$  outside  $\Omega$  (Figure 2.3) to augment the equation of tangential force balance as follows

$$\nabla_{2D} \cdot \left( \Gamma \bar{\bar{\Sigma}} \right) - \Gamma h^{-1} \bar{\mathbf{T}}_{2D} = \bar{\mathbf{0}}. \quad (2.19)$$

Considering that  $\nabla\Gamma = \delta(\partial\Omega) = \bar{\mathbf{n}}$  where  $\delta$  represents a Dirac Delta and  $\partial\Omega$  represents the boundary of the cell monolayer, the previous equation is equivalent to

$$-\Gamma \left[ \nabla_{2D} \cdot \bar{\bar{\Sigma}} - h^{-1} \bar{\mathbf{T}}_{2D} \right] + \delta(\partial\Omega) \bar{\bar{\Sigma}} \cdot \bar{\mathbf{n}} = \bar{\mathbf{0}}. \quad (2.20)$$

The first term in the left-hand side of this equation imposes tangential force balance in the region defined by  $\Gamma(x, y) = 1$ , i.e. inside the cell aggregate domain  $\Omega$ . The second term imposes a stress-free boundary condition at the edge of cell aggregate, where  $\delta(\partial\Omega)$  is non-zero. Note that because  $\Omega$  and  $\partial\Omega$  do not intersect, equation 20 independently imposes tangential force balance and the boundary conditions for the cell aggregate.

The bending problem can be treated in a similar manner, leading to the augmented equation

$$\nabla \cdot (\Gamma \nabla M) + T_z \Gamma = 0 \quad (2.21)$$

which is equivalent to

$$\Gamma \left[ \nabla^2 M + T_z \right] + \delta(\partial\Omega) \nabla M \cdot \bar{\mathbf{n}} = 0, \quad (2.22)$$

thereby recovering the equilibrium partial differential equation inside the cell aggregate and imposing the zero-shear-force condition,  $\nabla \Gamma \cdot \nabla M = \partial_n M = 0$ , at the edge of the aggregate.

## Numerical Integration

The system of augmented equations of static equilibrium (2.19, 2.21) is linear but has spatially varying coefficients, which complicates solving it using a Fourier Galerkin approach (i.e. projecting the equations onto each Fourier mode to obtain an almost-diagonal linear system of equations). To overcome this difficulty, the system was solved iteratively using a dynamic relaxation technique [57]. In this approach, the equations are reformulated to represent the time-dependent dynamics of a vibrating shell, and are marched in time until the steady state corresponding to static equilibrium is reached. The dynamical relaxation equation for the lateral problem reads

$$\Gamma [\rho \partial_{tt} \bar{\mathbf{U}} - (k + \mu \nabla_{2D}^2) \partial_t \bar{\mathbf{U}}] = \nabla_{2D} \cdot (\Gamma \bar{\bar{\Sigma}}) - \Gamma h^{-1} \bar{\mathbf{T}}_{2D}, \quad (2.23)$$

where  $\bar{\mathbf{U}}$  is the lateral deformation field of the cell monolayer,  $\rho$  is an arbitrary density, and a damping term with constants  $k$  and  $\mu$  is introduced to accelerate convergence. Upon convergence, all time derivatives are zero, recovering the equations of static equilibrium and boundary conditions for the cell monolayer (19). Using the definition of strains as a function of the deformation and Hooke's law, the time-dependent equation (23) can be recast as

$$\Gamma [\partial_{tt} \sigma_{xx} - (k + \mu \nabla_{2D}^2) \partial_t \sigma_{xx}] = A(\partial_x, \nu \partial_y) \cdot [\nabla_{2D} (\bar{\bar{\Sigma}} \Gamma) - \Gamma h^{-1} \bar{\mathbf{T}}_{2D}] \quad (2.24)$$

$$\Gamma [\partial_{tt} \sigma_{yy} - (k + \mu \nabla_{2D}^2) \partial_t \sigma_{yy}] = A(\nu \partial_x, \partial_y) \cdot [\nabla_{2D} (\bar{\bar{\Sigma}} \Gamma) - \Gamma h^{-1} \bar{\mathbf{T}}_{2D}] \quad (2.25)$$

$$\Gamma [\partial_{tt} \sigma_{xy} - (k + \mu \nabla_{2D}^2) \partial_t \sigma_{xy}] = B(\partial_y, \partial_x) \cdot [\nabla_{2D} (\bar{\bar{\Sigma}} \Gamma) - \Gamma h^{-1} \bar{\mathbf{T}}_{2D}] \quad (2.26)$$

which only depend on the lateral stress tensor  $\bar{\bar{\Sigma}}$ , and where  $A = (1 - \nu^2)^{-1}$  and  $B = -2(1 + \nu)^{-1}$ . The bending problem is treated in a similar manner, which yields the relaxation equation

$$\partial_t M = -(\nabla \cdot (\Gamma \nabla M) - T_z \Gamma). \quad (2.27)$$

The minus sign in front of the right-hand-side of the equation does not affect the final solution upon convergence but it is necessary to keep the iteration numerically stable. Equations (23-27) were discretized in a rectangular domain large enough so that the edges of the monolayer were separated at least 60  $\mu\text{m}$  from edges of the image, using a Cartesian grid with inter node spacing  $\Delta x = \Delta y = 2.7 \mu\text{m}$ . The discretized dynamic relaxation equations were advanced in time using an explicit Euler integration scheme until the solution changed by less than 5% between consecutive iterations. As initial condition for the iteration, we used the solution obtained without immersed boundary forcing (i.e.  $\Gamma = 1$  for the whole computational domain), which can be easily obtained by the Galerkin method. As is customary in level-set methods [58], we used a smeared-out Heaviside indicator function instead

of the sharp one in our numerical routines, in order to avoid spurious numerical oscillations in the results. Specifically, we convolved  $\Gamma$  with a Gaussian filter of width  $\Delta$  equal to a few pixels wide. The precise value of  $\Delta$  was chosen in each case to minimize the error of the solution based on our validation results, shown below.

## 2.3 Results

This section presents the results from validation analyses and experimental measurements of monolayer tension induced by 3D traction stresses in monolayer islands of varying shapes and sizes. We use islands because the boundary conditions at the free edge of a monolayer can be prescribed based on first principles, as described in the Methods section above. In experiments where the cell monolayer extends beyond the experimental field of view, the conditions at the edge of the computational domain are unknown. While it is possible to overcome this limitation by different approaches [18, 59] these approaches are beyond the scope of the present work. Micropatterning extracellular matrix proteins onto the substratum provides a robust way to culture cell islands within a region of tunable size and shape [60]. Furthermore, this methodology allows for repeatable geometric conditions, thus facilitating the statistical analysis of the experimental data.

### Validation

We validated the numerical discretization and integration methods presented above for a plate under the synthetic tangential load

$$T_r = T_0 x^2 (1 - x^\alpha), \quad (2.28)$$

which resembles our experimental measurements of the traction stress under circular cell monolayer islands. In the above equation,  $x = r/R$  is the distance to the center of the island normalized by island radius ( $R$ ), and  $T_0$  is a characteristic stress. The parameter  $\alpha \geq 1$  defines the width of the ring at edge of the cell island where the traction stresses are concentrated (see Figure 2.4 A). This width can be quantified by the length scale  $\lambda_\alpha =$



$\int_0^1 T_r(x, \alpha) dx / \max_x [T_r(x, \alpha)]$ , which is shown to decrease with  $\alpha$  in the inset of Figure 2.4 A.

In this axially symmetric case, the lateral elastic equilibrium and compatibility equations are reduced to

$$\partial_r \sigma_{rr} + \frac{1}{r} (\sigma_{rr} - \sigma_{\theta\theta}) = T_r \quad (2.29)$$

$$\partial_r [r \partial_r (\sigma_{rr} + \sigma_{\theta\theta})] = (1 + \nu) \partial_r (r T_r), \quad (2.30)$$

where  $\sigma_{rr}$  and  $\sigma_{\theta\theta}$  are the diagonal elements of the lateral stress tensor expressed in polar coordinates. The exact analytical solution to these equations is

$$\sigma_{rr} = T_0 R [A(\alpha, \nu)(x^3 - 1) + B(\alpha, \nu)(x^{3+\alpha} - 1)], \quad (2.31)$$

$$\sigma_{\theta\theta} = T_0 R [C(\alpha, \nu)x^3 + D(\alpha, \nu)x^{3+\alpha} + E(\alpha, \nu)], \quad (2.32)$$

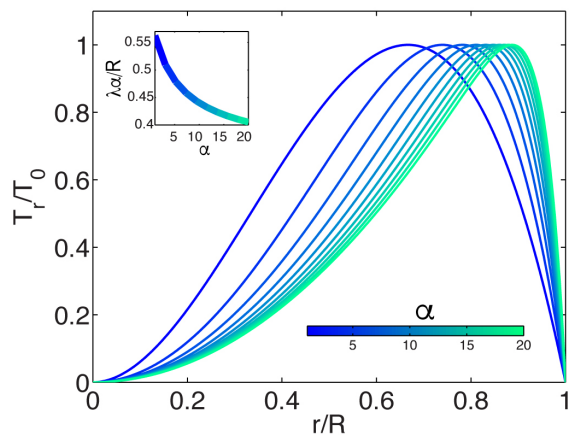
where the coefficients  $A(\alpha, \nu)$ ,  $B(\alpha, \nu)$ ,  $C(\alpha, \nu)$ , and  $D(\alpha, \nu)$  are given in the Appendix, together with the derivation of the solution. We determined the difference between the monolayer tension recovered from  $T_r$  using the procedures described in sections 2.6–2.8 above, and the exact monolayer tension obtained analytically. The difference is integrated over the cell island domain and normalized by the integral of the exact tension to yield the relative error:

$$Err_s \equiv \left[ \int \int |(\sigma_{rr} + \sigma_{\theta\theta})_{\text{recovered}} - (\sigma_{rr} + \sigma_{\theta\theta})_{\text{exact}}| dx dy \right] \cdot \left[ \int \int |(\sigma_{rr} + \sigma_{\theta\theta})_{\text{exact}}| dx dy \right]^{-1}. \quad (2.33)$$

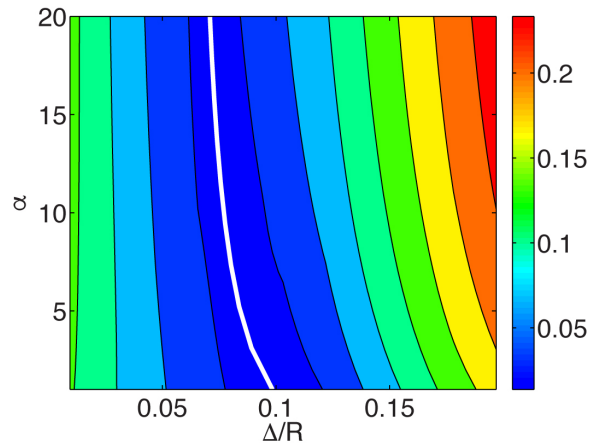
This error is plotted in Figure 2.4 B as a function of the width of the low-pass filter used to smooth the Heaviside level-set function,  $\Delta$ , and the parameter  $\alpha$  that defines the sharpness of the input distribution of tangential traction stresses. The data indicate that,

Figure 2.4: Validation of the lateral problem. (A) Profiles of the tangential traction stress load used to validate 3DMSM as a function of the width of the ring  $\alpha$  where traction forces are concentrated. Inset: lengthscale of the width of the ring  $\lambda_\alpha$  as a function of  $\alpha$  (B) Average error 3DMSM in the simulation as a function smoothness of  $\Gamma$  and width of the ring,  $\alpha$  (C) Example of a traction stress map for the particular case  $\alpha = 9$ . (D) Error, (E) analytical and (F) numerical solution for the lateral intracellular stress.

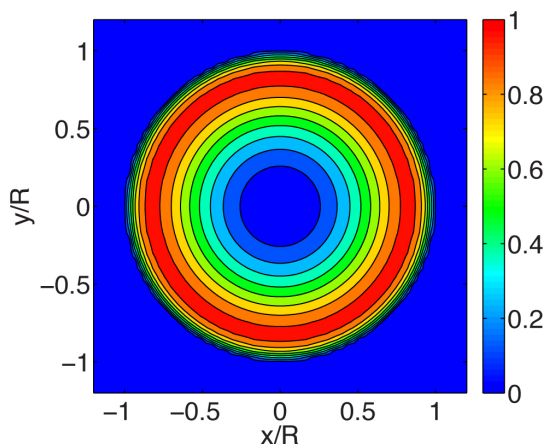
A) Lateral Forcing vs  $\alpha$



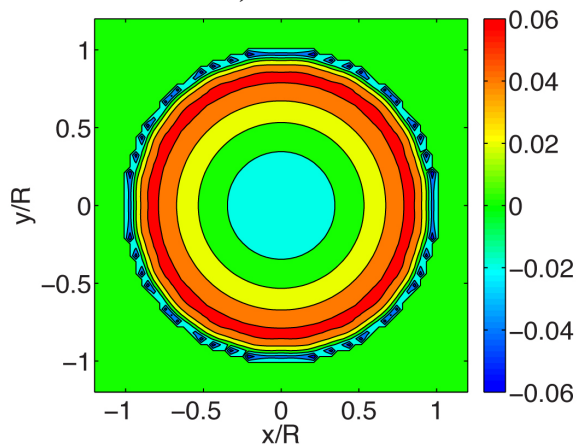
B) Monolayer Tension Relative Error



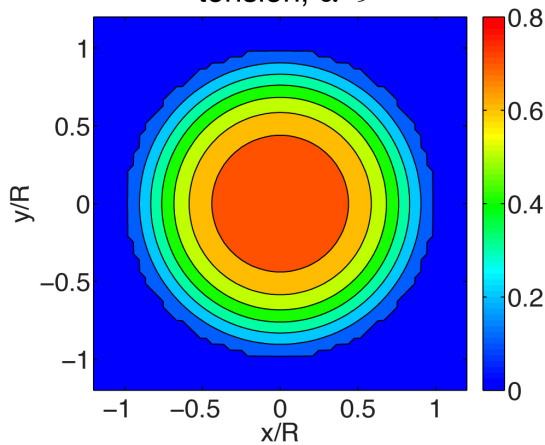
C) Lateral Forcing  $\alpha=9$



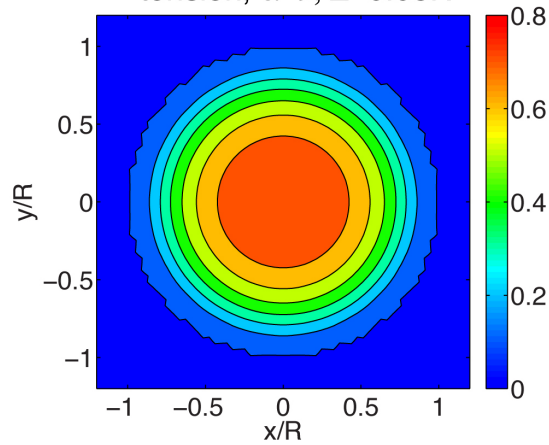
D) Monolayer tension Error  $\alpha=9, \Delta=0.08R$



E) Exact Monolayer tension,  $\alpha=9$



F) Recovered Monolayer tension,  $\alpha=9, \Delta=0.08R$



while the relative error is fairly independent of  $\alpha$ , it is more sensitive to the filter width  $\Delta$ . The dependence of the error with  $\Delta$  can be understood considering that  $\Delta$  tends to zero the level set function becomes infinitely sharp, leading to spurious numerical oscillations in the results (Gibbs error) [58]. Conversely, if the filter is too wide it artificially smooths out the solution, which is manifested by an increase in the error. The optimal filter width is  $\Delta \approx 0.18\lambda_\alpha$  (white line in Figure 2.4 B), which corresponds to approximately 20% the spatial extent of the tangential traction stresses, and yields an error below 5%. This result allowed us to adjust the numerical routines in each specific experiment, since  $\lambda_\alpha$  can be determined from the measured traction stresses without difficulty.

Figure 2.4 also includes detailed results from a particular case corresponding to  $\alpha = 9$ . The spatial distributions of the forcing traction stress and the absolute error in the monolayer tension are represented in Figures 2.4 C and D, respectively. These data indicate that the error co-localizes with the forcing stresses. However, this error is small ( $< 6\%$ ) and the spatial distributions of exact and numerically recovered monolayer tension are barely distinguishable (Figure 2.4 E,F). We used the same approach to validate our procedure to calculate the bending monolayer tension. We considered a circular cell monolayer island under the normal traction stress:

$$T_z = T_0 x^2 (1 - x^\alpha) \left( x^\alpha - \frac{2}{2 + \alpha} \right), \quad (2.34)$$

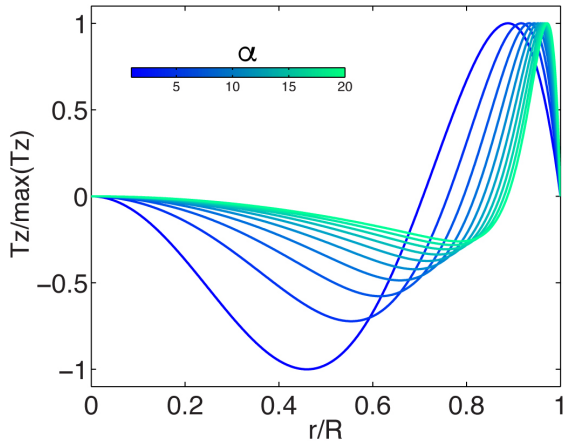
where the parameter  $\alpha \geq 1$  again defines how concentrated the traction stresses are near the edge of the island. This synthetic traction stress distribution is shown in Figure 2.5 A. It resembles the normal traction stresses measured in our experiments and satisfies global equilibrium of forces and moments, particularly of bending moments. The governing equation for this axially symmetric problem is

$$\partial_{rr} M + \frac{1}{r} \partial_r M = T_z, \quad (2.35)$$

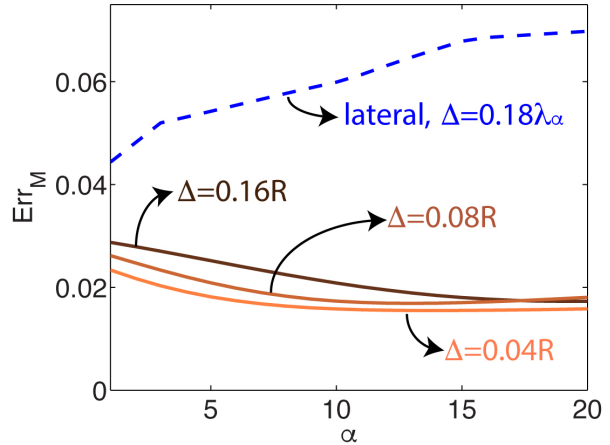
and the boundary condition is  $\partial_r M|_{r=R} = 0$ . The exact analytical solution to this problem is

Figure 2.5: Validation of the bending problem. (A) Profiles of the normal traction stress load used to validate 3DMSM as a function of the width of the ring  $\hat{I}\hat{s}$  where traction forces are concentrated. (B) Average error 3DMSM in the simulation as a function smoothness of  $\Gamma$  and width of the ring,  $\alpha$  (C) Example of a traction stress map for the particular case  $\alpha = 9$ . (D) Error, (E) analytical and (F) numerical solution for the bending intracellular stress.

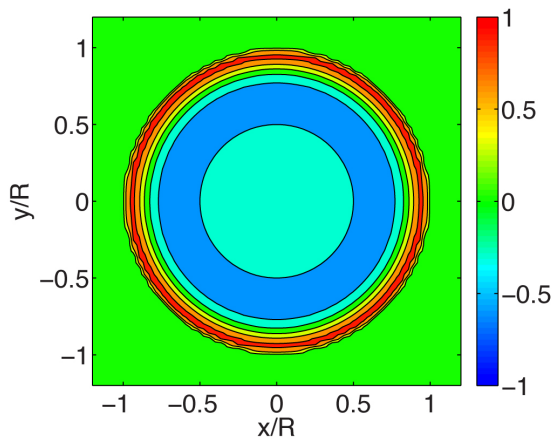
A) Out-of-plane Forcing vs  $\alpha$



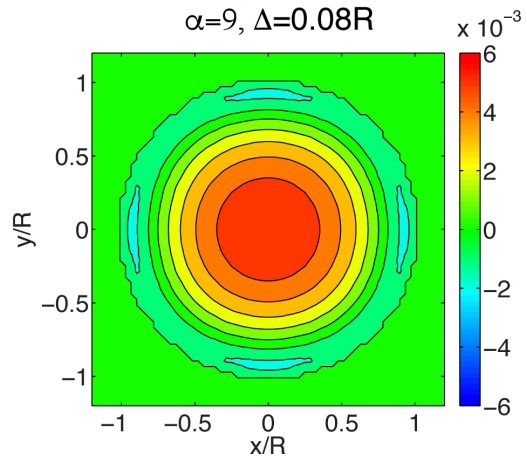
B) Bending Moment Relative Error



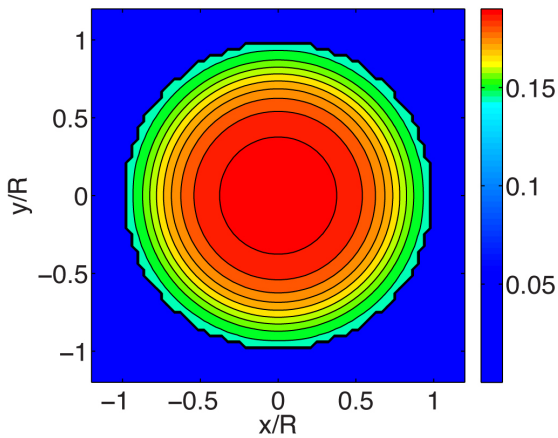
C) Out-of-plane Forcing  $\alpha=9$



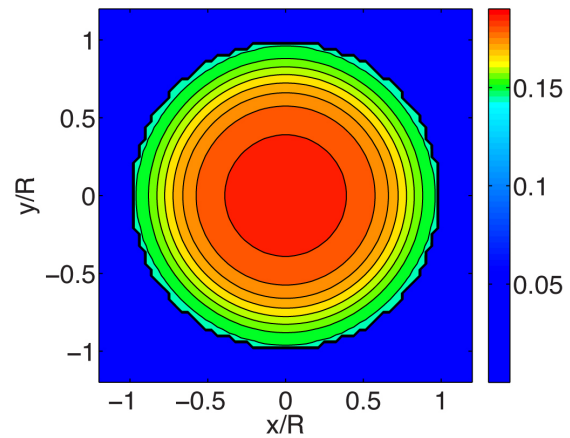
D) Bending Moment Error  $\alpha=9, \Delta=0.08R$



E) Exact Bending Moment,  $\alpha=9$



F) Recovered Bending Moment,  $\alpha=9, \Delta=0.08R$



$$M = T_0 R^2 [A(\alpha)x^{\alpha+4} + B(\alpha)x^{2\alpha+4} + C(\alpha)x^4], \quad (2.36)$$

where the coefficients  $A(\alpha)$ ,  $B(\alpha)$ , and  $C(\alpha)$  are given in the Supporting Material, together with the derivation of the solution.

The relative error of the recovered bending moment is defined as

$$Err_M = \frac{\int \int |M_{\text{recovered}} - M_{\text{exact}}| dx dy}{|M_{\text{exact}}|} dx dy, \quad (2.37)$$

and is plotted in Figure 2.5 B together with the lateral error obtained for the optimal value of the filter width,  $Err_S(\alpha, \Delta = 0.18\lambda_\alpha)$ . Overall,  $Err_M$  is approximately independent of the shape of the forcing ( $\alpha$ ) and the width of the filter ( $\Delta$ ) used to smooth out the level set function  $\Gamma$ . Furthermore,  $Err_M$  is lower than  $Err_S$ .

Similar to the lateral case, Figure 2.5 includes detailed results from a particular case corresponding to  $\alpha = 9$ . Inspection of these data indicates that the magnitudes of both the bending moment and its absolute error are highest near the center of the island. As a result, the recovered bending moment (Figure 2.5 F) underestimates the exact one near the center of the island, although this difference is small (relative error  $\approx 2\%$ ).

## Measurements of Lateral and Bending Monolayer Tension in Micropatterned Cell Islands

We used the methods described above to measure three-dimensional distributions of traction stress and intracellular stress in micropatterned islands of different shapes and sizes. Figure 2.6 shows a typical example of the measurements obtained for a circular island. The cells in the island collectively contract towards the island center by applying strong traction stresses in the x-y plane along the edge of the island (Figure 2.6 A). In the normal direction (z), the cells pull upwards along the island edge, and the resulting force is balanced out by a weaker distribution of compressive stresses that is spread more uniformly over the whole extent of the island (Figure 2.6 B). In cell islands with corners (e.g. triangular islands, see Figure 2.7 A-B), both the contractile tangential traction stresses and the pulling z stresses are

more concentrated near the high-curvature island corners, whereas the compressive stresses are still spread more uniformly over the whole extent of the island. These results are in general agreement with previously reported measurements of traction stresses in single-cell and collective-cell cultures [11, 40, 53].

The traction stresses were used as inputs to calculate the internal monolayer stresses caused by lateral deformation and the bending of the cell islands. The monolayer tension caused by each of these two contributions is also plotted in Figure 2.6 for an example circular island. It is important to note that the tensions induced by lateral deformation (Figure 2.6 C, E) and bending (Figure 2.6 D,F) have comparable magnitudes, especially in the region near the edge of the island. The tension coming from lateral deformation starts at low values at the free edge of the island and continuously increases towards the island center. This increase is sharpest near the edge of the island where the tangential traction stresses are maximum. The bending tension also rises sharply from its value at the island edge but, in contrast to the lateral tension, it plateaus in the interior region of the island. This behavior can be understood by considering that monolayer bending was highest near the island edge due to the concentration of positive and negative normal traction stresses in that region (Figure 2.6 F).

The distribution of lateral tension was similar in cell islands with corners (Figure 2.7 C,E), although the more uneven distribution traction stresses along the island edge led to a less homogeneous tension distribution. This effect was more accentuated in the bending tension (Figure 2.7 D,F). A similar behavior was observed when varying the size of the micropatterned islands (Figure 2.8 and 2.9). We observed that larger islands with more cells experienced larger spatial fluctuations in both their traction stresses and monolayer stresses.

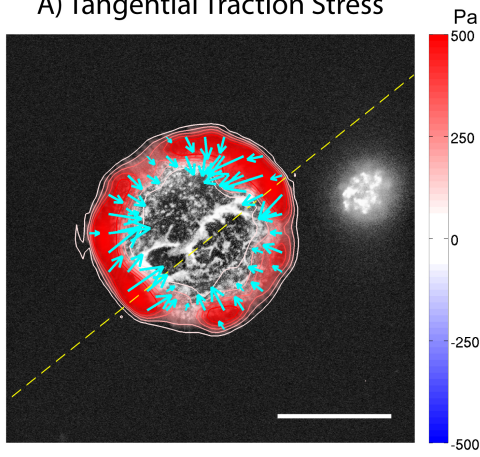
### **The effect of monolayer island size on the lateral and bending monolayer tensions**

To study how cell island size affects the lateral and the bending monolayer stresses, we performed experiments on circular micropatterned islands of different radii ( $R_{\text{island}} = 25, 45, \text{ and } 65 \mu\text{m}$ ). The choice of circular islands facilitates compiling statistics to quantify in detail the

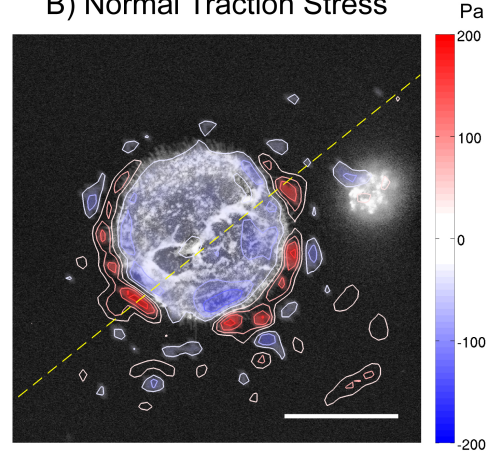


Figure 2.6: (A) Tangential traction stress ( $\tau_{xz}, \tau_{yz}$ ) field on a 45-micron radius cell island. Colormap represents magnitude  $\sqrt{\tau_{xz}^2 + \tau_{yz}^2}$ . (B) Normal traction stress field, positive values (red) pointing upwards from the substrate plane. (C) Intracellular tension due to lateral stress (color) tangential traction stress (arrows) are superimposed for reference. (D) Intracellular tension due to bending stress. (E) Side view representation of the intracellular and substrate tension due to lateral stresses along a representative line (yellow-dashed lines in A, B, C, and D). The black solid line represents the surface of the deformed substrate. Red-blue colormap represents the magnitude of the tangential  $\sqrt{\tau_{xz}^2 + \tau_{yz}^2}$  traction stress as they propagate inside the gel Orange-cyan colormap represents the intracellular tension due to lateral stress. (F) Side view representing the intracellular tension due to bending stresses. Red-blue colormap represents the magnitude of the normal traction stress  $\tau_{zz}$  as they propagate inside the gel. Orange-cyan colormap represents the intracellular tension due to bending stress. Scalebar = 50  $\mu\text{m}$ .

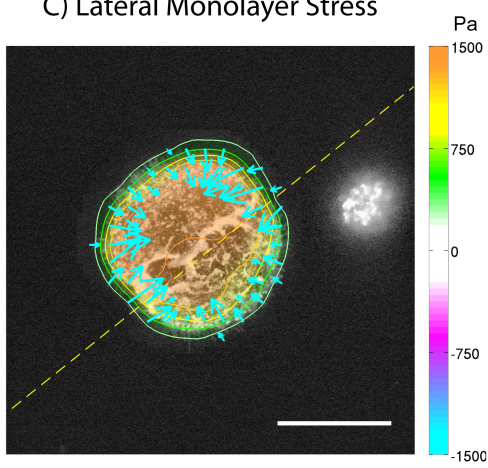
A) Tangential Traction Stress



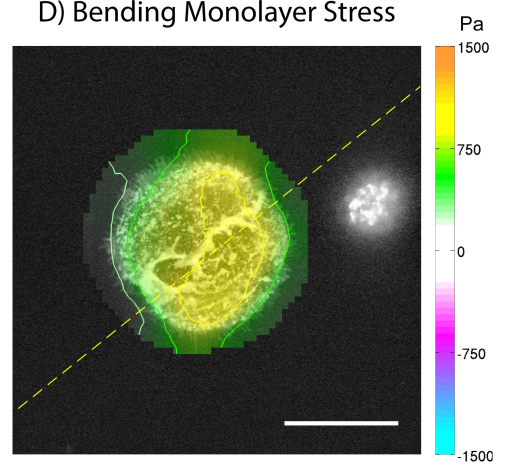
B) Normal Traction Stress



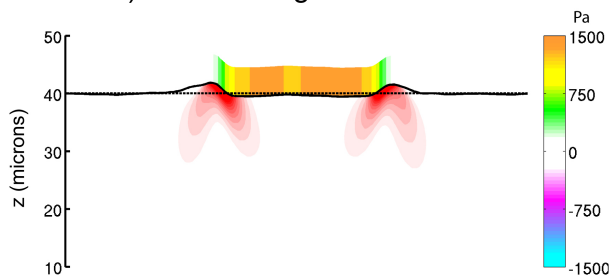
C) Lateral Monolayer Stress



D) Bending Monolayer Stress



E) Lateral/Tangential Sideview



F) Bending/Normal Sideview

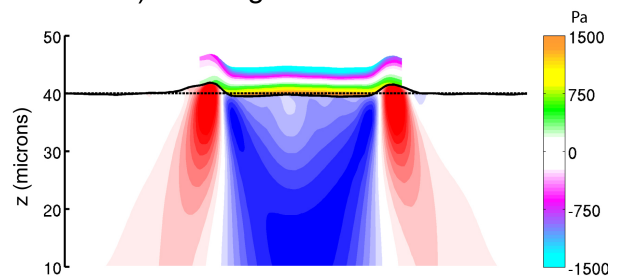
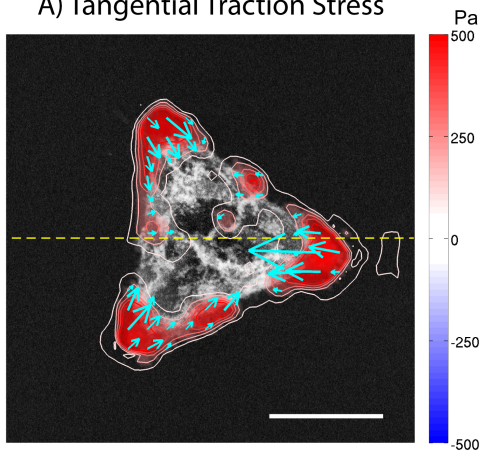
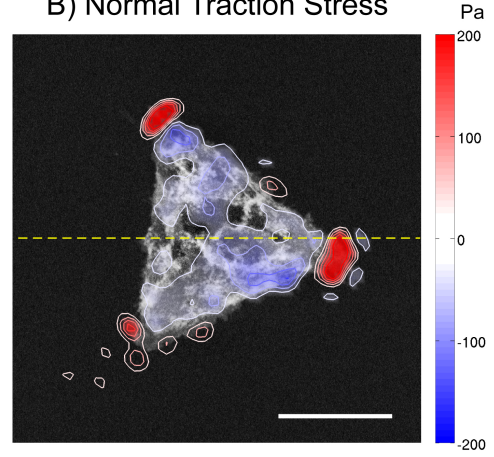


Figure 2.7: (A) Tangential traction stress  $(\tau_{xz}, \tau_{yz})$  field on a triangular cell island of side 120 microns. Colormap represents magnitude  $\sqrt{\tau_{xz}^2 + \tau_{yz}^2}$ . (B) Normal traction stress field, positive values (red) pointing upwards from the substrate plane. (C) Intracellular tension due to lateral stress (color) tangential traction stress (arrows) are superimposed for reference. Yellow dashed line represents the line along the side views are represented in E and F. (D) Intracellular tension due to bending stress. (E) Side view representation of the intracellular and substrate tension due to lateral stresses along a representative line (yellow-dashed lines in A, B, C, and D). The black solid line represents the surface of the deformed substrate. Red-blue colormap represents the magnitude of the tangential  $\sqrt{\tau_{xz}^2 + \tau_{yz}^2}$  traction stress as they propagate inside the gel Orange-cyan colormap represents the intracellular tension due to lateral stress. (F) Side view representing the intracellular tension due to bending stresses. Red-blue colormap represents the magnitude of the normal traction stress  $\tau_{zz}$  as they propagate inside the gel. Orange-cyan colormap represents the intracellular tension due to bending stress. Scalebar = 50  $\mu\text{m}$ .

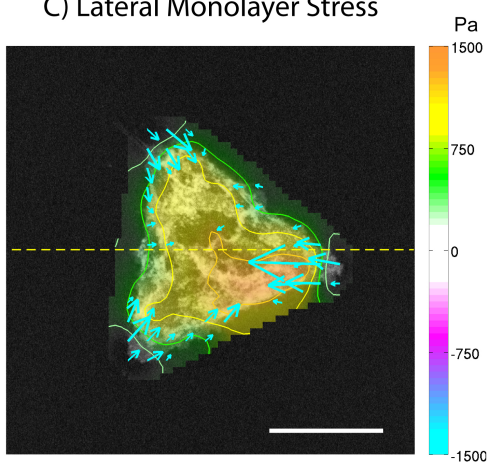
A) Tangential Traction Stress



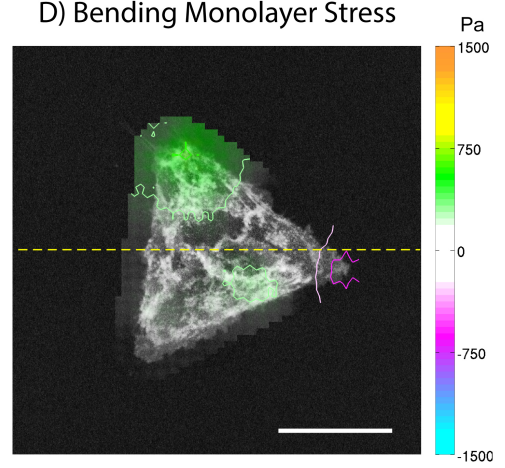
B) Normal Traction Stress



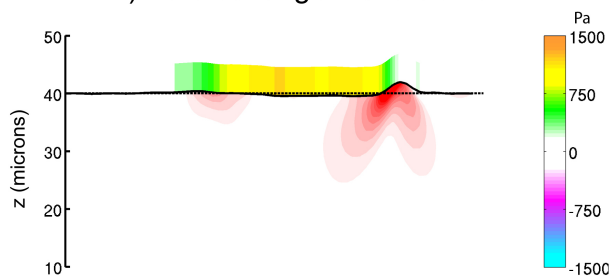
C) Lateral Monolayer Stress



D) Bending Monolayer Stress



E) Lateral/Tangential Sideview



F) Bending/Normal Sideview

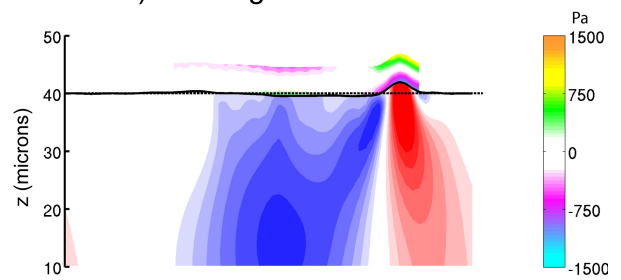
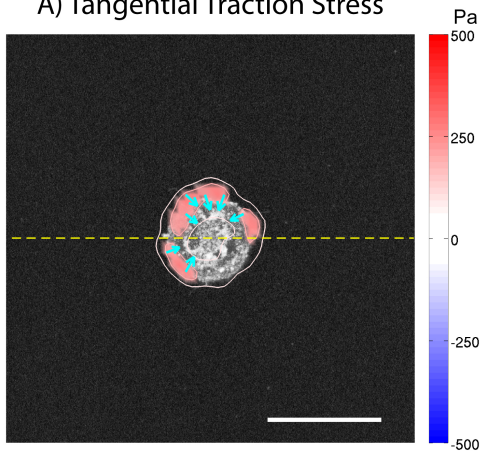
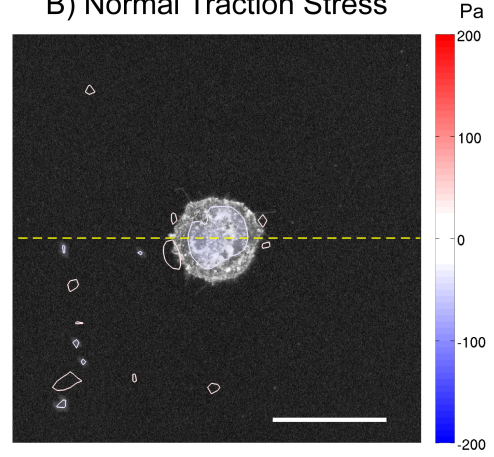


Figure 2.8: (A) Tangential traction stress ( $\tau_{xz}, \tau_{yz}$ ) field on a 25-micron radius cell island. Colormap represents magnitude  $\sqrt{\tau_{xz}^2 + \tau_{yz}^2}$ . (B) Normal traction stress field, positive values (red) pointing upwards from the substrate plane. (C) Intracellular tension due to lateral stress (color) tangential traction stress (arrows) are superimposed for reference. Yellow dashed line represents the line along the side views are represented in E and F. (D) Intracellular tension due to bending stress. (E) Side view representation of the intracellular and substrate tension due to lateral stresses along a representative line (yellow-dashed lines in A, B, C, and D). The black solid line represents the surface of the deformed substrate. Red-blue colormap represents the magnitude of the tangential  $\sqrt{\tau_{xz}^2 + \tau_{yz}^2}$  traction stress as they propagate inside the gel Orange-cyan colormap represents the intracellular tension due to lateral stress. (F) Side view representing the intracellular tension due to bending stresses. Red-blue colormap represents the magnitude of the normal traction stress  $\tau_{zz}$  as they propagate inside the gel. Orange-cyan colormap represents the intracellular tension due to bending stress. Scalebar = 50  $\mu\text{m}$ .

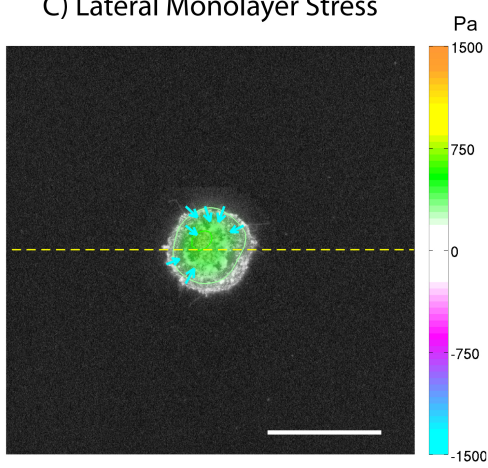
A) Tangential Traction Stress



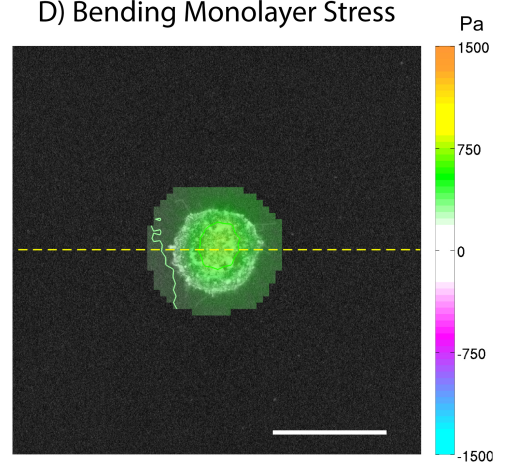
B) Normal Traction Stress



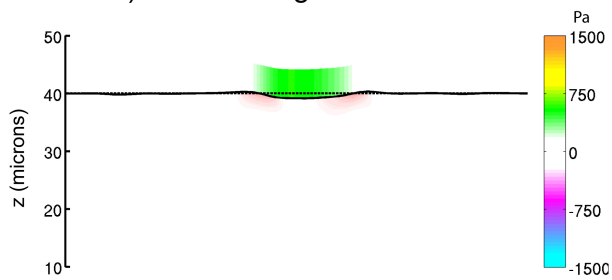
C) Lateral Monolayer Stress



D) Bending Monolayer Stress



E) Lateral/Tangential Sideview



F) Bending/Normal Sideview

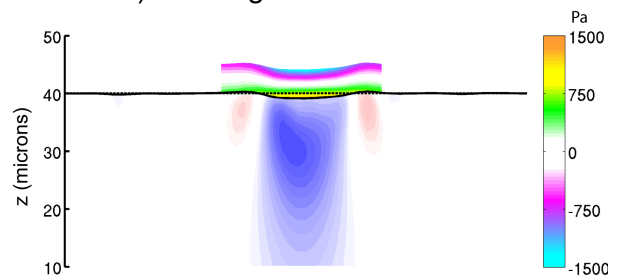
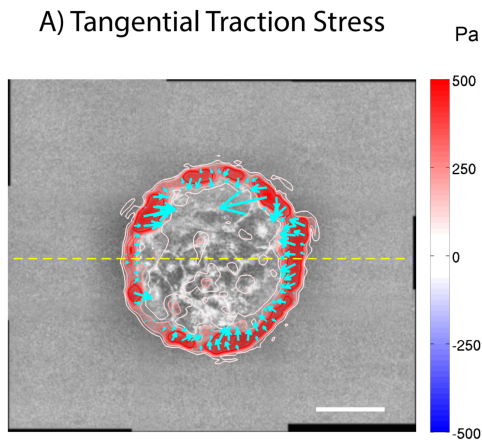
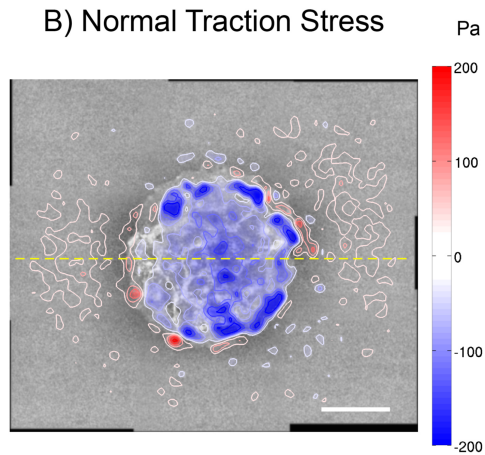


Figure 2.9: (A) Tangential traction stress ( $\tau_{xz}, \tau_{yz}$ ) field on a 65-micron radius cell island. Colormap represents magnitude  $\sqrt{\tau_{xz}^2 + \tau_{yz}^2}$ . (B) Normal traction stress field, positive values (red) pointing upwards from the substrate plane. (C) Intracellular tension due to lateral stress (color) tangential traction stress (arrows) are superimposed for reference. Yellow dashed line represents the line along the side views are represented in E and F. (D) Intracellular tension due to bending stress. (E) Side view representation of the intracellular and substrate tension due to lateral stresses along a representative line (yellow-dashed lines in A, B, C, and D). The black solid line represents the surface of the deformed substrate. Red-blue colormap represents the magnitude of the tangential  $\sqrt{\tau_{xz}^2 + \tau_{yz}^2}$  traction stress as they propagate inside the gel Orange-cyan colormap represents the intracellular tension due to lateral stress. (F) Side view representing the intracellular tension due to bending stresses. Red-blue colormap represents the magnitude of the normal traction stress  $\tau_{zz}$  as they propagate inside the gel. Orange-cyan colormap represents the intracellular tension due to bending stress. Scalebar = 50  $\mu\text{m}$ .

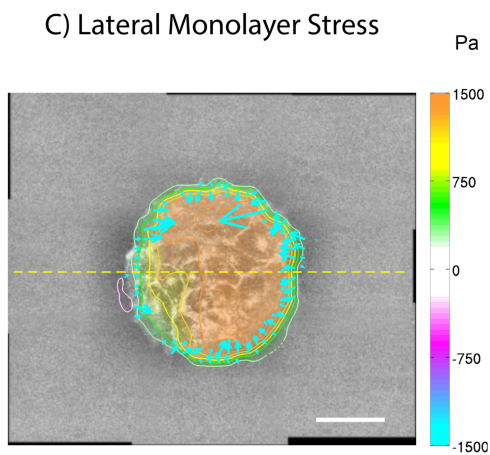
A) Tangential Traction Stress



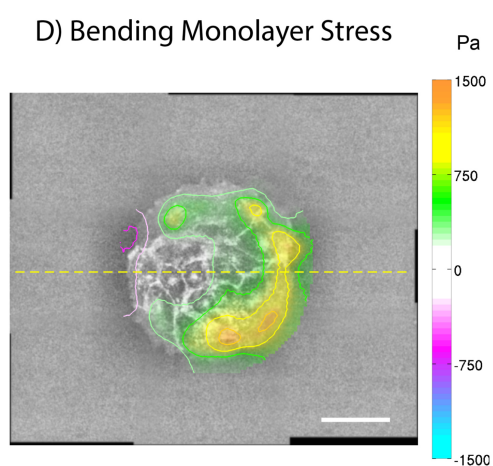
B) Normal Traction Stress



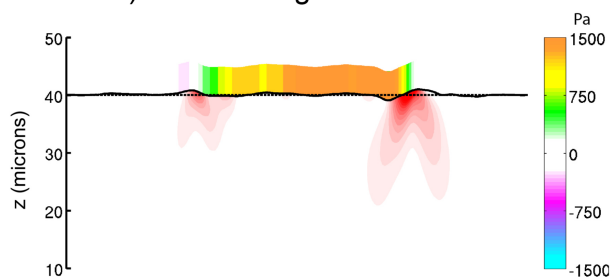
C) Lateral Monolayer Stress



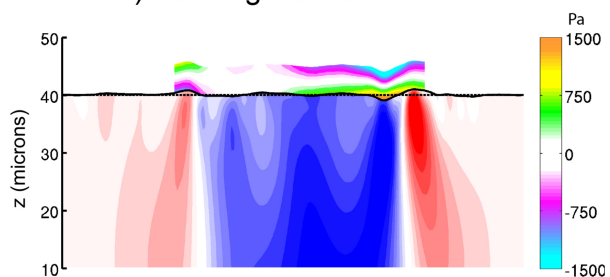
D) Bending Monolayer Stress



E) Lateral/Tangential Sideview



F) Bending/Normal Sideview





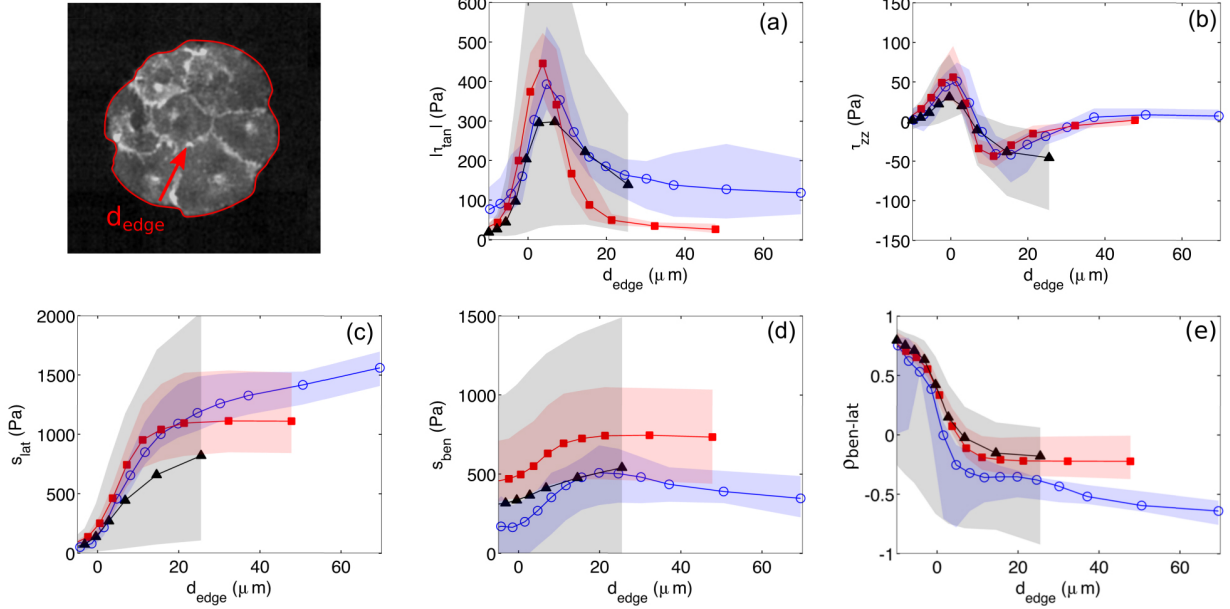


Figure 2.10: Profiles representing the average value of: magnitude of tangential (A), normal (B) traction stress, and intracellular tension due to lateral (C) and bending (D); with respect to the distance to the edge in circular islands of 25(μm), 45(μm), and 65(μm) radius. Solid lines, average value, shaded regions, 25% and 75% quartiles.

spatial distribution of the monolayer stresses. For each island, we expressed traction and monolayer stresses in a polar coordinate system with origin at the center of the island (e.g. the tension was denoted as  $s_i(r, \theta)$  where the index  $i$  identifies islands within each diameter group, and  $0 < r < R_{\text{island}}$  and  $0 < \theta < 2\pi$  are the radial and azimuthal coordinates), and calculated their mean and standard deviation along the angular direction,

$$S_i(r) = \frac{1}{2\pi} \int_0^{2\pi} s_i(r, \theta) d\theta, \quad (2.38)$$

$$S'_i(r) = \left\{ \frac{1}{2\pi} \int_0^{2\pi} [s_i(r, \theta) - S_i(r)]^2 d\theta \right\}^{\frac{1}{2}}. \quad (2.39)$$

These variables were averaged for the total number of islands ( $N$ ) within each island radius group to obtain the mean stress profiles  $\bar{S}(r) = \frac{1}{N} \sum_{i=1}^N S_i(r)$ , and the standard deviation profiles  $\bar{S}'(r) = \frac{1}{N} \sum_{i=1}^N S'_i(r)$ . They are plotted in Figures 2.10 and 2.11 as a function of the distance to the edge,  $d_{\text{edge}} = R_{\text{island}} - r$ .

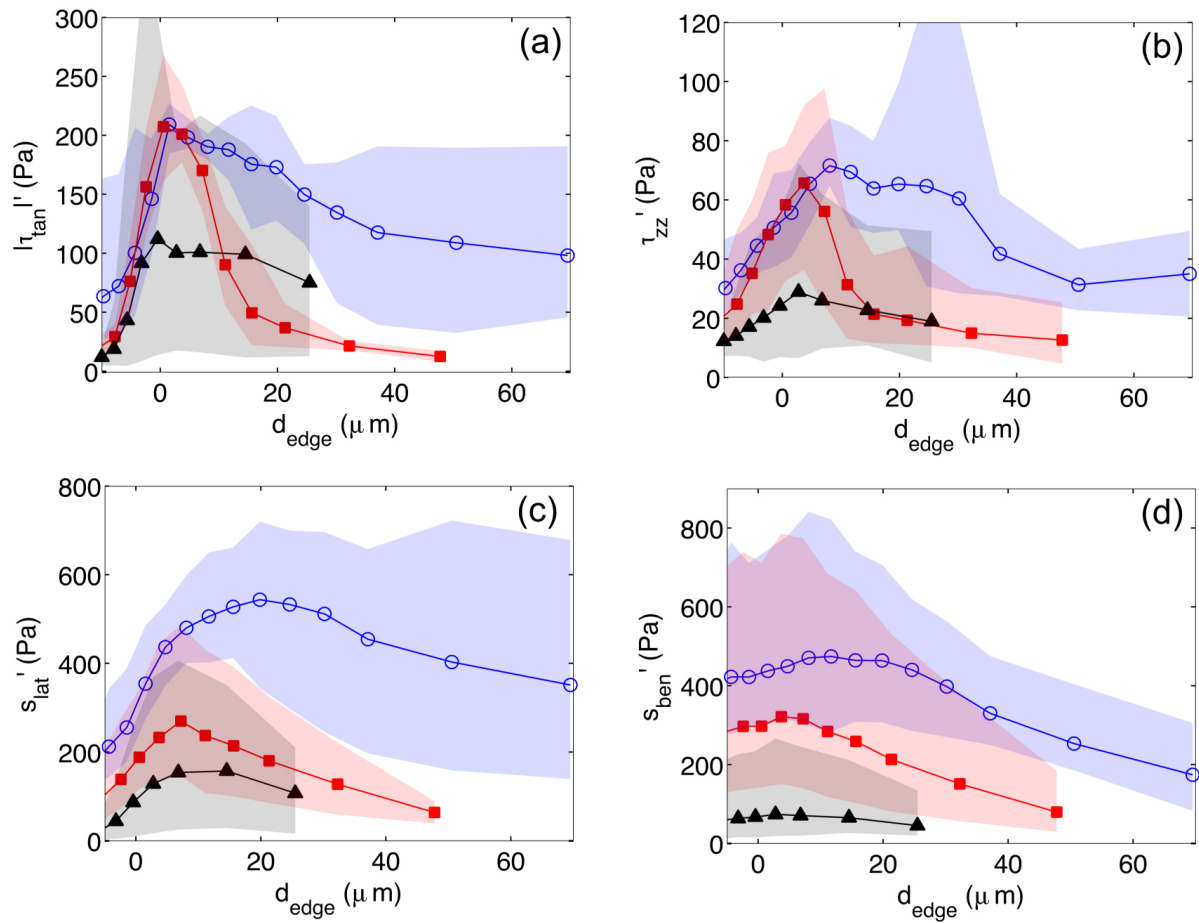


Figure 2.11: Profiles representing the standard deviation of: magnitude of tangential (A), normal (B) traction stress, and intracellular tension due to lateral (C) and bending (D); with respect to the distance to the edge in circular islands of 25(black), 45 (red), and 65(blue)  $\mu\text{m}$  radius. Solid lines, average value, shaded regions, 25% and 75% quartiles.

The mean profiles of the tangential traction stresses ( $|\tau_{\text{tan}}|(d_{\text{edge}})$ ) peak around  $\approx 5 \mu\text{m}$  away from the island edge (Figure 2.10 A). This behavior is independent of island size suggesting that these traction stress patterns are mainly generated by the outermost single row of cells of the island. Consistent with previous observations on single cells [11], the normal stresses ( $\tau_{zz}(d_{\text{edge}})$ ) have a maximum (i.e. pulling) that precedes the peak of the tangential stresses by  $\approx 5 \mu\text{m}$ , and a minimum (i.e. pushing) that follows it by  $10 \mu\text{m}$ . The value of this maximum,  $\tau_{zz,\text{max}} \approx 60\text{Pa}$ , is lower than the maximum value of tangential stresses  $|\tau_{\text{tan}}|_{\text{max}} \approx 400 \text{Pa}$  for all island sizes, and this difference is statistically significant for the two largest island sizes. These peak values of both the tangential and normal traction stresses do not vary significantly with island size. Away from the edge, the mean profiles of the traction stresses decay towards the center of the island, and this behavior is more evident for the larger islands. Of note, the  $\tau_{zz}$  profile remains negative-valued beyond its minimum, suggesting that in average the cells away from the edge exert a gentle pressure on their substrate (consistent with the data shown in Figures 2.6 B, 2.7 B and 2.9 B). Besides, the fluctuations of the traction stresses,  $|\tau_{\text{tan}}|'(d_{\text{edge}})$  and  $\tau'_{zz}(d_{\text{edge}})$ , seem to increase with island size, especially in the interior of the island (Figure 2.11 A,B).

The mean profiles of lateral and bending tension,  $s_{\text{lat}}(d_{\text{edge}})$  and  $s_{\text{ben}}(d_{\text{edge}})$ , follow similar trends with  $d_{\text{edge}}$  regardless of island size (Figure 2.10 C,D). They raise sharply near the edge of the island where the traction stresses are strongest, and reach a plateau in the interior of the island. This behavior, which is more apparent for the larger islands, suggests that a monolayer reaches homeostasis a few cell rows far away from its free edge, not only for its lateral tension as previously reported [61], but also for its bending tension. Remarkably, the lateral tension is zero at the edge of the islands whereas the bending tension is not, which implies that there is a region near the island edge where bending is the dominant source of mechanical tension inside the monolayer. To quantify the relative contributions of lateral deformation versus bending to monolayer tension, we computed the quantity

$$\rho_{\text{ben-lat}} = \frac{|s_{\text{ben}}| - |s_{\text{lat}}|}{|s_{\text{ben}}| + |s_{\text{lat}}|}, \quad (2.40)$$

which varies between  $-1$  (pure lateral distortion) and  $1$  (pure bending). The profile of  $R_{\text{ben-lat}}$  (Figure 2.10 E) shows that bending is the dominant source of intracellular tension near the island edge. As we move towards the interior of the island lateral deformation becomes increasingly more important, but bending is still an appreciable source of intracellular stress at the center of the island ( $\rho_{\text{ben-lat}} \approx -0.5$ ). This behavior seems to depend little on cell island size, although we observe a trend for bending to become less important far from the edge of the island as we increase  $R_{\text{island}}$ .

## 2.4 Discussion

Monolayer Stress Microscopy (MSM) is becoming an increasingly widespread method to quantify the collective generation and transmission of intracellular stress. There are several different approaches to calculate intracellular stresses from measurements of substrate deformation, including the discrete application of Newton’s third law at cell-cell boundaries [62], continuum mechanics models based on the analogy between the monolayer and a thin-plate [15, 21], dissipative particle dynamics simulations [16] and Bayesian inference [18]. However, none of these approaches considers that a cell monolayer can undergo bending due to mechanical stresses pointing in the direction perpendicular its surface, even when cultured on a flat substrate. These bending stresses can be generated by the cells that form the monolayer [14, 35] but also by cells outside of the monolayer. For example, leukocytes undergoing endothelial transmigration generate mechanical forces that bend the endothelium at the transmigration site [20]. Furthermore, epithelial bending and invagination driven by mechanical forces play a key role in the development of most tissues and organs [63]. Currently, there is a lack of experimental data about the contribution of bending to intracellular tension, and also about the propagation of this mechanical signal throughout monolayers.

The intracellular tension caused by small bending in a cell monolayer can be inferred by extending Trepat et al’s [15, 21] thin-plate analogy to consider not only equilibrium of forces, but also equilibrium of bending moments. The inputs to the extended 3-D MSM method are the 3-D traction stresses at the interface between the cell monolayer and its sub-

stratum, i.e.  $[\tau_{xz}(x, y), \tau_{xz}(x, y), \tau_{zz}(x, y)]$ , which requires interrogating the 3-D deformation of the substrate in a thin volumetric slice near the surface of the substrate [38]. Similar to traction force microscopy, where global force balance yields an integral constraint for the measured deformations (i.e. zero average displacement) [51], global balance of bending moments leads to an additional constraint (i.e. zero average tilt). Given that the image processing algorithm for measuring substrate deformation involves the optimization of image cross-correlation, the constraints can be incorporated during image processing instead of during stress recovery. This approach is advantageous since it adapts the weight of the constraints in each region of the image according to its local signal to noise ratio, and it generally yields more realistic displacement measurements.

The MSM equations were discretized numerically on a Cartesian grid using Fourier series. The boundary conditions at the edges of the monolayer were imposed via a level-set immersed interface method [39]. In this formulation, the problem is solved in a rectangular domain that encompasses the edges of the monolayer, i.e. the immersed interface, and virtual body forces are imposed to enforce boundary conditions. This procedure leads to a relaxation problem that can be marched in time until it converges to a steady state solution that simultaneously satisfies equilibrium of moments and forces, as well as the boundary conditions at the edges of the monolayer. Compared to finite element methods, the Fourier immersed interface method does not require solving large linear systems of equations. Additionally, it interfaces exactly with the Fourier method used to determine the traction stress inputs to the MSM equations [5, 37, 38, 48, 55, 56]. The numerical solver was validated by prescribing a family of synthetic traction stress distributions for which the lateral and bending monolayer stresses can be calculated analytically, and which mimic our 3D experimental data on endothelial monolayer islands. This validation study suggested that the main source of numerical error is the level-set function used to impose the immersed interface boundary condition. When the level-set function varies too sharply, we observe spurious oscillations near the monolayer edge due to Gibbs error. On the other hand, if the level-set function is too smooth, the virtual body forces propagate inside the monolayer and the boundary conditions are smeared out. These two effects can be balanced out when the steepness of the

level-set function is adjusted to be proportional to the steepness of the tangential traction stresses near the island edge, in which case the error decreases to  $\approx 5\%$ .

Within the framework of the thin plate model, the intracellular tension induced by convex bending ( $M > 0$ ) varies across the thickness of the monolayer, reaching its maximum (tension) and minimum (compression) values at the top (i.e. apical) and bottom (i.e. basal) surfaces. This variation is given by

$$IT(x, y, z) = \frac{zE(z)}{(1 - \nu(z)^2)\bar{D}}M(x, y), \quad (2.41)$$

where  $\bar{D} = \int_{-h/2}^{h/2} z^2 E(z) / [1 - \nu(z)^2] dz$  is the flexural rigidity of the monolayer averaged across its thickness. The opposite distribution of bending stresses (i.e. apical compression and basal tension) is obtained for concave bending ( $M < 0$ ). The z-dependence of the bending-induced intracellular stresses makes it difficult to quantify their average magnitude across monolayer width. For lack of detailed data about the variation of intracellular Young's modulus and Poisson's ratio across the z direction, our MSM model assumes uniform mechanical properties. In this idealized case, the value of the bending stresses averaged across monolayer width is zero, so we chose the mean of their absolute value to quantify their magnitude. We note, however, that the mean bending stresses across the thickness of the monolayer need not be zero in the more realistic scenario where the mechanical properties of cells vary in the z direction. Mechanistically, this result reflects the fact that intracellular stresses concentrate in stiffer subcellular compartments. Recent data indicate that the main tension bearing elements of adherent cells, i.e. the stress fibers, have different orientations in the basal and apical regions of cells adhering to convex surfaces [64]. The reported orientation patterns are consistent with the apical stress fibers but not the basal ones bearing tension, in agreement with bending creating mechanical tension in the apical surface and compression in the basal surface. How cells are able to withstand compressive stresses is less clear, although the nucleus and cytoplasmic pressure mediated by membrane curvature have been postulated as candidates [64, 65]. The fact that bending may result in compressive or tensile stress and deformation in different compartments of the cell based on their

apical/basal localization could have implications for mechanotransduction.

In epithelial cell sheets, the intracellular stresses caused by lateral cell contractility have been shown to propagate over distances much longer than the size of a single cell, and to contribute to collective mechanosensing [66]. However, the propagation of intracellular stresses caused by normal contractility has not been explored systematically so far. To address this question, we applied 3D MSM to confluent micropatterned cell islands of different shapes and sizes, and obtained the first measurements of intracellular tension caused by out-of-pane traction stresses. These measurements revealed that the magnitude of bending intracellular tension can exceed that of the tension caused by lateral contractility near the edges of a cell monolayer, particularly in regions of high edge curvature like corners. We also found that the internal stresses caused by bending do not propagate as far as the internal stresses caused by lateral contractility, and tend to balance out within a few ( $\sim 1$ ) cell lengths into the monolayer. This concentrated effect may be relevant for phenomena like cellular extravasation, which are accompanied by significant normal deflections of the endothelial monolayer, and which require spatially regulated changes in endothelial permeability [20, 67].

## 2.5 Appendix

### 2.5.1 Implementation of Gradient Descent Method for Constrained PIV

Consider the optimization problem with the following cost function:

$$\begin{aligned}
J_{i,j} = & C_{i,j}(u_x, u_y, u_z) + \frac{\lambda_x}{N_x N_y} \sum_{i=1}^{N_x} \sum_{j=1}^{N_y} u_{x_{i,j}} + \frac{\lambda_y}{N_x N_y} \sum_{i=1}^{N_x} \sum_{j=1}^{N_y} u_{y_{i,j}} \\
& + \frac{\lambda_z}{N_x N_y} \sum_{i=1}^{N_x} \sum_{j=1}^{N_y} u_{z_{i,j}} + \frac{\mu_{xy}}{N_x N_y} \sum_{i=1}^{N_x} \sum_{j=1}^{N_y} y_{i,j} u_{x_{i,j}} + \frac{\mu_{yx}}{N_x N_y} \sum_{i=1}^{N_x} \sum_{j=1}^{N_y} x_{i,j} u_{y_{i,j}} \\
& + \frac{\mu_{zx}}{N_x N_y} \sum_{i=1}^{N_x} \sum_{j=1}^{N_y} x_{i,j} u_{z_{i,j}} + \frac{\mu_{zy}}{N_x N_y} \sum_{i=1}^{N_x} \sum_{j=1}^{N_y} y_{i,j} u_{z_{i,j}}, \tag{2.42}
\end{aligned}$$

where the cross-correlation of the two interrogation windows  $C_{i,j}$  can be fitted to a paraboloid,

$$C_{i,j}(u_x, u_y, u_z) = A_1 + A_2u_x + A_3u_y + A_4u_z + A_5u_x^2 + A_6u_y^2 + A_7u_z^2 + A_8u_xu_y + A_9u_xu_z + A_{10}u_yu_z. \quad (2.43)$$

We want to maximize the cost function (2.42) for each window  $i, j$ . Since the constraints involve the displacements of every window, the problem becomes  $3N \times 3N$  where  $N$  is the number of windows. The analytical solution of that optimization problem is cumbersome and direct inversion can result slow. If the Lagrange multipliers are known, the derivatives with respect to  $u_x, u_y$ , and  $u_z$  equated to zero yield,

$$\bar{u} = P^{-1} [\bar{a} + \bar{\lambda} + M\bar{x}] \quad (2.44)$$

where  $\bar{u}$  is the displacement of the window  $i, j$

$$\bar{u} = \begin{bmatrix} u_x \\ u_y \\ u_z \end{bmatrix}, \quad (2.45)$$

$$P^{-1} = \frac{1}{PD} \begin{bmatrix} P_{11} & P_{12} & P_{13} \\ P_{21} & P_{22} & P_{23} \\ P_{31} & P_{32} & P_{33} \end{bmatrix}, \quad (2.46)$$

$$PD = 2 (A_7A_8^2 - A_8A_9A_{10} + A_6A_9^2 + A_5A_{10}^2 - 4A_5A_6A_7) \quad (2.47)$$



$$P_{11} = A_{10}^2 - 4A_6A_7 \quad (2.48)$$

$$P_{12} = 2A_7A_8 - A_9A_{10} \quad (2.49)$$

$$P_{13} = 2A_6A_9 - A_8A_{10} \quad (2.50)$$

$$P_{21} = P_v1 \quad (2.51)$$

$$P_{22} = A_9^2 - 4A_5A_7 \quad (2.52)$$

$$P_{23} = 2A_5A_{10} - A_8A_9 \quad (2.53)$$

$$P_{31} = P_{13} \quad (2.54)$$

$$P_{32} = P_{23} \quad (2.55)$$

$$P_{33} = A_8^2 - 4A_5A_6 \quad (2.56)$$

$$\bar{a} = \begin{bmatrix} A_2 \\ A_3 \\ A_4 \end{bmatrix}, \quad (2.57)$$

$$\bar{\lambda} = \begin{bmatrix} \lambda_x \\ \lambda_y \\ \lambda_z \end{bmatrix}, \quad (2.58)$$

$$M = \begin{bmatrix} 0 & \mu_{xy} \\ \mu_{yx} & 0 \\ \mu_{zx} & \mu_{zy} & 0 \end{bmatrix}, \quad (2.59)$$

$$\bar{x} = \begin{bmatrix} x \\ y \end{bmatrix}. \quad (2.60)$$

In this case, finding the displacements has the cost of solving  $N$  3x3 problems. The

Lagrange multipliers can be found with a gradient descent approach. The derivatives of the cost function (2.42) with respect to  $\lambda$  and  $M$  simply return the equilibrium conditions,

$$\frac{\partial J}{\partial \lambda_x} = \sum_{i=1}^{N_x} \sum_{j=1}^{N_y} u_{x_{i,j}} \quad (2.61)$$

$$\frac{\partial J}{\partial \lambda_y} = \sum_{i=1}^{N_x} \sum_{j=1}^{N_y} u_{y_{i,j}} \quad (2.62)$$

$$\frac{\partial J}{\partial \lambda_z} = \sum_{i=1}^{N_x} \sum_{j=1}^{N_y} u_{z_{i,j}} \quad (2.63)$$

$$\frac{\partial J}{\partial \mu_{xy}} = \sum_{i=1}^{N_x} \sum_{j=1}^{N_y} y_{i,j} u_{x_{i,j}} \quad (2.64)$$

$$\frac{\partial J}{\partial \mu_{yx}} = \sum_{i=1}^{N_x} \sum_{j=1}^{N_y} x_{i,j} u_{y_{i,j}} \quad (2.65)$$

$$\frac{\partial J}{\partial \mu_{xz}} = \sum_{i=1}^{N_x} \sum_{j=1}^{N_y} x_{i,j} u_{z_{i,j}} \quad (2.66)$$

$$\frac{\partial J}{\partial \mu_{zy}} = \sum_{i=1}^{N_x} \sum_{j=1}^{N_y} y_{i,j} u_{z_{i,j}} \quad (2.67)$$

The algorithm for PIV with force and moment equilibrium constraints is implemented as follows,

1. Take an initial guess for  $\bar{\lambda}$  and  $M$ .
2. Evaluate  $\bar{u}$  using (2.44).
3. Evaluate the gradient (2.61 - 2.67).
4. Update  $\lambda$  and  $M$  with gradient descent

$$\bar{\lambda}^{n+1} = \bar{\lambda}^n + \gamma \frac{\partial J}{\partial \bar{\lambda}}$$

$$M^{n+1} = M^n + \gamma \frac{\partial J}{\partial M}$$

5. Repeat steps 2-4 until desired convergence.

## 2.5.2 Derivation of analytical solutions for validation of the Lateral Problem

We validated our procedure to recover monolayer tension from tangential traction stresses for a cell monolayer island under the radially symmetric traction stress:

$$T_r = T_0 x^2 (1 - x^\alpha) \quad (2.68)$$

where  $r$  is the distance to the center of the island,  $R$  is the island radius and  $x = r/R$ . The parameter  $\alpha \geq 1$  defines how concentrated the traction stresses are near the edge of the island, and  $T_0$  is a characteristic stress. This synthetic traction stress distribution is in equilibrium of forces and moments. The governing equations for this problem are the lateral elastic equilibrium and compatibility equations, i.e.

$$\partial_r \sigma_{rr} + \frac{1}{r} (\sigma_{rr} - \sigma_{\theta\theta}) = T_r, \quad (2.69)$$

$$\partial_r [r \partial_r (\sigma_{rr} + \sigma_{\theta\theta})] = (1 + \nu) \partial_r (r T_r), \quad (2.70)$$

where  $\sigma_{rr}$  and  $\sigma_{\theta\theta}$  are the diagonal elements of the lateral stress tensor expressed in polar coordinates. The boundary condition for this problem is zero radial intracellular stress at the island edge  $\sigma_{rr}(x = 1) = 0$ . Given the form of these equations and the boundary condition, we try solutions of the form

$$\sigma_{rr} = T_0 R [A(\alpha, \nu) (x^3 - 1) + B(\alpha, \nu) (x^{3+\alpha} - 1)], \quad (2.71)$$

$$\sigma_{\theta\theta} = T_0 R [C(\alpha, \nu) x^3 + D(\alpha, \nu) x^{3+\alpha} + E(\alpha, \nu)]. \quad (2.72)$$

Plugging these solutions into the governing equations, and matching terms of similar order in  $x$  for each equation, we obtain a linear system of algebraic equations for the unknown

coefficients

$$x^2 \rightarrow 4A - C = 1, \quad (2.73)$$

$$x^{2+\alpha} \rightarrow (4 + \alpha)B - D = -1, \quad (2.74)$$

$$x^{-1} \rightarrow E = -(A + B), \quad (2.75)$$

$$x^2 \rightarrow 3A + 3C = 1 + \nu, \quad (2.76)$$

$$x^{2+\alpha} \rightarrow (3 + \alpha)(B + D) = -(1 + \nu). \quad (2.77)$$

The solution of this system of equations is

$$A(\alpha, \nu) = F(0, \nu), \quad (2.78)$$

$$B(\alpha, \nu) = -F(\alpha, \nu), \quad (2.79)$$

$$C(\alpha, \nu) = G(0, \nu), \quad (2.80)$$

$$D(\alpha, \nu) = -G(\alpha, \nu), \quad (2.81)$$

$$E(\alpha, \nu) = -F(0, \nu) + F(\alpha, \nu), \quad (2.82)$$

where

$$F(\alpha, \nu) = \frac{4 + \alpha + \nu}{(3 + \alpha)(5 + \alpha)}, \quad (2.83)$$

$$G(\alpha, \nu) = (4 + \alpha)F(\alpha, \nu) - 1. \quad (2.84)$$

### 2.5.3 Derivation of analytical solutions for validation of Bending Problem

We validated our procedure to recover monolayer tension caused by bending for a cell monolayer island under the normal traction stress:

$$T_z = T_0 x^2 (1 - x^\alpha) \left( x^\alpha - \frac{2}{2 + \alpha} \right), \quad (2.85)$$

where  $r$  is the distance to the center of the island,  $R$  is the island radius and  $x = r/R$ . The parameter  $\alpha \geq 1$  defines how concentrated the traction stresses are near the edge of the island, similar to the lateral validation problem, and  $T_0$  has dimensions of stress. This synthetic traction stress distribution is in equilibrium of forces and moments, particularly bending moments. The governing equation for this axially symmetric problem is

$$\partial_{rr} M + \frac{1}{r} \partial_r M = T_z. \quad (2.86)$$

Considering the forms of this equation and the forcing term, we try a solution of the form

$$M = T_0 R^2 [A(\alpha)x^{\alpha+4} + B(\alpha)x^{2\alpha+4}C(\alpha)x^4]. \quad (2.87)$$

Note that this solution automatically satisfies the boundary condition  $\partial_r M|_{r=R} = 0$ . Plugging this solution into the governing equation and matching terms of similar order in  $x$ , we arrive at:

$$x^{2+\alpha} \rightarrow A = \frac{1}{(2 + \alpha)(4 + \alpha)}, \quad (2.88)$$

$$x^{2+2\alpha} \rightarrow B = -\frac{1}{4(2 + \alpha)^2}, \quad (2.89)$$

$$x^2 \rightarrow C = -\frac{1}{8(2 + \alpha)}. \quad (2.90)$$

## 2.6 Acknowledgements

Chapter 2, in part, has been submitted for publication of the material as it may appear in *Biophysical Journal*, 2018, Serrano, Ricardo; Aung, Aereas; Lasheras, Juan C.; Varghese, Shyni; del Álamo, Juan C.. The dissertation author was the primary author of this paper.

# Chapter 3

## High-throughput phenotypical Screening of Force and Stiffness of Cardiomyocytes

### 3.1 Introduction

Advances in induced pluripotent stem cell technology have, among other feats, open the possibility of producing cardiomyocytes in a scalable, robust way [68]. With access to large numbers of cells, scientists have devoted their efforts to recreate cardiac disease in vitro models, and assays to evaluate the efficiency and safety of new treatments [69]. Physiological assays for cardiomyocytes focus mainly to quantify one or more of the signals that determine cardiomyocyte function, namely: action potential, cytosolic calcium concentration, and mechanical force production [31, 70].

While assays that measure action potential and calcium signals are relatively well-established [71, 72], quantifying cardiac contractility both in single cells and monolayers is still elusive. High-throughput contractility assays are, in general, based on optic measurements -typically high-framerate videos obtained with a High Content Screening system [73–76]. The conditions in which the cells are imaged are also far from being standardized. Some methods require images of a fluorescent label whereas other methods work directly on transmitted light images. Remarkably, in all of the methods literature the cells seeded directly on the bottom of the multiwell plate -glass or plastic. However, the stiffness of the substrate has been proven of key relevance in iPS-CM maturity and function [77, 78].

There is also a lack of uniformity in the definition and physical meaning of the readout of these methodologies. Although the concept of contraction is intuitive, the way contractility is quantified in current method is loosely defined. Some methods report measurements on basic metrics such as the change in light intensity [73] or correlation of image blocks [75]. Other more advanced methods use optical flow to get a measurement of velocity fields during contraction [74, 76]. All of these methods rely on cell motion as surrogate of contractility.

Traction Force Microscopy is considered the golden standard to provide accurate measurement of cell force [6]. To perform TFM measurements, the cells must be seeded on a soft deformable substrate of known mechanical properties. These gels are embedded with fluorescent beads that serve as tracers for the deformation cause by the cell forces. The measured deformations, together with the information about the substrate stiffness, are used to infer the resulting force field that caused such deformations. However, TFM is seldom used in high throughput applications [79].

Aside of contractility properties, the passive elasticity of cardiomyocytes affects the ability of cardiac tissue to relax. Changes in the stiffness of cardiomyocytes have been related to cardiac disease such as heart failure with preserved ejection fraction [80]. Recent studies have uncovered proteins that contribute to the passive elasticity of cardiomyocytes as potential therapeutic targets for diastolic dysfunction [81–83]. Currently, the most common technique to measure the stiffness of tissue is Atomic Force Microscopy [84], a technique that requires highly specialized tools and is time consuming. Today, even though both contractile forces and passive mechanical properties are known to be essential for the function of cardiac tissue, there are no methods to quantify cellular forces and cellular stiffness in high throughput.

We have designed a device that consists on a 96 well plate with polyacrylamide gels at the bottom of each well. These substrates can be coated with any ECM protein of interest and can be used for TFM experiments. This device meets the standard of SBS plates and can be easily imaged in any standard High Content Screening system. In addition, we have developed fully automated software that evaluates cardiomyocyte contractility and passive



stiffness from the combination of high-speed videos of the deformation of the cells as well as deformation of the substrate under cell contraction. To validate our platform, we have cultured monolayers of spontaneously beating hIPS-CM on the 96 well plate device and run the presented analysis to obtain dose-response curves against benchmark compounds.

## 3.2 Materials and Methods

### 3.2.1 Fabrication of Polyacrylamide Gel Fabrication in 96-well format

A glass slide of size 105x140mm, No.2 thickness, (260453, TedPella Redding, CA, USA) was cut down to a size of 75x113mm with help of a diamond scribe and a straight edge. The slide was then placed on a hot plate at 90°C and 0.1M NaOH was added until the top surface was covered. The slide was left on the hot plate until total evaporation of the liquid. Next, the slide was treated with (3-Aminopropyl) triethoxysilane (APTES) (Sigma-Aldrich, St. Louis, MO) for 3min. Then it was rinsed with ultrapure water and dried. Afterwards the slide was treated with a solution of 0.5% Gluteraldehyde (Sigma-Aldrich, St. Louis, MO) in ultrapure water for 30min. Finally the slide was washed in ultrapure water and dried.

To facilitate later peeling of the top coverslips, four 26x75mm coverslips (1916-25075, Bellco, Vineland, NJ) were treated in an UV Ozone cleaner for 3min. The treated surfaces were coated with PLL-g-PEG (PLL(20)-g[3.5]-PEG(2): poly-L-lysine-g-poly(ethyleneglycol), SurfaceSolutions GmbH, Zurich) for 20min at room temperature. The PLL-g-PEG was then aspirated making the treated surface hydrophobic.

A mixture consisting of 50uL 40% acrylamide (MilliporeSigma, Burlington, MA), 60uL 2.2% bis-Acrylamide (MilliporeSigma, Burlington, MA), 3uL of 0.2um TRITC fluorescent beads (Invitrogen, Carlsbad, CA), and 2uL of Irgacure 2959 (Sigma-Aldrich, St. Louis, MO) at 30mg/mL yielded gels of 9kPa.

The mixture was pipetted on the silanized bottom coverslip and sandwiched with the PLL-g-PEG coated surface of the top coverslip. The assembly (3.1A) was placed on

top of a benchtop UV transilluminator (UVP, Cambridge UK) and photomask (Advance Reproductions, North Andover, MA, see 3.1 C for photomask design). The mix was cured under UV light (UV Benchtop Transilluminator, UVP, Upland, California, 302nm, 8W) for 10min -this time may vary depending on the light source intensity and wavelength. After curation, the top coverslips are peeled and the gels remain in the areas where the photomask is transparent (3.1 B). Unpolymerized liquid was aspirated. This step must be done quickly to prevent desiccation of the gels. Lastly, plastic walls with a bottom adhesive (204969, Grace Bio-Labs, Bend, OR, USA) were placed, sealing each well individually (3.1 D). Finally PBS 1X was added to each well to guarantee hydration of the gels and check for possible leaks due to manufacturing faults.

### **3.2.2 Differentiation of hiPSCs to Cardiomyocytes**

hiPSCs (hiPSC line SCVI15 and SCVI273) were dissociated using 0.5 mM EDTA (ThermoFisher Scientific) in PBS without CaCl<sub>2</sub> or MgCl<sub>2</sub> (Corning) for 7 minutes at room temperature. The dissociated hiPSCs were plated at a density of  $3 \times 10^5$  cells per well of a Matrigel-coated 12 well plate in mTeSR1 media (StemCell Technologies) supplemented with 2  $\mu$ M Thiazovivin (Selleck Chemicals). After 24 hours, the media was replaced with mTESR1 without Thiazovivin and was replenished daily for 3-5 days until the cells reached  $\sim$  90% confluence. Cardiomyocytes were differentiated by methods previously described [85, 86]. At day 25, cells were dissociated using 10x TrypLE (ThermoFisher Scientific) and plated onto Matrigel-coated 384-well tissue culture plates (Greiner Bio-One) at a density of 20,000 cells/well. All experiments were performed day 28 post differentiation.

### **3.2.3 Preparation of WGA Loading Solution and Benchmark Compounds**

Wheat germ agglutinin conjugated to AlexaFluor488 (Thermo Fisher Scientific) dye loading solution and the compound dilutions were prepared prior to manipulation of the cells on the day of imaging. WGA stock solution was made by dissolving in 1x PBS (Corning) to

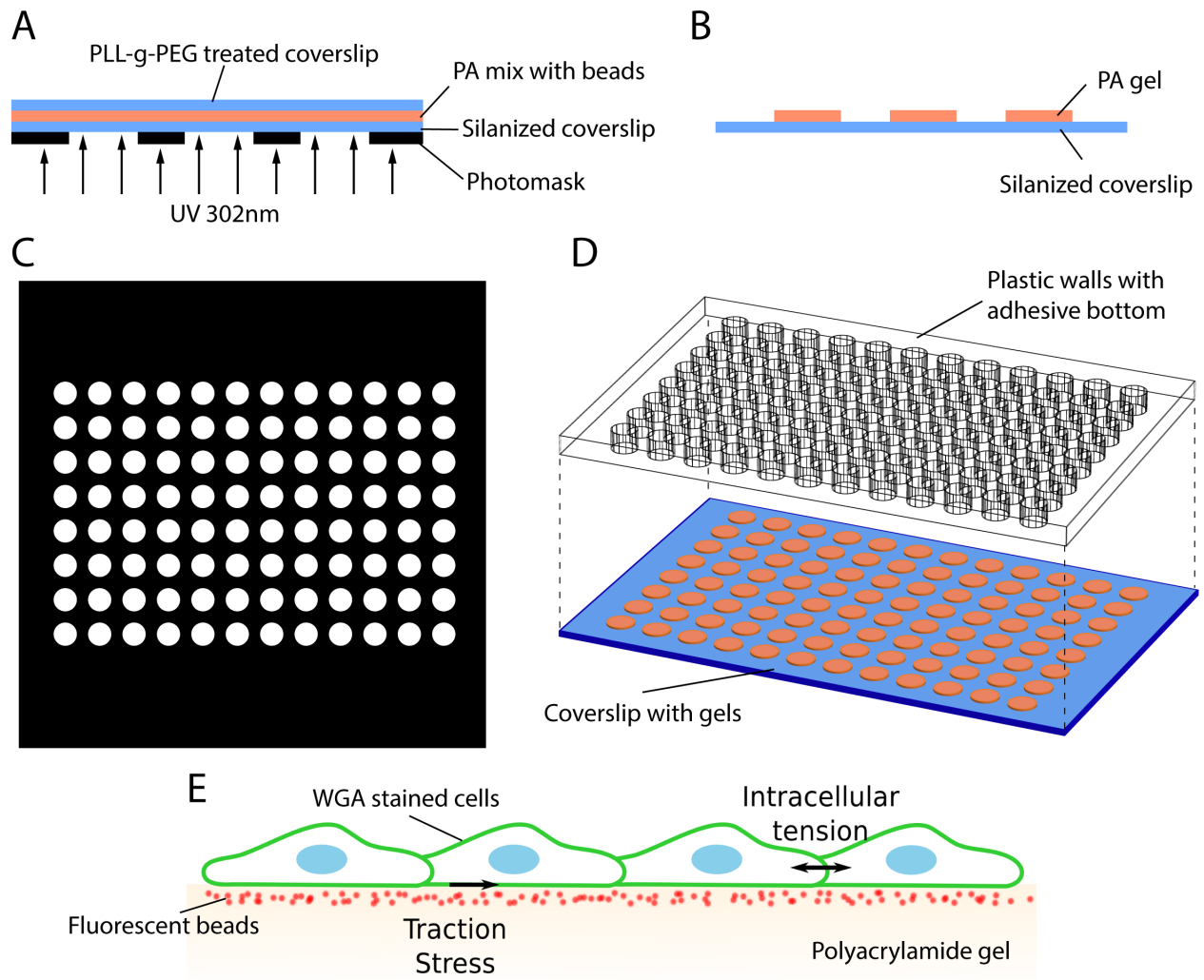


Figure 3.1: Protocol for the fabrication of a 96 well plate with polyacrylamide gels at the bottom. A) Sideview representation of the order for a UV light source place at the bottom, the light is blocked in certain regions by the photomask. The polyacrylamide mix is sandwiched between a silanized coverslip and a PLL-g-PEG treated coverslip. B) After UV curing, the gels have only polymerized in the illuminated areas, the PLL-g-PEG has been peeled off and the gels are bonded to the silanized coverslip. C) Detail of the photomask that creates circular gels of 5mm, distributed for SBS compatible 96 well plate standard. D) Sidewalls with an adhesive bottom are mounted to the glass coverslip, sealing a gel per well. E) Representation of a cardiomyocyte monolayer seeded on top of a polyacrylamide gel embedded with fluorescent beads.

a concentration of 5 mg/mL. WGA stock solution was then diluted into Fluorobrite solution (Thermo Fisher Scientific) containing 5  $\mu\text{g}/\text{mL}$  Hoechst 33258 (Thermo Fisher Scientific) to a concentration of 20  $\mu\text{g}/\text{mL}$  for prior to application of hiPSC-CMs. This solution was a 2x concentrated of dye loading solution that was then applied to hiPSC-CMs. Reference compound isoproterenol (Tocris) and MYK-461(Myokardia) were diluted in DMSO. Each compound was diluted in Fluorobrite solution to a 2x concentrated stock and was warmed to 37°C using a dry heat block prior to application to hiPS-CMs.

### **3.2.4 Loading of WGA Dye Solution and Automated Image Acquisition**

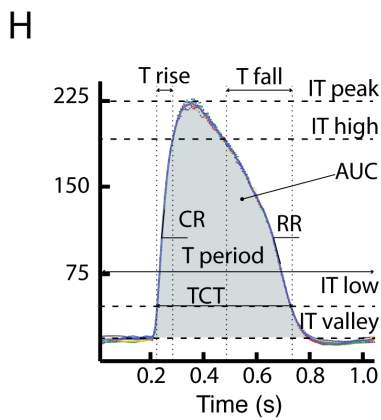
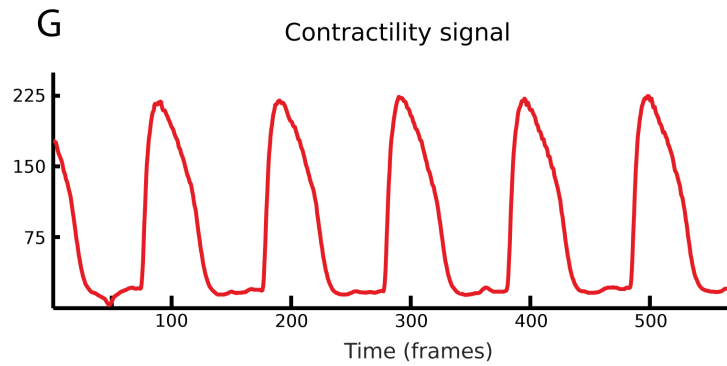
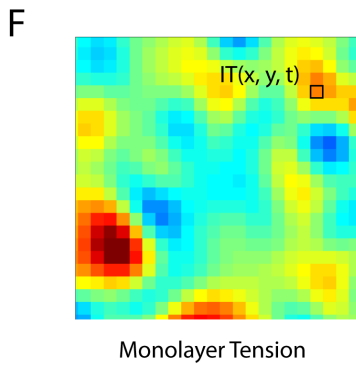
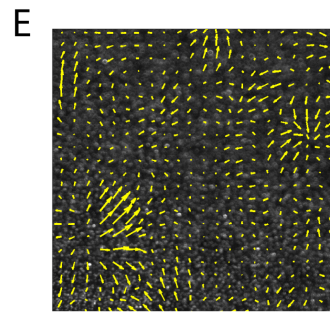
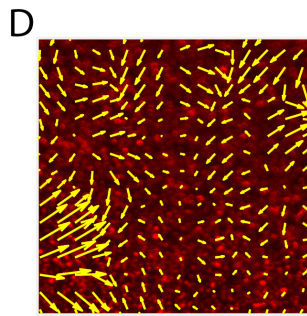
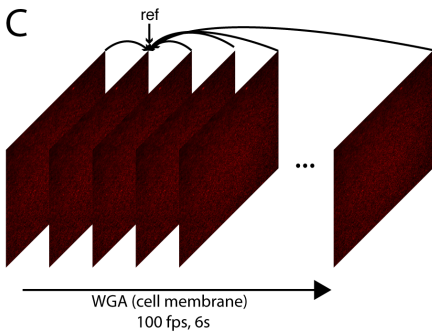
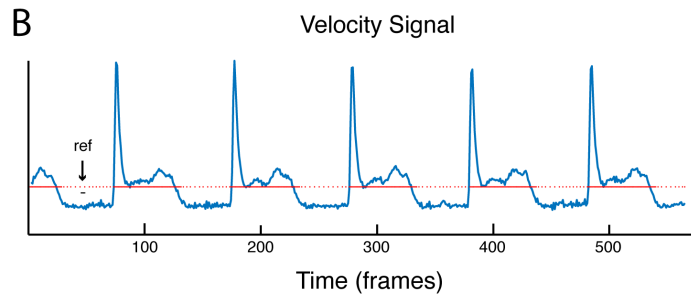
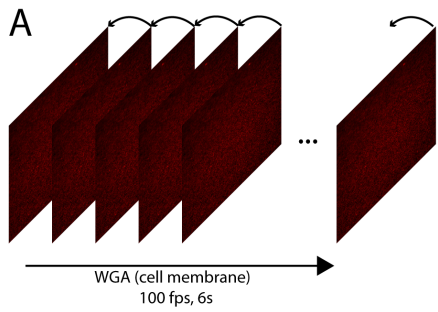
hiPSC-CMs were removed from a 37°C 5% CO<sub>2</sub> incubator and placed immediately into in a tissue culture cabinet on a dry heat block set to 37°C to prevent temperature fluctuation during the subsequent washing and dye loading steps. All subsequent manipulations were conducted on a 37°C dry heat block. Fluorobrite solution was warmed to 37°C in a water bath. To wash the cells and remove the media, 50  $\mu\text{L}$  of media was removed and replaced with 50  $\mu\text{L}$  of Fluorobrite solution five times using a 16 channel pipette at flow rate of 35  $\mu\text{L}/\text{second}$ . After the fifth wash, 50  $\mu\text{L}$  of the 2x WGA dye loading solution was added to each well. The plate was placed back in the 37°C 5% CO<sub>2</sub> incubator for 15 minutes. After the 15 minute incubation, the cells were washed 4 more times by removing 50  $\mu\text{L}$  of Fluorobrite/dye solution from the well and adding 50  $\mu\text{L}$  of fresh Fluorobrite to the well and repeating. After washing, the cells were placed back in a 37°C 5% CO<sub>2</sub> incubator for 10 minutes to recover. After recovery, 50  $\mu\text{L}$  of solution was removed and 50  $\mu\text{L}$  of 2x reference compound was added to the respective well and incubated at 37°C and 5% CO<sub>2</sub> for 5 minutes before image acquisition. Time series images were acquired automatically using the IC200 KIC instrument (Vala Sciences, California, USA) at an acquisition frequency of 100 Hz for a duration of 5 seconds, with excitation wavelength of 485/20 nm and emission filter 525/30 nm using a 0.75 NA 20x Nikon Apo VC objective. A single image of the Hoechst was acquired after the time series.

### 3.2.5 Automated Quantification of Deformation in Polyacrylamide Gels

We developed a fully automated algorithm that retrieves relevant information regarding cardiomyocyte contractility from high-framerate videos. During contraction, the cells deform the polyacrylamide substrate. Those deformations of the substrate are measured using Particle Image Velocimetry (PIV) where the beads embedded in the polyacrylamide gel act as tracers (3.1 E).

In order to obtain the deformations that the cells exert on the gel during contraction it is required to compare each frame of the acquisition to a reference frame where the cells are at a relaxed state i.e. they are not contracting. For cells undergoing spontaneous contractions, this information is not known a priori. To automatically select the reference frames, the algorithm does a first run of PIV on each frame using the previous one as reference (3.2 A), yielding instantaneous velocity fields. Next, the velocity signal (3.2 B) is computed as the spatial average of the magnitude of the velocity field. Typically the velocity signal presents two distinct peaks of similar or distinct amplitudes that correspond to maximum rates of contraction and relaxation. There are also two periods where the velocity signal takes low values. The longer period of time corresponds to the beating frequency of the cells. The shorter one corresponds to the time lapse that the cells spend in a contracted state, without significant motion. In order to robustly identify the periods of relaxation  $\hat{\text{A}}\text{S}$  versus the short periods at which the cells are still and contracted- the velocity signal is first window-averaged in time. The reference frame is selected as that of minimum window-averaged signal (black arrow, 3.2 B). Optionally, more than one reference frame can be selected in order to perform phase-averaged PIV. In addition, the velocity signal can be further utilized to reduce the computational expense of the next step by just focusing the analysis on those frames where cell contraction has been detected and skipping those where the cells are at a relaxed estate. Finally, all the frames of the video are compared to the selected reference frame (3.2 C), yielding instantaneous deformation fields (3.2 D).

Figure 3.2: A) PIV analysis is performed in each frame paired to the previous one. B) The velocity signal resulting from first pass is used to select reference frames and -optionally - alleviate computational effort by skipping further analysis in those frames where the cells are not contracting. C) PIV is executed to measure deformations in the selected frames using the chosen reference frame. Example of a deformation map (D), traction force field (E), intracellular tension (F), contractility signal (G), and retrieved parameters (H) from one experiment. (I) Table summarizing physical meaning and abbreviation of each parameter.



T period = 1.026 s  
 T rise = 0.059 s  
 T fall = 0.254 s  
 TCT = 0.504 s  
 IT peak = 212.3 Pa  
 IT high = 185.4 Pa  
 IT low = 59.8 Pa  
 IT valley = 32.9 Pa  
 AUC = ???  
 CR = 0.221 s<sup>-1</sup>  
 RR = -0.065 s<sup>-1</sup>

**I**

Meaning	Abbr.
Peak Value of Signal	Speak
Baseline Value of Signal	Svalley
90% Amplitude Value	Shigh
10% Amplitude Value	Slow
Beating Period	Tperiod
Total Contraction Time	TCT
Contraction time (from 10% to 90%)	Trise
Relaxation time (from 10% to 90%)	Tfall
Maximum contraction rate	CR
Maximum relaxation rate	RR
Area under the curve	AUC

### 3.2.6 Dynamic Monolayer Force Microscopy

The traction stresses (3.2 E) are determined from the measured deformations by solving the partial differential equations of equilibrium for the polyacrylamide substratum, which behaved like a linearly elastic medium, as previously described [37, 38]. Dynamic analysis of the deformation allows for the traction stresses to be determined during several contraction cycles without removing the cells from the gels. The cumulative intracellular tension (3.2 F) transmitted through the cell sheet were determined by solving the Kirchhoff-Love equations of mechanical equilibrium for a thin elastic plate subject to the forcing created by the measured traction stresses, using previously described methods [14, 21]. Finally, the time-dependent contractility signal (3.2 G) is computed as the average value of the magnitude of the intracellular tension for each frame. Furthermore, in those instances where the cells present a robust periodic behavior, we have developed a phase averaging algorithm (see Appendix) that produces a canonical peak representative of the contraction 3.2 H. From that canonical peak, we measure relevant contractility metrics explained in 3.2 I.

### 3.2.7 Cell Deformation Measurement and Contractility Signal

Alternative to TFM, several studies have reported cell contraction from directly measuring motion of the cells [73–76]. Our algorithm can also be employed to obtain contractility parameters from measuring the motion of the cell membrane. To do so, we stained the cells membrane with wheat germ agglutinin (WGA) and acquired videos of the same area than the imaged for TFM. We identified reference frames and run PIV in a similar fashion to that used for analyzing the gel deformations. After completion, the yielded result is the time-resolved deformation of the monolayer during contraction (3.3 D). We computed local changes in area -i.e. contracting / stretching - by taking the divergence on the deformation fields (3.3 E). The divergence operator is numerically implemented with centered finite differences. The contractility signal (3.3 F) is computed as the average value of the magnitude of the divergence field for each frame. The phase averaging algorithm can be employed to reconstruct a canonical peak 3.3 G and retrieve contractility metrics.



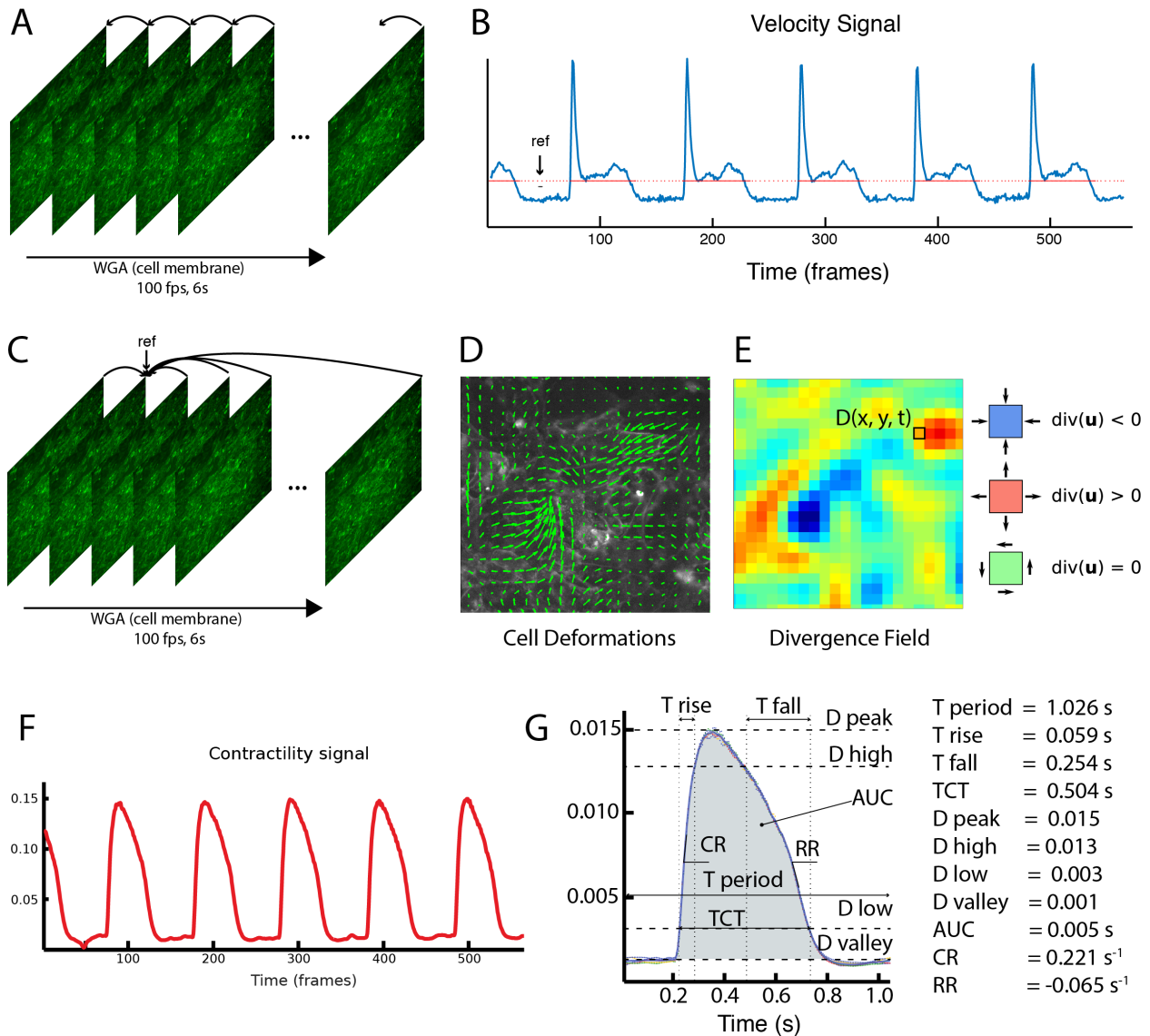


Figure 3.3: A) PIV analysis is performed in each frame paired to the previous one. B) The velocity signal resulting from first pass is used to select reference frames. C) PIV is executed to measure deformations in the selected frames using the chosen reference frame. Example of a deformation map (D), divergence field (E), contractility signal (F) and retrieved parameters (F) from one experiment.

### 3.2.8 Elastography

Elastography aims to map and quantify elastic properties and stiffness of tissue, based on processing the deformation of a tissue when loaded under a known force. Following the workflow summarized in 3.4, we propose to combine the intracellular tension and divergence maps, to evaluate the mechanical properties of the cells.

In DMSM, the cells are modeled as a thin, elastic membrane of uniform thickness and elastic modulus. Under those assumptions, the intracellular tension ( $IT$ , 3.4 E) is proportional to the divergence field ( $D$ , 3.4 D).

$$IT = kD \tag{3.1}$$

where  $k$ , represents the bulk modulus of the cells. Given measurements  $IT$  and  $D$ , we can estimate  $k$  from a simple least squares approximation

$$J = \sum_i \frac{(IT_i - kD_i)^2}{\sigma_{IT} + k\sigma_D} \tag{3.2}$$

$\sigma_{IT}$  and  $\sigma_D$  are the errors in the measurement of  $IT$  and  $D$ , respectively. Because the measurement errors are unknown, they have been approximated as the standard deviation of  $IT$  and  $D$ . The minimization problem above is highly over determined (for our experiments,  $\sim 4000$  data points in one field of view and 1 fitting parameter 3.4 F, gray dots). One of the current limitations of DMSM is the lack of knowledge of the correct boundary conditions at the edge of the image [21]. This is due to the lack of information about the value of the tension that the cells at the edge of the images are exerting on to the imaged ones. In contrast to  $IT$ , the measurements of  $D$  are obtained from direct differentiation of the data and thus do not contain boundary artifacts. We propose to relax the discrepancies at the boundary between  $IT$  and  $D$  by introducing point forces at each of the points at the edge of the image. Therefore, in a field of view with  $N \times M$  datapoints, we will fit  $2N+2M+1$  parameters.

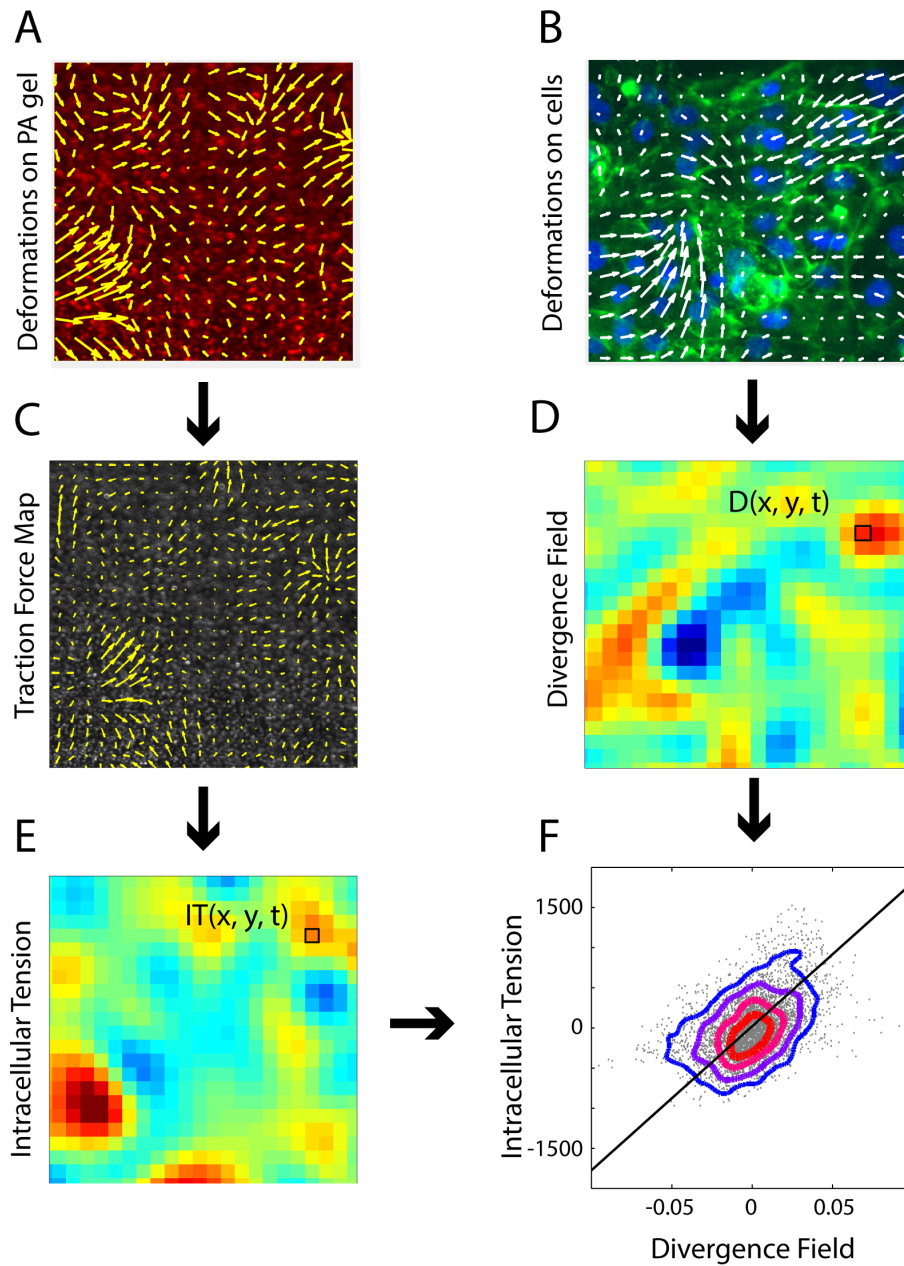


Figure 3.4: Workflow describing crucial steps for elastography. From the deformation field measured by tracking the fluorescent beads in the gel (A), the traction stresses (C) and intracellular tension (E) are computed. From the deformation field measured by tracking the deformations of the cells membrane (B), the divergence field is computed (D). The relationship between IT and divergence provides information about the mechanical properties of the cell (F). The bulk modulus of the cells corresponds to the slope of a linear fit of the data (solid line, F)

## Examples of $F_j$

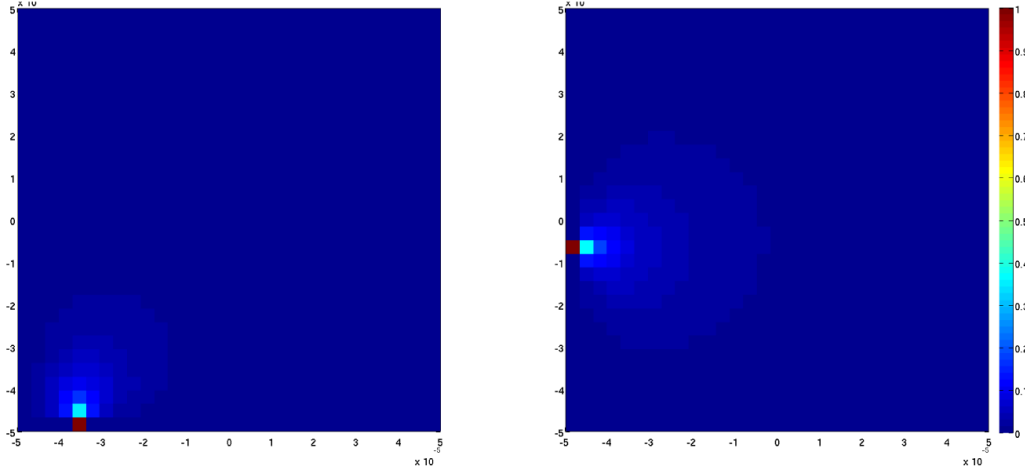


Figure 3.5: Example of the intracellular tension fields generated by a point force located at two different edge points.

$$J = \sum_i \frac{(IT_i - kD_i + \sum_j \lambda_j F_j)^2}{\sigma_{IT} + k\sigma_D} \quad (3.3)$$

Where the index  $i$  denotes all the points in the field of view and  $j$  are only those points at the edge of the field.  $F_j$  is the tension field resulting from a point force located at  $(x_j, y_j)$ , pulling outwards of the domain normal to the edge. This tension field is obtained by solving the Poisson equation

$$\nabla^2 F_j = 0, \quad (3.4)$$

with boundary conditions  $F_j$  at the edge point  $j$  with coordinates  $(x_j, y_j)$ , and  $F_j = 0$  at other edge points. 3.5 shows two examples of the resulting tension field  $F_j$  for two different edge point force loads. The fit parameters  $k$  and  $\lambda_j$  of the cost function  $J$  were found numerically using gradient descent.

To validate the improvement of the boundary correction method, we set up the following strategy. From the displacements measured from a beads video (3.6 A), we compute the  $IT$  field (3.6 B). From those results, we crop the middle region, which will be considered

the ground truth  $IT$  field (3.6 C) that we aim to recover. For this idealized case, we generate the strain field (3.6 D) by simply dividing the  $IT$  by an arbitrary bulk modulus. Then, the question that we aim to answer is, how well does the algorithm recover the  $IT$  field and bulk modulus from cropped displacement data (3.6 A highlighted). The first step is to compute the  $IT$  without any boundary correction (3.6 E). After execution of the boundary correction method, the estimated boundary conditions (3.6 F) improved the recovered  $IT$  field (3.6 G). Notice that, because the strain data inputted in the method is idealized, all the datapoints should follow a linear stress-strain relationship with slope the bulk modulus (3.6 E' and G'). There is a significant improvement of the recovered  $IT$  field, in particular for the points at the boundary (3.6 E' and G', red points).

It is important to note that, both  $IT$  and  $D$  must be representative of the same time point within the contraction cycle. In our system, the measurements of cell deformations (from which we computed  $D$ ) are not acquired simultaneously with that of the gel deformations (that led to  $IT$ ). To overcome this limitation, we developed an algorithm for the reconstruction of deformation fields for one single contraction described in the section Reconstruction of Phase Average Deformation Maps in the Appendix.

### 3.3 Results

To illustrate the ability to capture the effect of drugs and application of the method, we have fabricated a 96 well device with polyacrylamide gels and cultured monolayers of hIPS-CM. The cells were spontaneously beating at the time of recording. We tested our platform to evaluate the capacity of making dose response curves from the contractility data against isoproterenol, and MYK-461 (mavacamten). The plate was imaged twice: before the cells were subject to any treatment, and after the corresponding dose of compound was added. Hence, for each well we obtained 4 different videos: before and after treatment, and beads and cell membrane channels. In this way, the results of the contractility analysis before treatment can be used as internal control after the compound was added.

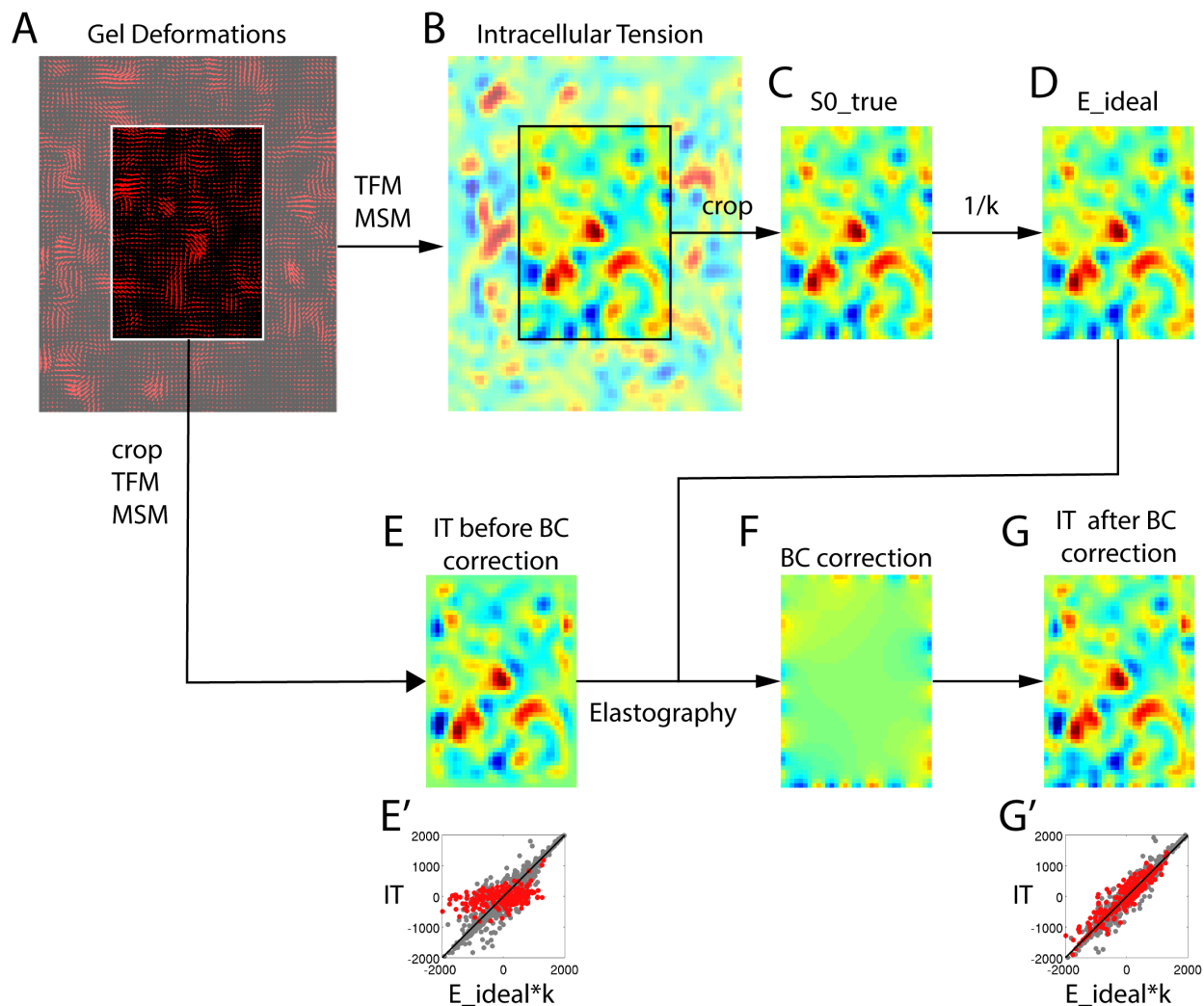


Figure 3.6: Validation of the boundary correction method. The ideal case was generated in the following manner. Using the deformation field measured in an experiment (A), the intracellular tension ( $IT$ ) field (B) was computed. A subregion  $IT$  field was then cropped (C,  $S0_{true}$ ) and the ideal strain field (D) was computed by using the relationship  $E_{ideal} = 1/k * S0_{true}$ . Where  $k$  is an arbitrary bulk modulus of the cells. The method was tested by cropping a section of the deformation field (A, highlighted region) and further used to compute the intracellular tension with the cropped data (E). The resulting  $IT$  map contains boundary effects that affect the correlation with  $E_{ideal}$  (E') specially at the points at the edge of the box (red points). The elastography/boundary condition method was then used to recover  $k$  and correct the errors at the boundary. After convergence, the algorithm has found a correction (F) that improves the comparison between  $IT$  maps (compare G with C), specially to those points at the edge of the field (red points, G').

### 3.3.1 Measurement of Drug Response Against Benchmark Compounds

MYK-461, is a myosin inhibitor currently in clinical trials for the treatment of hypertrophic cardiomyopathy. MYK-461 reduces contractility by decreasing the ATP activity of the cardiac myosin heavy chain. Due to this mechanism, the effect of this drug can't be studied using action potential or calcium kinetics assays. The effect in cardiomyocyte contractility is a decrease in overall contractile force. 3.7 A shows 4 representative traces of contractility analysis results before (gray) and after (red) treatment for doses: baseline, 0.01 $\mu$ M, 1 $\mu$ M, and 10 $\mu$ M, see 3.8 and 3.9 for all the traces. The traces were further processed with our parameter retrieval algorithm. The quantification is then plotted as a dose-response 3.7 B or heatmap 3.7 C where the color indicates fold-change of each metric.

Isoproterenol is non-selective beta-adrenoreceptor agonist, analog of epinephrine that is used for the treatment of bradycardia and heart block. The effect of isoproterenol is to increase cardiac frequency (decrease  $T_{\text{peak}}$ , 3.7 D-F).

The acute treatment of either MYK-461 or isoproterenol did not have a significant impact in the bulk modulus of the cells (last row 3.7 C, F). As it can be observed, there is some variability between the control traces before and after treatment, particularly affecting the contraction kinetics (increase in  $T_{\text{rise}}$  and decrease in CR). We suspect that this changes may be due to the fact that extra medium was added to each well in order to add the compound solution.

### 3.3.2 Comparison of Membrane and Substrate Deformation Measurements

The data set comprising all the wells before the drugs were added can be used to further extract statistics of the metrics of the analysis. We first questioned the relationship between the metrics obtained from the contractility signals measured from the substrate deformations compared to those obtained from membrane deformations. In order to answer that question we built a correlation matrix between all the metrics of both channels (3.10).

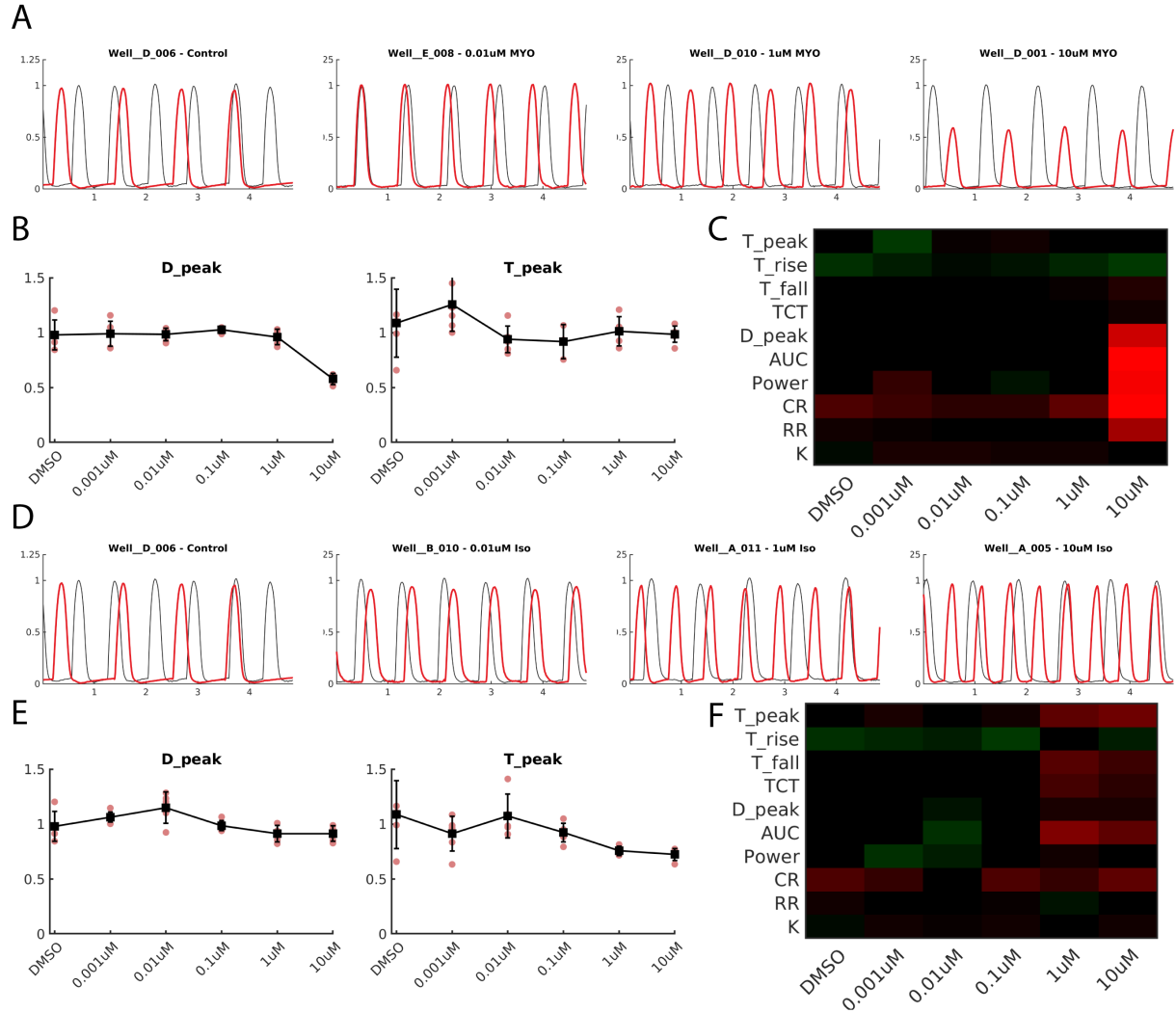


Figure 3.7: Contractility signals of hIPS-CM monolayers as response to different doses of (A) MYK-461 and (D) isoproterenol (left to right: baseline, 0.01 $\mu$ M, 1 $\mu$ M, and 10 $\mu$ M) . Gray: before treatment. Red: after treatment. The amplitude of each trace was normalized with the D\_peak before treatment. Representative dose-response curves of peak contraction D\_peak, and time between peaks T\_peak (B, MYK-461; E, isoproterenol). Heatmap summarizing dose-response changes for all different metrics(C, MYK-461; D, isoproterenol).



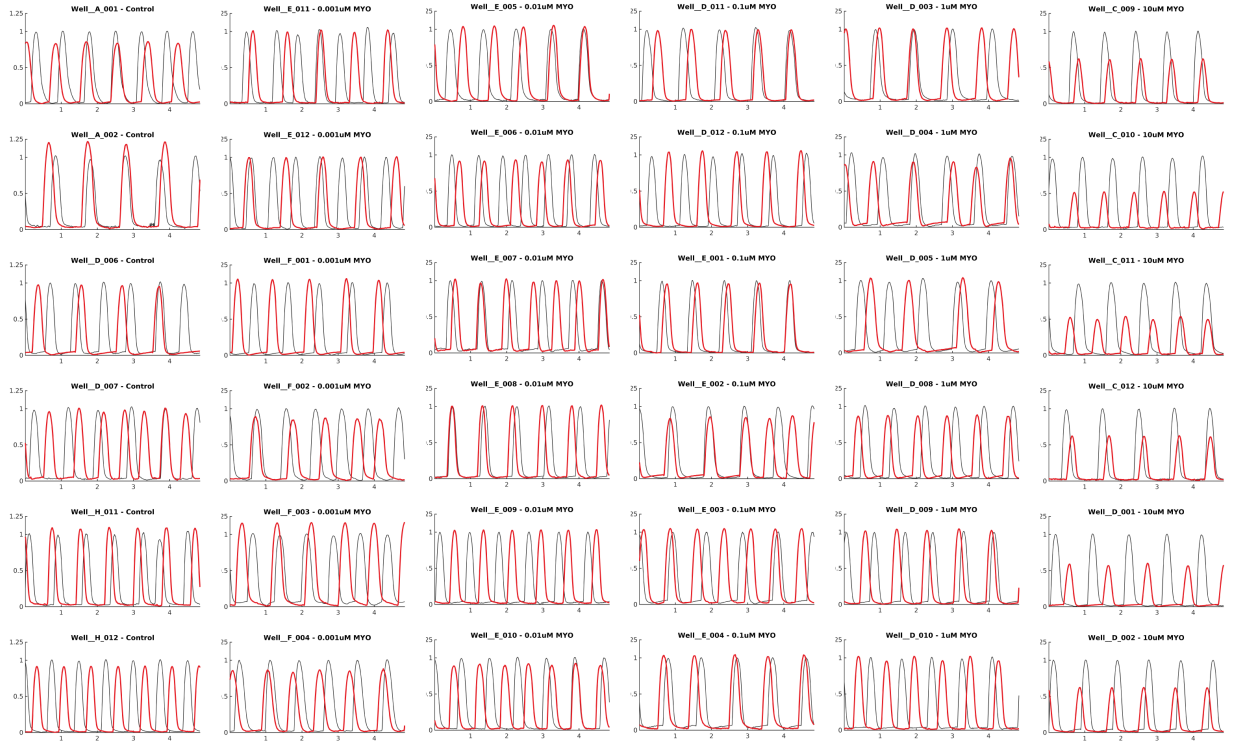


Figure 3.8: Contractility traces before (gray) and after (red) treatment with MYK-461. Dose concentrations increase by column (Baseline,  $0.001\mu\text{M}$ ,  $0.01\mu\text{M}$ ,  $0.1\mu\text{M}$ ,  $1\text{M}$ , and  $10\text{M}$ ).

In general there is a strong correlation between metrics measured from the substrate deformations compared to that same metric measured from cell deformations. The correlation matrix, also provides information inter-metric correlations. As could be expected, the time metrics correlate best among themselves ( $T_{\text{peak}}$ ,  $T_{\text{rise}}$ ,  $T_{\text{fall}}$ , and  $TCT$ ). Metrics that depend on both the amplitude ( $D_{\text{peak}}$ ) and time duration of the peak ( $TCT$ ), such as  $AUC$  and  $Power$  seem to be more dependent on the amplitude than on the duration of the peak.

Next we proceeded to elucidate the relationship between intracellular tension and divergence. This question is analog to asking whether or not the amplitude of the contractility signal can be used as a surrogate of force production. To answer this question we pooled data from all the wells at peak contraction and pre-multiply the divergence with the measured bulk modulus of each experiment. In the ideal case of the cells being perfectly linearly elastic and no measurement errors, the data should fit in a straight line of slope unity and zero ordinate at the origin. Each pair of measurements of  $IT$  and  $D$  is represented as a dot in the scatter



Figure 3.9: Contractility traces before (gray) and after (red) treatment with MYK-461. Dose concentrations increase by column (Baseline,  $0.001\mu\text{M}$ ,  $0.01\mu\text{M}$ ,  $0.1\mu\text{M}$ ,  $1\mu\text{M}$ , and  $10\mu\text{M}$ ).

plot in 3.11 A. The black line in the plot as fit assuming error in the measurements in both  $x$  and  $y$  (as described for the elastography section), yielding a fit  $IT = 1.0676kD + 0.0026$ . The curve lines are iso-probability lines containing 90%, 75%, 50%, and 25% of all the data. In addition, we constructed a Bland-Altman plot (3.11 B) to look for possible biases of one measurement versus the other. As it can be seen from the density lines, the data doesn't show any bias away from the origin, suggesting that in first approximation, there is a linear relationship between  $IT$  and  $D$ .

### 3.4 Discussion

Functional screening assays of contractile force generation of iPSC-CM pose great potential for new cardiac drug development, drug cardiotoxicity, and in vitro modeling of cardiac disease [31]. Existing high-throughput assays for cardiac contractility rely on the measurement of surrogate variables such as the motion of the cells, and changes in the in-

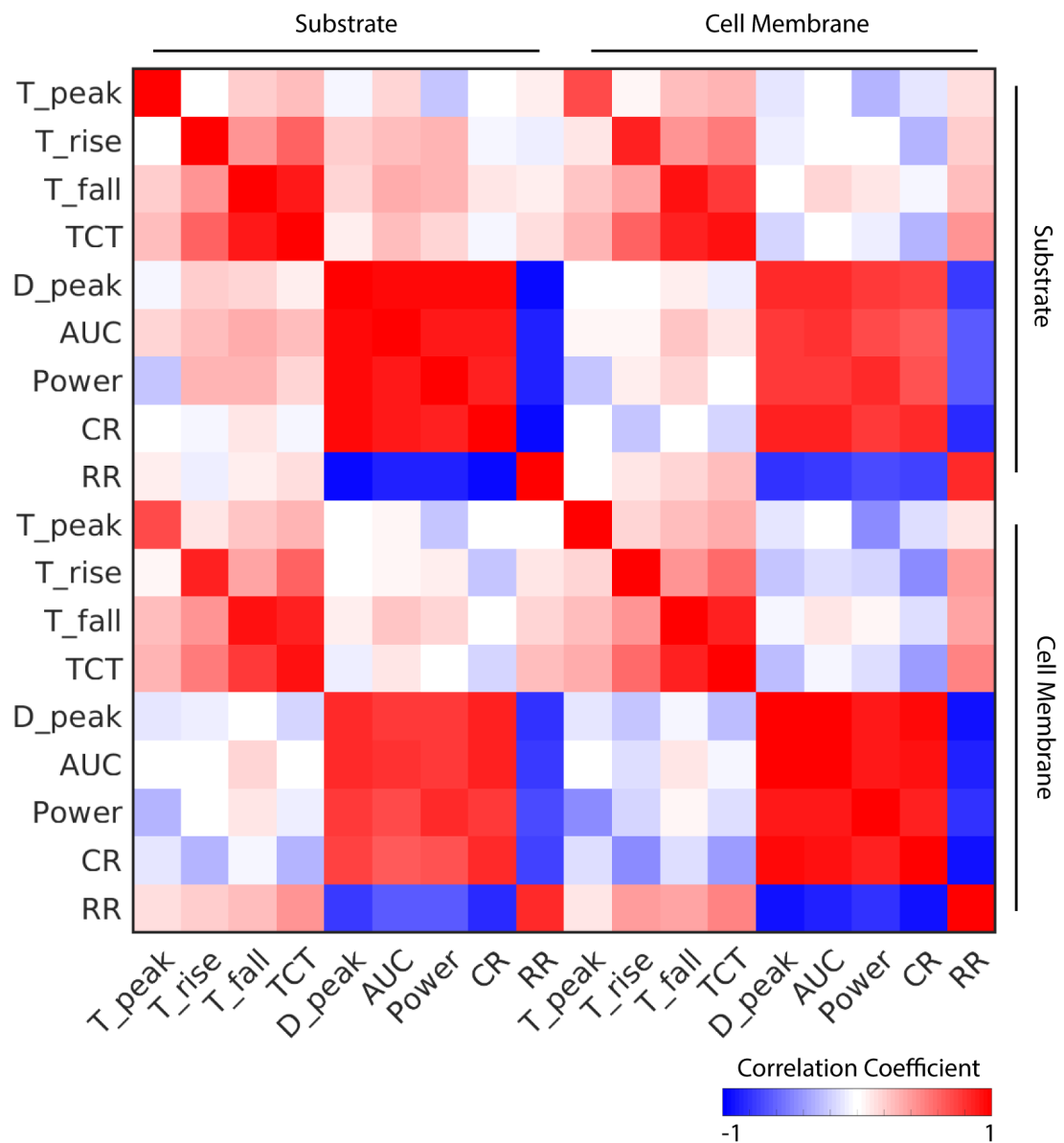


Figure 3.10: Correlation matrix across the metrics retrieved by the contractility analysis and the video analyzed (that of the substrate deformations from the beads images or the cell membrane deformations from the WGA stain).

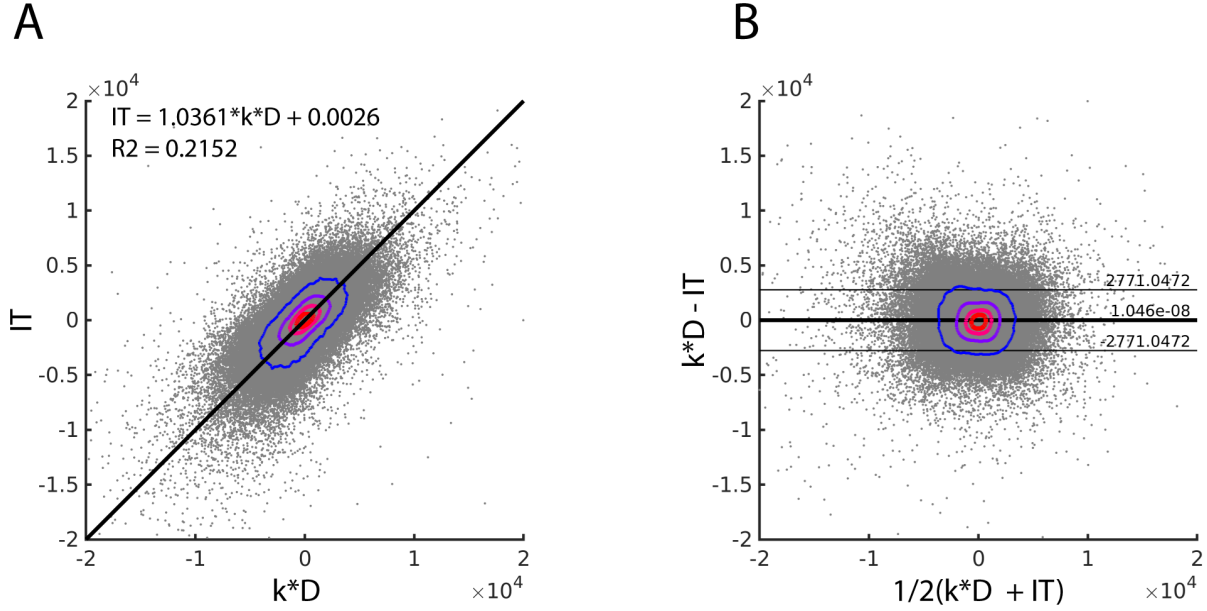


Figure 3.11: Scatter (A) and Bland-Altman (B) plots, of bulk modulus times divergence ( $k * D$ ) against intracellular tension ( $IT$ ) for all the experiments before drug treatment, at the moment of maximum contraction.

tensity of the image [73–75]. Moreover, all these assays have been realized on a stiff surface such as glass or plastic. In contrast, substrate stiffness is a feature that has proven to be of relevance, especially for iPSC maturity [78]. Monolayer Stress Microscopy is a powerful tool for the quantification of collective force generation and transmission. However, up to this date, there hasn’t been any attempt to implement MSM in high-throughput. In addition to precise measurements of force generation, there is a lack of functional assays that aim to quantify cardiomyocyte stiffness. The lack of stiffness-based assays contrasts with the increasing interest in myocardial mechanical properties [83], which has been associated with cardiac diseases affecting the heart’s relaxation during diastole [80].

In this paper we presented a protocol to manufacture SBS compatible 96 well plates with polyacrylamide gels that can be imaged with any standard High Content Screening system, enabling the realization of MSM measurements in high-throughput. The stiffness of the gels of our device can be tuned by changing the ratio of acrylamide and bis-acrylamide or, alternatively, the UV curing time, as shown before by other groups [49, 87].

Next, we developed automatized reference selection algorithms to remove the need

of manually selecting a reference frame for measuring deformations with PIV. The selection is based on finding those frames where the monolayer presents less average motion and is presumed to be at a relaxed state. The identification of frames corresponding to relaxation or contraction allows to effectively diminishing computational time without any loss of information during the contraction event. PIV is well suited for parallelization in multiple cores or GPU. If the monolayer is undergoing periodic beating, we have further developed a phase reconstruction algorithm that finds a canonical deformation map based on a Fourier decomposition of the multiple cycles acquired in the video.

The deformation maps of the polyacrylamide gels are further analyzed with MSM, yielding time-resolved two-dimensional maps of intracellular tension. The time-dependent contractility signal is defined as the spatial average magnitude of intracellular tension. From this signal we extract representative metrics such as magnitude and period of the signal as well as duration of duration of contraction. These metrics are calculated for each well, providing a quick summary for each experimental condition.

In addition to the deformations of the substrate, we can also extract relevant features of the contraction from measuring the deformations of the cell. For this purpose we added fluorescently labeled WGA to live stain the cells's membrane. Similarly to the substrates, the automatic reference selection can be used to extract reference frames to then execute PIV to measure the deformation fields of the cells during contraction. The divergence of the deformation fields can be calculated with direct differentiation, obtaining maps of local change of area. Computing the spatial average of the magnitude of the field reduces the dimensionality of the divergence maps into a time-dependent contractility signal.

We examined the variation of each metric with different concentrations of benchmark compounds with known effects. Our analysis is able to recapitulate both the increase in beating frequency expected from the addition of isoproterenol as well as the decrease in amplitude of contraction caused by the myosin activity inhibitor, MYK-461. The plate was imaged before adding the compounds to obtain internal control values of each plate, reducing the noise caused by well-to-well variability and increasing the sensitivity of the method to drug-induced changes.

We studied the correlation between metrics obtained through the substrate images and those same metrics measured with the cell-membrane images. Overall, the correlation coefficients between same-metric, different-channel is almost unity, signifying that the measurements are robust enough and can be recapitulated from each imaging channel. Correlations between different-metric, same-channel indicated that time-related (T peak, TCT, T rise, T fall) metrics cluster among themselves. Similarly, amplitude-related (D peak, AUC, Power) metrics present higher correlation with those that are also amplitude-related.

The spontaneous contraction of the cells serves to obtain stress-strain (intracellular tension-divergence) curves that are further utilized to obtain an average bulk modulus of the imaged region. This aspect of the analysis may be of significant importance for the study of diseases that affect cardiomyocyte relaxation due to changes in their passive stiffness. Additionally, we proposed a combination of both substrate and cell membrane measurements to correct boundary artifacts that are inherent to MSM at the edge of the field of view.

In conclusion, the presented work provides a high-throughput platform for the study of iPS-CM contractility force and stiffness. The fabrication of the device is simple enough to be implemented in any lab and the substrates' stiffness can be tuned easily. Our platform can be used in drug screening, toxicity, and disease in vitro. To illustrate its validity, we have performed experiments of spontaneously beating iPS-CM seeded on a 96 well plate with PA gels and employed to retrieve changes in force and stiffness against benchmark compounds.

## 3.5 Appendix

### 3.5.1 Implementation of Phase Average Algorithm for Parameter Retrieval

The strategy to extract the relevant contractility features shown in Figure 3.2 is based on the reconstruction of a canonical peak, representative of the multiple imaged contraction cycles during the recording. This algorithm exploits the robust periodicity of the contractility signal (3.12 A) to overlay one peak over another to finally average over the multiple measurements and get one representative peak. The first step of the analysis is to find the

period of the signal ( $T_{\text{peak}}$ ) by computing the autocorrelation of the Contractility Signal (3.12 B), which provides information about the expected distance between a peak and another. All the peaks are aligned using for instance the local maxima (black dots, 3.12 C). The local maxima search algorithm uses the built-in MATLAB function `findpeaks`. To improve accuracy and reduce the false identification of peaks we constrained the peaks to have a height higher than the average of the signal and be at a distance greater than half of the period ( $> T_{\text{peak}} / 2$ ). The contractility signal is then cropped into windows of width  $= T_{\text{peak}}$  with `localMax` located at  $1/3 T_{\text{peak}}$  (3.12 D). The accuracy of the alignment is further improved by removing the lead/lag between individual peaks by calculating the cross correlation between peaks (3.12 E).

### 3.5.2 Reconstruction of Phase Averaged Deformation Maps

In order to perform the elastography step of our method, we require the deformations of both cells and gel to be synchronized, for instance, at maximum contraction D peak. Since the videos of the cells and gels were not acquired simultaneously, we have implemented an algorithm that reconstructs one single beating cycle from the measured instantaneous deformation fields recording during the video. Let's define the averaged deformation field  $\bar{\mathbf{u}}$  to be defined as

$$\bar{\mathbf{u}}(x, y, t) = \sum_{i=0}^{N_h} A_i(x, y) \cos\left(\frac{2\pi i t}{T_{\text{peak}}}\right) + \sum_{i=1}^{N_h} B_i(x, y) \sin\left(\frac{2\pi i t}{T_{\text{peak}}}\right) \quad (3.5)$$

The Fourier coefficients  $A_i$  and  $B_i$  can be computed from the PIV measured deformation field  $\mathbf{u}$

$$A_i(x, y) = \frac{\int \mathbf{u}(x, y, \tau) \cos\left(\frac{2\pi i \tau}{T_{\text{peak}}}\right) d\tau}{\int \cos^2\left(\frac{2\pi i \tau}{T_{\text{peak}}}\right) d\tau} \quad (3.6)$$

$$B_i(x, y) = \frac{\int \mathbf{u}(x, y, \tau) \sin\left(\frac{2\pi i \tau}{T_{\text{peak}}}\right) d\tau}{\int \sin^2\left(\frac{2\pi i \tau}{T_{\text{peak}}}\right) d\tau} \quad (3.7)$$

The number of harmonics  $N_h$  was chosen to match that of applying Akaike's information criterion to reconstruct the contractility signal. After this manipulation, we can retrieve

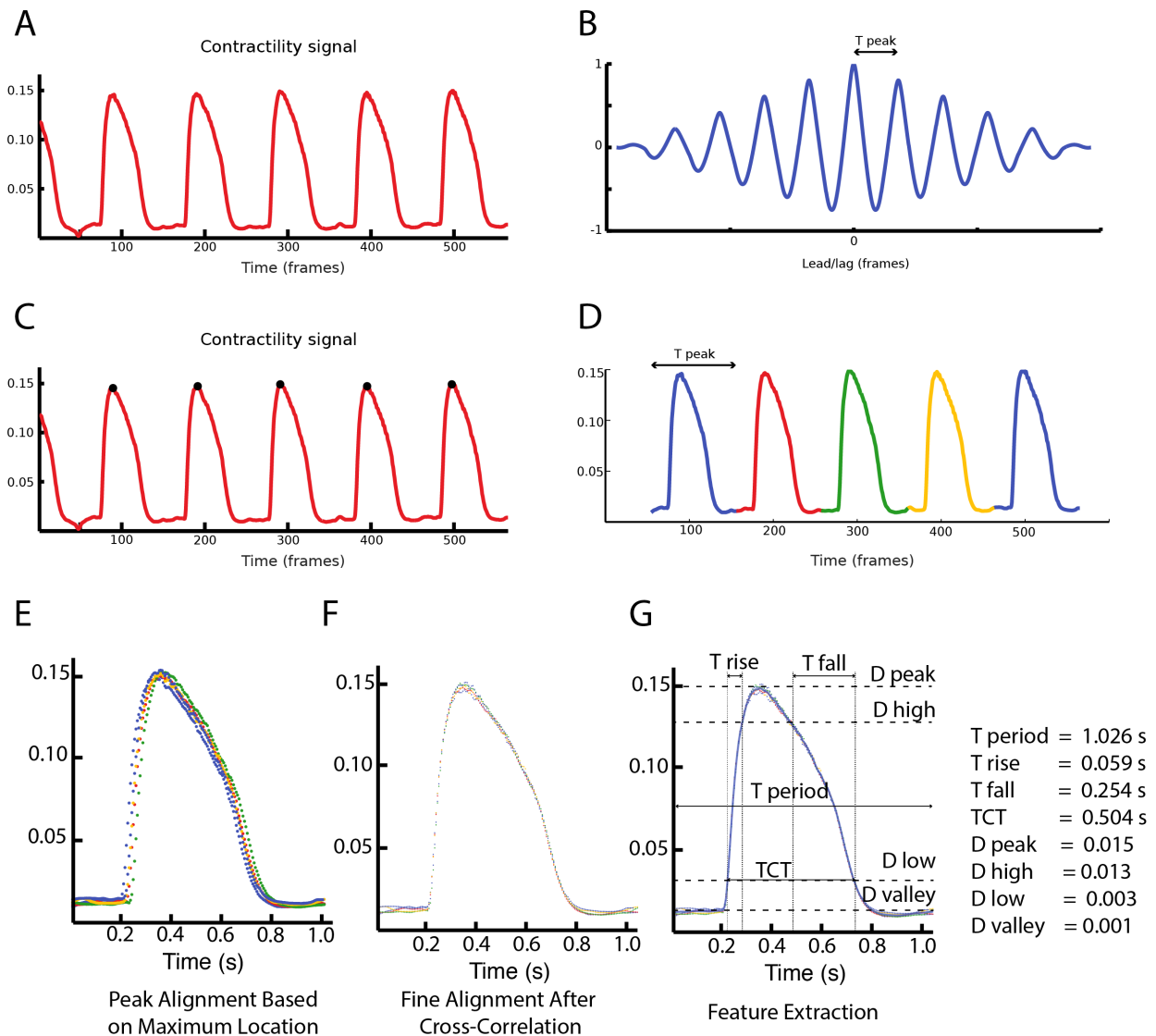


Figure 3.12: Parameter retrieval algorithm for periodic contractility signals. From the contractility signal (A), the autocorrelation signal (B) is computed, estimating the beating period  $T_{peak}$ . The detected local maximum of the contractility signal (C, black dots), are used as guides to window each individual peak (D). All the peaks are collapsed into one (E) and further realigned with by means of cross-correlation between peaks (F). The representative peak (G) is obtained with non-parametric regression and it is further used to measure the different contractility metrics listed on the figure.



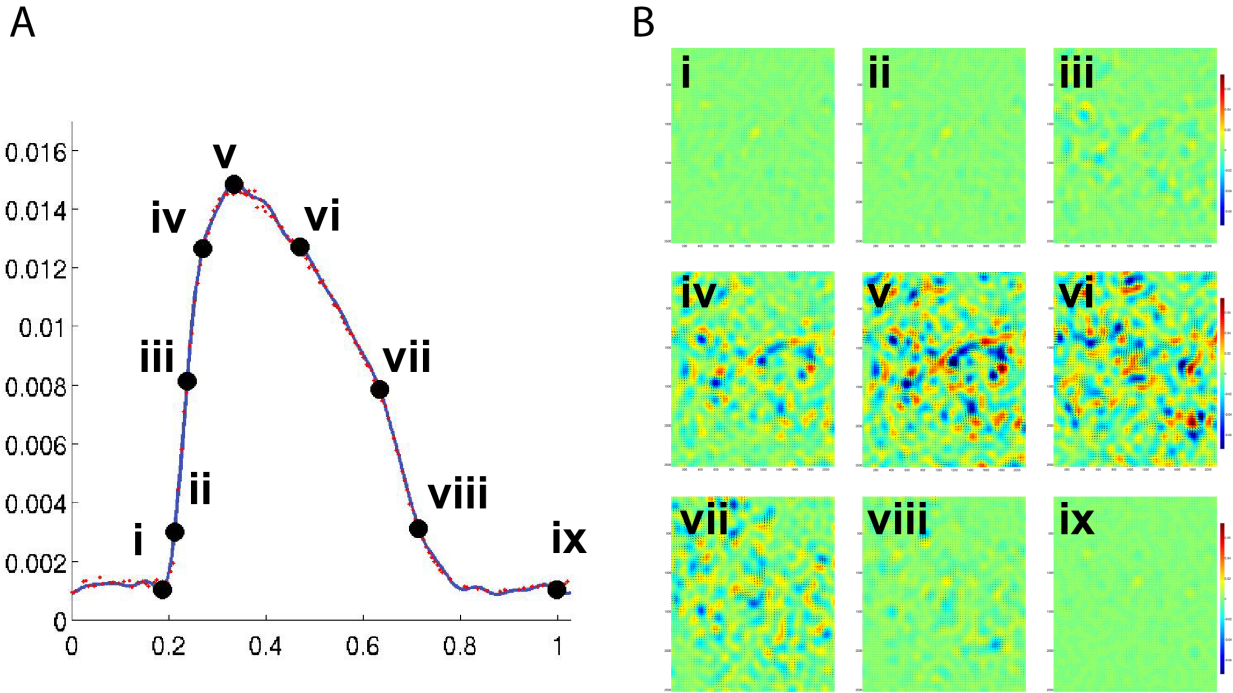


Figure 3.13: Example of results produced by synchronization algorithm. A) Reconstructed contractility peak signal. B) Maps of divergence at different stages of contraction cycle.

the average deformation field at any given time of the contraction cycle (Fig SI2).

### 3.6 User Guide For Contractility Analysis

This User Guide is aimed to provide instructions for running the Cardiomyocyte Contractility Analysis (CCA) described in the previous chapter. The current version is still under development and unexpected errors may arise. Please submit your feedback to [rserrano@ucsd.edu](mailto:rserrano@ucsd.edu).

#### System Requirements

CCA is distributed as a packaged Matlab app. In order to install and run CCA, the user must first install Matlab Runtime R2017b (9.3) available for free for Windows, Linux, and Mac operating systems at [www.mathworks.com/products/compiler/matlab-runtime.html](http://www.mathworks.com/products/compiler/matlab-runtime.html).

CCA is recommended to be executed in a multicore system to take full advantage of

the built-in parallel-computing acceleration.

## Input Files

CCA is optimized to analyze image sequences obtained from a standard High Content Screening system. Currently, CCA only supports .tif format files. The analysis will be run assuming that all the images within a folder belong to the same video and must be analyzed together. In other words, the images are expected to be organized in a single folder per experiment, per well, per condition, and per fluorescent channel.

## Launching CCA

To launch CCA, navigate to the downloaded folder and just double click run\_CCA.sh. The main menu dialog shown in Figure 3.14 should appear.

In order to run CCA, the user must create: a job file, a configuration file, and an alias file, in this specific order. Clicking the button "New" opens a dialog to create a new file. If instead the user is providing an existing file, she can load the file by clicking "Browse".

## Creating a Job File

A job file is a simple-text file that contains a list with all the folders in which the analysis must be executed -i.e. the innermost folder containing the images. In a typical high-throughput experiment, this list may comprise hundreds of folders. Because the folder hierarchy may vary from one HCS system to another, CCA provides a function to list all the sub-folders that contain .tif images recursively and save it as a job file.

The user must first click "Load Data" and navigate to the outermost folder that contains all the subdirectories to be analyzed. After confirmation, CCA will start looking inside each folder and return those folder that contain at least one .tif image. A list of directories should appear in the "Candidate Folders" text box (Figure 3.15).

Optionally the user may not desire to analyzed all of the "Candidate Folders". In that case, the user can type in a particular string in the "Filter" box to construct a list with

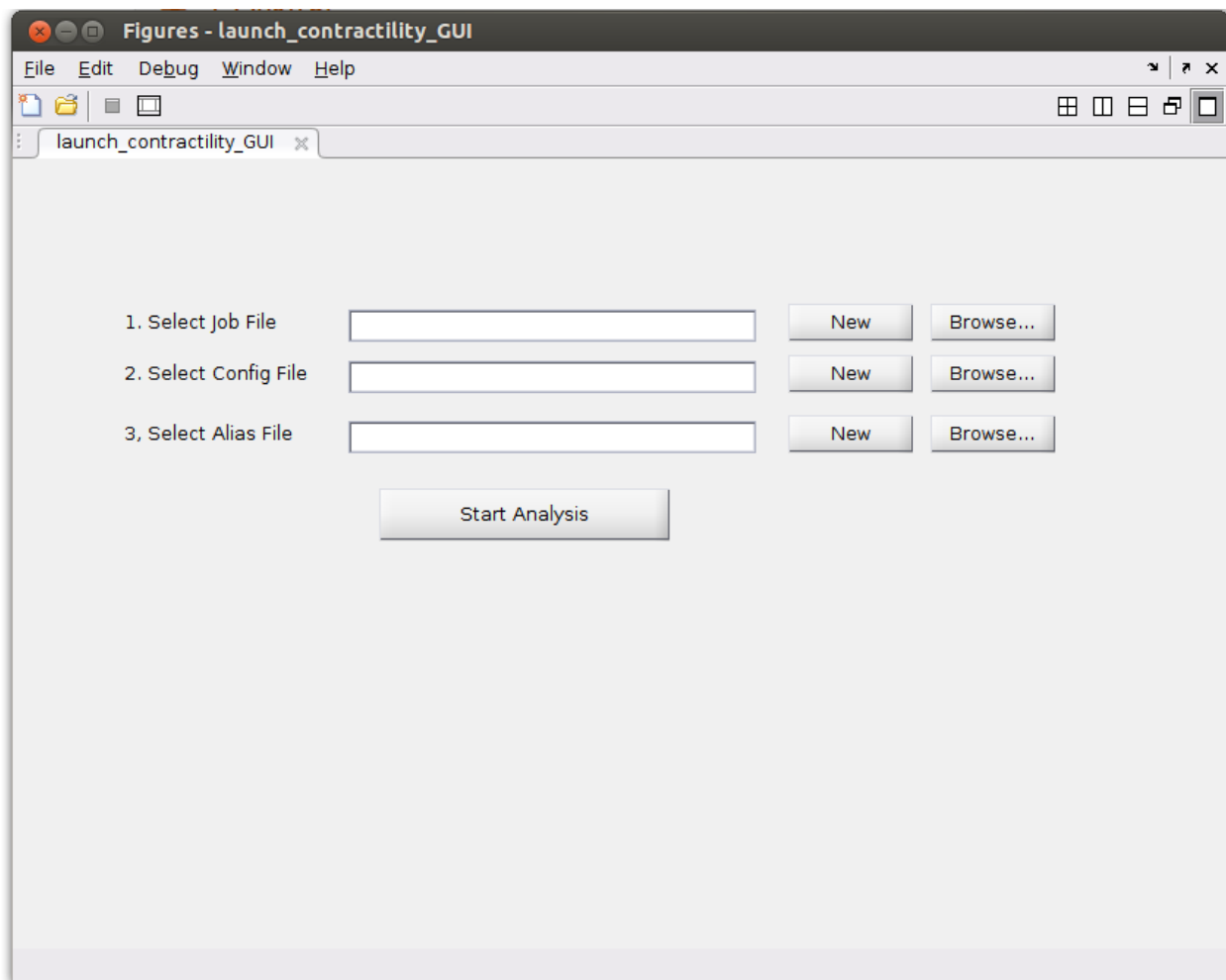


Figure 3.14: Main menu of CCA.

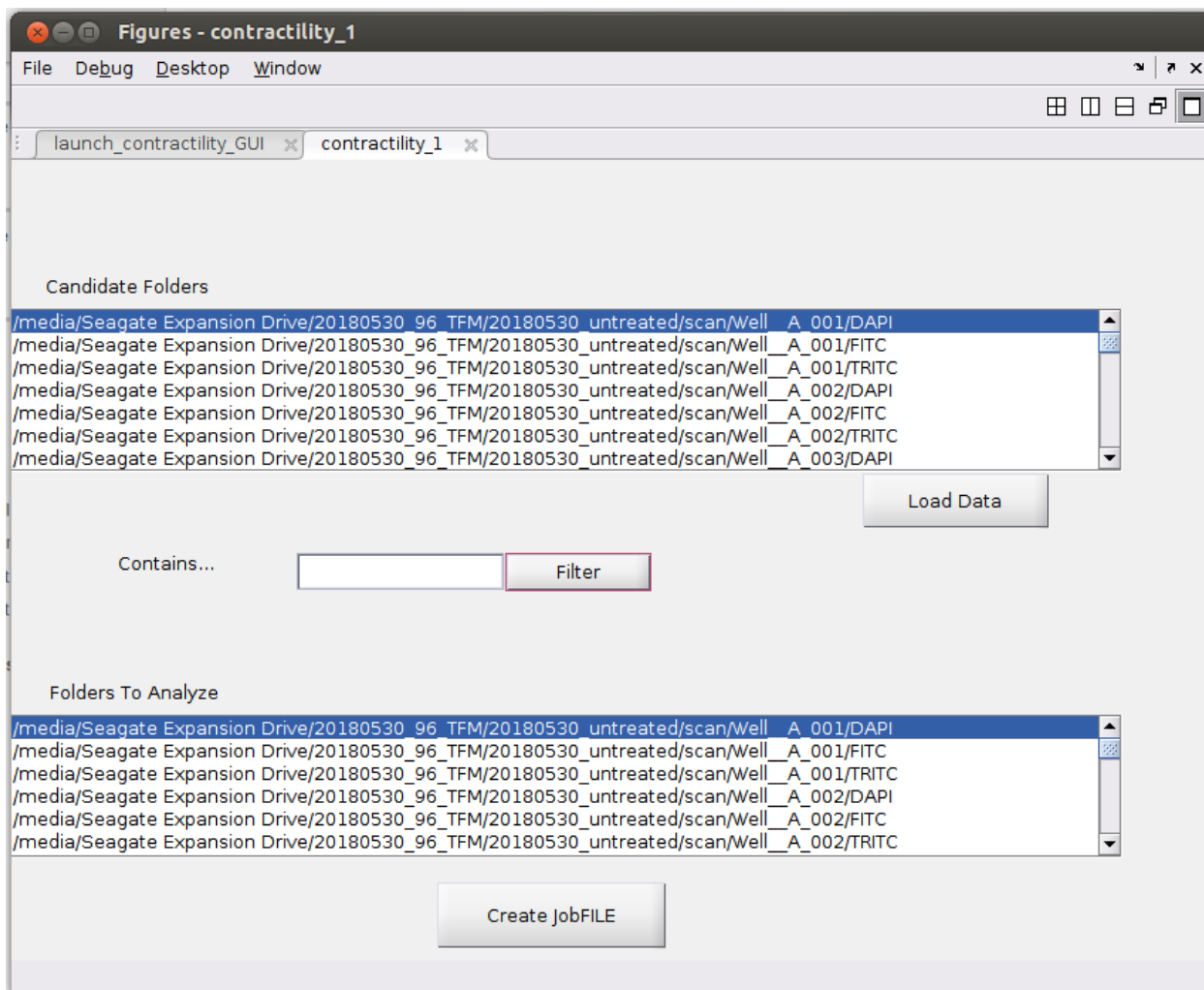


Figure 3.15: GUI to create a new job file.

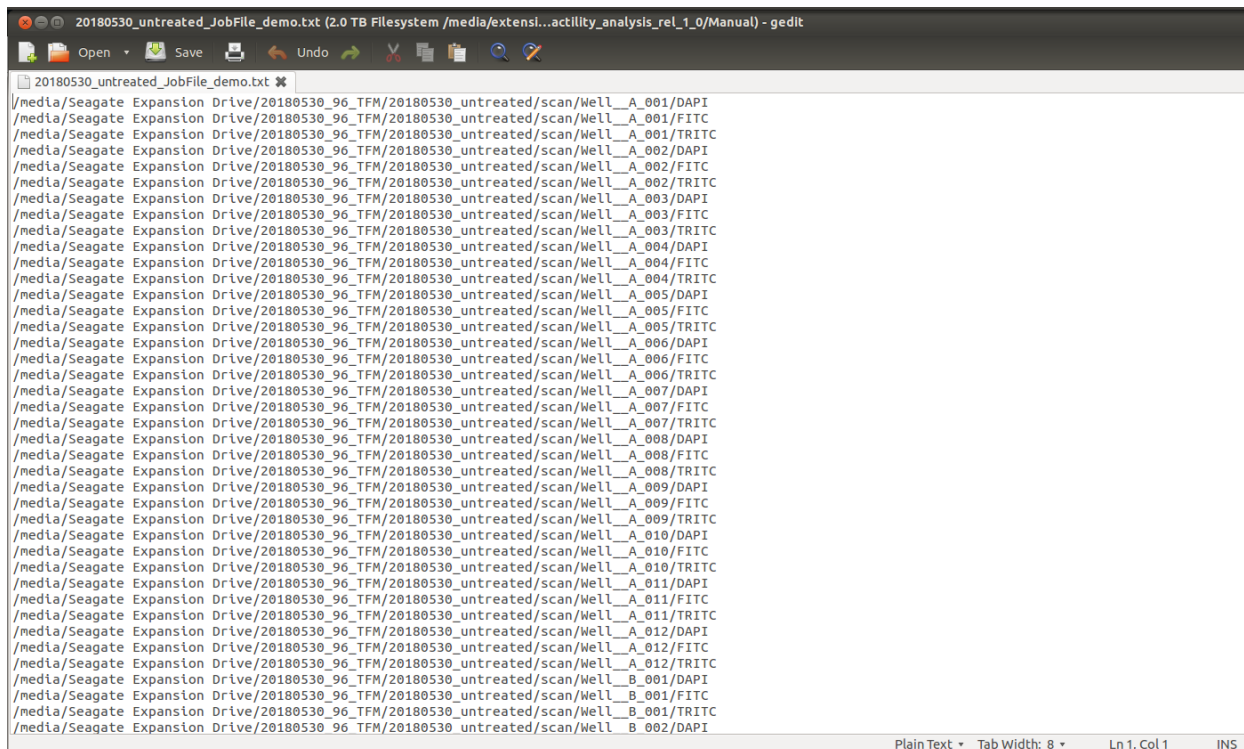


Figure 3.16: Sample of Job File.

those folders containing that string. If the user wants to analyze all of the listed folders, just leave the "Filter" box blank and click the button.

Now all of the matching folders should appear in the "Folders to Analyze" text box. If the user agrees with that list, click "Create Job File". A new dialog will ask the user to save the job file. The job file can be reviewed and edited with any standard simple-text editor such as Wordpad in Windows or TextEdit in Mac (Figure 3.16). Once the jobfile has been successfully created, close the job file GUI.

## Creating a Configuration File

Next the user must create a configuration file. The configuration file contains information about how the analysis must be run. Currently CCA, only executes the contractility analysis based on the divergence of deformation fields. Future versions will include options to execute Dynamic Monolayer Force Microscopy and elastography.

The configuration dialog (Figure 3.17) opens when the user clicks "New" in the main

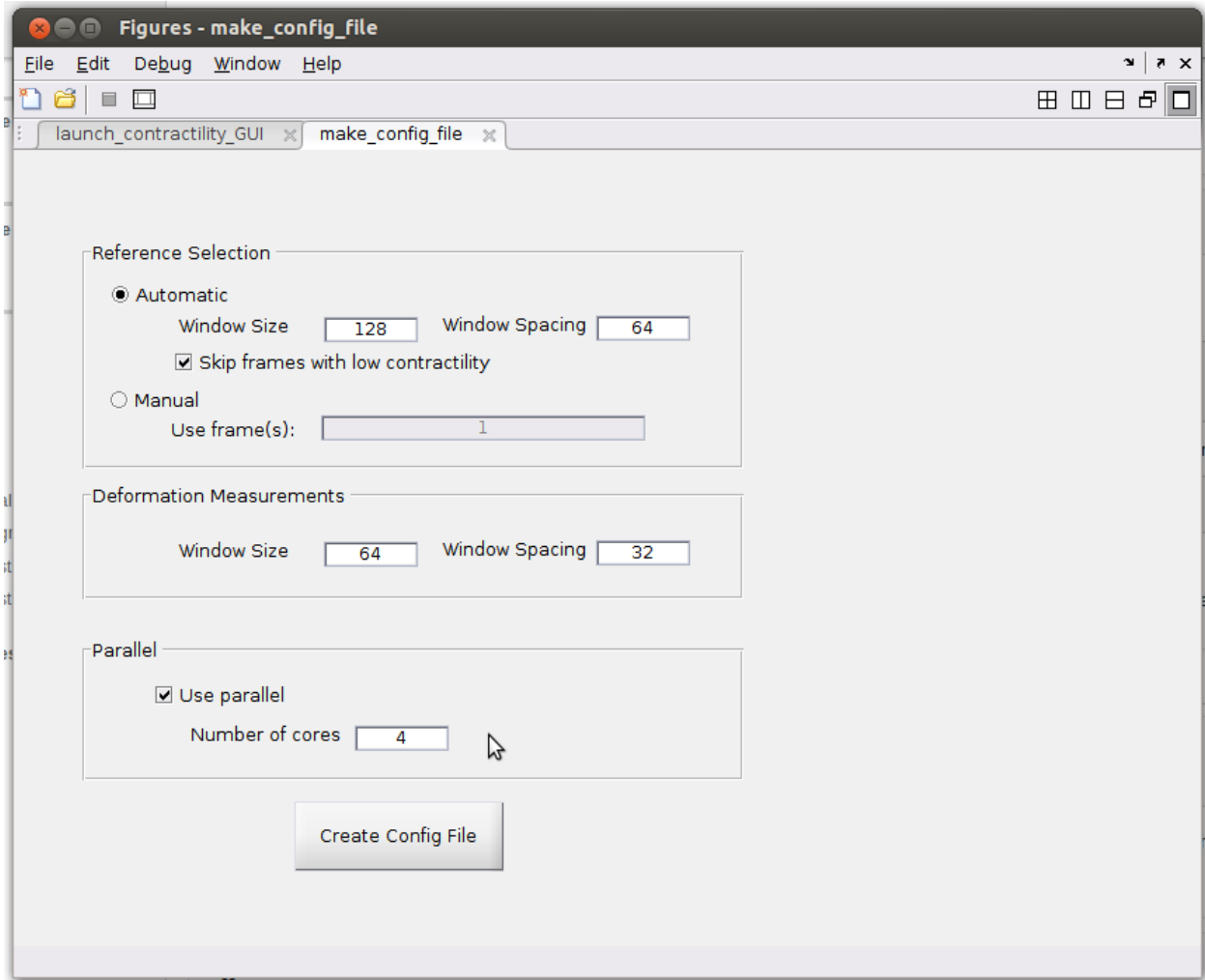


Figure 3.17: GUI to create a new configuration file.

many from CCA. The meaning of each field is explained below:

### 1. Reference Selection

- Automatic: Automatic reference selection should be used when the user does not know in what frames the cells are in a relaxed state.
  - Window Size: size of the PIV window for creating velocity signal. Recommended value of twice the size of the window for Deformation Measurements.
  - Window spacing: spacing of the PIV window for creating velocity signal. Recommended value: half of the Window Size.

- Skip frames with low contractility: Allow CCA to skip the Deformation Measurements on those frames where the cells are at rest.
- Manual: Manually choose what are the reference frames that should be used for the Deformation Measurements. NOTE: in the current version all the folders listed in the jobfile will be analyzed with the same frame index. For instance, if the user chooses '1', all the Deformations will be computed using the first frame of the folder as reference frame.

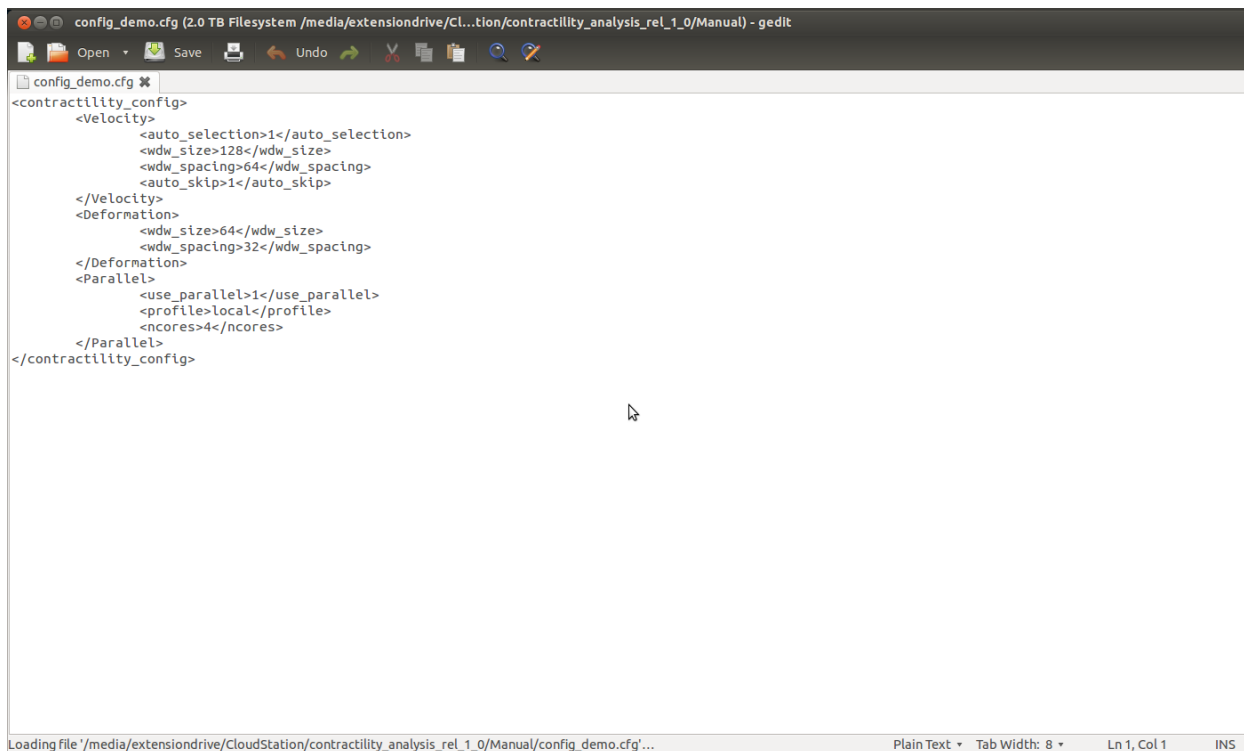
## 2. Deformation Measurements

- Window Size: size of the PIV window for Deformation Measurements. The optimal value for the window size depends on experimental factors. We encourage to test different values and look for contractility signals that provide a good trade-off between noise and peak amplitude.
- Window spacing: spacing of the PIV window for Deformation Measurements. Recommended value: half of the Window Size.

## 3. Parallel

- Use parallel: Selection enables CCA to run on multiple processors.
- Number of cores: Number of Matlab workers (tasks/processes) on which CCA will be executed. Currently CCA can only operate with the default parallel options of Matlab Runtime. The maximum number of workers is that of the number of physical cores of the system. NOTE: A hyperthreaded core will only be counted as one core, although the Operating System may list them as two.

After selecting the desired options, the user must click "Create Config File", and save the configuration file. The configuration file can be reviewed and edited with any standard simple-text editor such as Wordpad in Windows or TextEdit in Mac (Figure 3.18). Once the configuration file has been successfully created, close the dialog to return to CCA's main menu.



```
config_demo.cfg (2.0 TB Filesystem /media/extensiondrive/CloudStation/contractility_analysis_rel_1_0/Manual) - gedit
<contractility_config>
  <Velocity>
    <auto_selection>1</auto_selection>
    <wdw_size>128</wdw_size>
    <wdw_spacing>64</wdw_spacing>
    <auto_skip>1</auto_skip>
  </Velocity>
  <Deformation>
    <wdw_size>64</wdw_size>
    <wdw_spacing>32</wdw_spacing>
  </Deformation>
  <Parallel>
    <use_parallel>1</use_parallel>
    <profile>local</profile>
    <ncores>4</ncores>
  </Parallel>
</contractility_config>
```

Figure 3.18: Sample of Config File.

## Creating an Alias File

The alias file is a list that matches, one by one, the entries of the job file. The alias file provides a short unique name -an alias- for all the traces generated by CCA. The name of the alias file must match the name of the job file preceded by with the string "Alias\_" Example: "Jobfile.txt" and "Alias\_Example.txt". CCA provides a function to easily create aliases based on the folder hierarchy (Figure 3.19). In this example, we may want to use the last 2 levels of subfolders to create a unique identifier for each condition. One of the levels contains the information regarding the well where the video was taken from "Well\_X\_####". The next level contains the name of the fluorescent channel used for the image acquisition "DAPI", "FITC" or "TRITC".

We recommend to use the least amount of levels possible to keep the alias length easy to read (Figure 3.20). However, it is very important that all the experiments should have a unique alias, otherwise the trace images would be overwritten in the output folder.



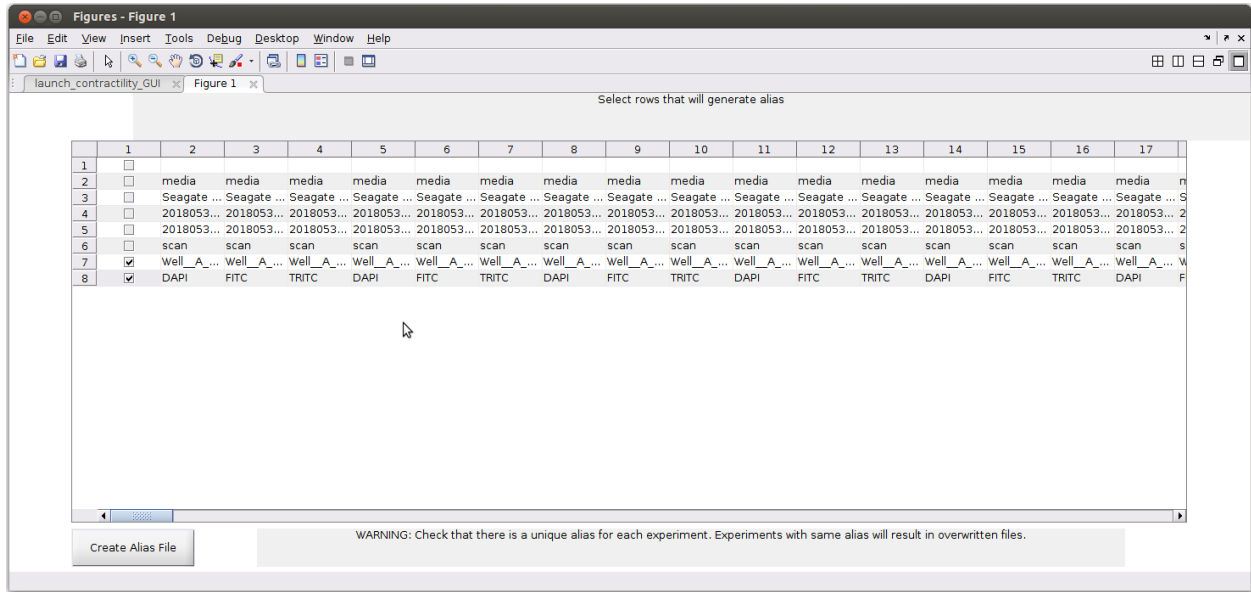


Figure 3.19: GUI to create an alias file.

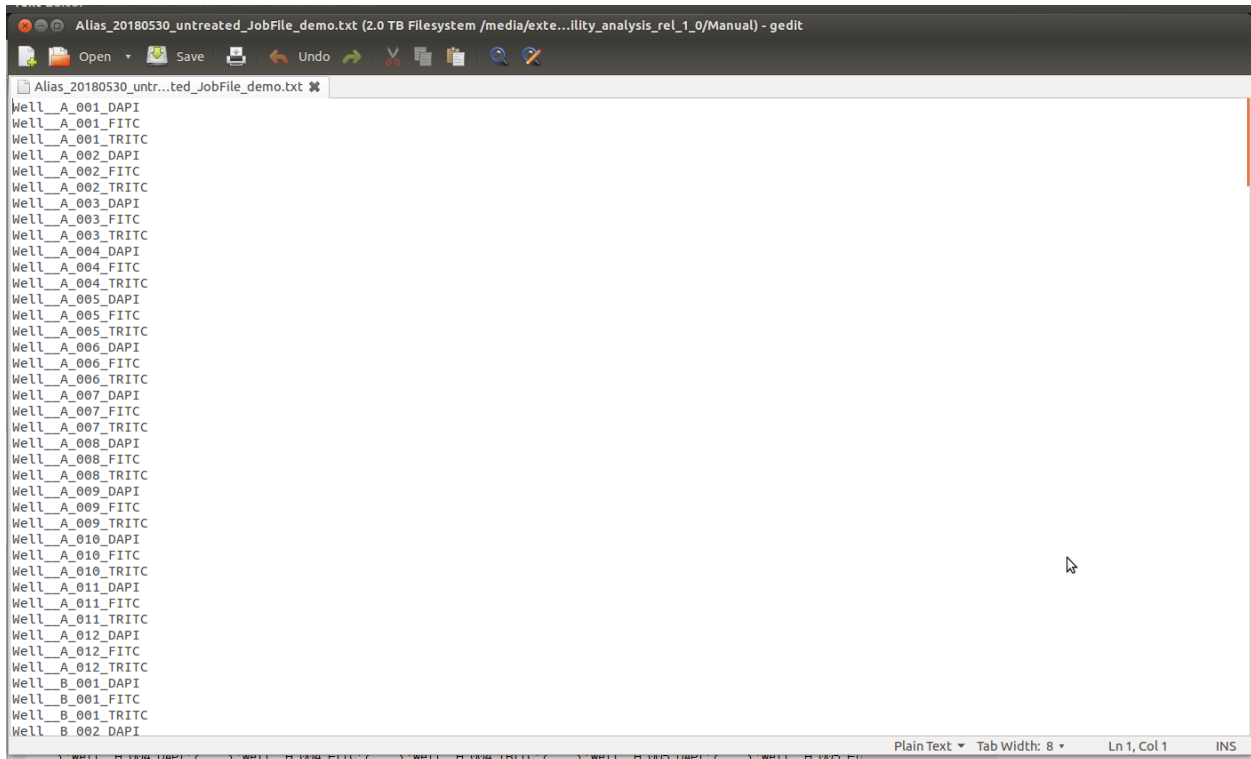


Figure 3.20: Sample of alias file.

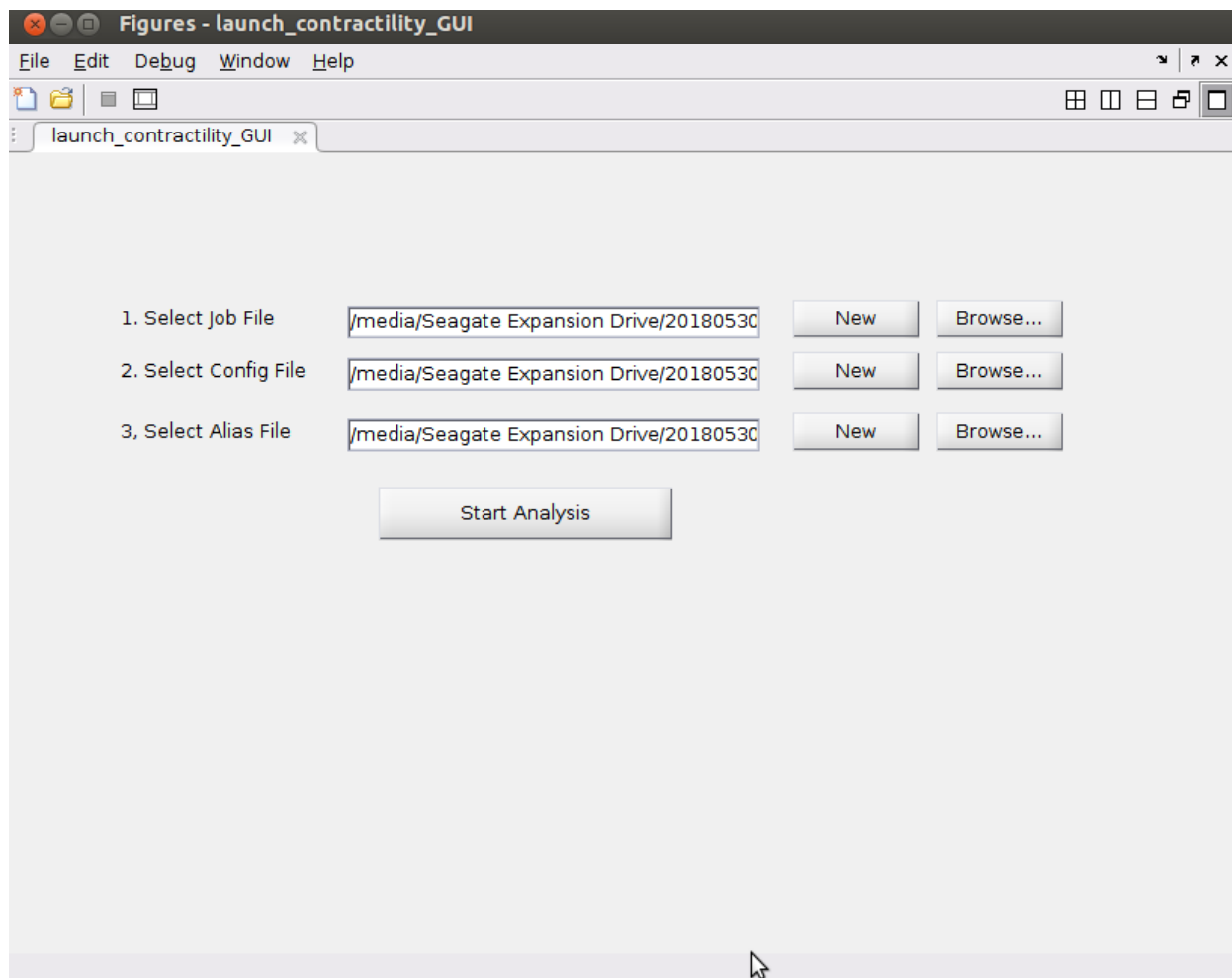


Figure 3.21: Main menu of CCA ready to start the analysis.

## Executing the Analysis

Once the job, configuration, and alias files have been created, the system is ready to start the analysis. The user may make sure that all the files are correctly listed in their respective fields (Figure 3.21). Then just click "Start Analysis".

## During Execution

During execution of CCA, several folders will be created in the same directory as the job file. The traces that CCA generates will appear in those folder as execution progresses. The contractility signals will be saved in the "raw" folder. The phase averaged peak annotated with the retrieved parameters will be stored in the "PA" folder. If CCA is running in

```
status_20180530_untreated_JobFile.txt.log
/media/ricardo/Seagate Expansion Drive/20180530_96_TFH/20180530_untreated/scan/Well_A_001/DAPI ERROR 19-Jul-2018 14:42:12
/media/ricardo/Seagate Expansion Drive/20180530_96_TFH/20180530_untreated/scan/Well_A_001/FITC COMPLETED 19-Jul-2018 14:48:35
/media/ricardo/Seagate Expansion Drive/20180530_96_TFH/20180530_untreated/scan/Well_A_001/TRITC COMPLETED 19-Jul-2018 14:55:10
/media/ricardo/Seagate Expansion Drive/20180530_96_TFH/20180530_untreated/scan/Well_A_002/DAPI ERROR 19-Jul-2018 14:55:10
/media/ricardo/Seagate Expansion Drive/20180530_96_TFH/20180530_untreated/scan/Well_A_002/FITC COMPLETED 19-Jul-2018 15:01:02
/media/ricardo/Seagate Expansion Drive/20180530_96_TFH/20180530_untreated/scan/Well_A_002/TRITC COMPLETED 19-Jul-2018 15:08:18
/media/ricardo/Seagate Expansion Drive/20180530_96_TFH/20180530_untreated/scan/Well_A_003/DAPI ERROR 19-Jul-2018 15:08:19
/media/ricardo/Seagate Expansion Drive/20180530_96_TFH/20180530_untreated/scan/Well_A_003/FITC COMPLETED 19-Jul-2018 15:14:14
/media/ricardo/Seagate Expansion Drive/20180530_96_TFH/20180530_untreated/scan/Well_A_003/TRITC COMPLETED 19-Jul-2018 15:21:10
/media/ricardo/Seagate Expansion Drive/20180530_96_TFH/20180530_untreated/scan/Well_A_004/DAPI ERROR 19-Jul-2018 15:21:10
/media/ricardo/Seagate Expansion Drive/20180530_96_TFH/20180530_untreated/scan/Well_A_004/FITC COMPLETED 19-Jul-2018 15:27:29
/media/ricardo/Seagate Expansion Drive/20180530_96_TFH/20180530_untreated/scan/Well_A_004/TRITC COMPLETED 19-Jul-2018 15:33:44
/media/ricardo/Seagate Expansion Drive/20180530_96_TFH/20180530_untreated/scan/Well_A_005/DAPI ERROR 19-Jul-2018 15:33:44
/media/ricardo/Seagate Expansion Drive/20180530_96_TFH/20180530_untreated/scan/Well_A_005/FITC COMPLETED 19-Jul-2018 15:39:36
/media/ricardo/Seagate Expansion Drive/20180530_96_TFH/20180530_untreated/scan/Well_A_005/TRITC COMPLETED 19-Jul-2018 15:45:52
/media/ricardo/Seagate Expansion Drive/20180530_96_TFH/20180530_untreated/scan/Well_A_006/DAPI ERROR 19-Jul-2018 15:45:52
/media/ricardo/Seagate Expansion Drive/20180530_96_TFH/20180530_untreated/scan/Well_A_006/FITC COMPLETED 19-Jul-2018 15:52:04
/media/ricardo/Seagate Expansion Drive/20180530_96_TFH/20180530_untreated/scan/Well_A_006/TRITC COMPLETED 19-Jul-2018 15:58:53
/media/ricardo/Seagate Expansion Drive/20180530_96_TFH/20180530_untreated/scan/Well_A_007/DAPI ERROR 19-Jul-2018 15:58:54
/media/ricardo/Seagate Expansion Drive/20180530_96_TFH/20180530_untreated/scan/Well_A_007/FITC COMPLETED 19-Jul-2018 16:05:10
/media/ricardo/Seagate Expansion Drive/20180530_96_TFH/20180530_untreated/scan/Well_A_007/TRITC COMPLETED 19-Jul-2018 16:11:49
/media/ricardo/Seagate Expansion Drive/20180530_96_TFH/20180530_untreated/scan/Well_A_008/DAPI ERROR 19-Jul-2018 16:11:49
/media/ricardo/Seagate Expansion Drive/20180530_96_TFH/20180530_untreated/scan/Well_A_008/FITC COMPLETED 19-Jul-2018 16:17:50
/media/ricardo/Seagate Expansion Drive/20180530_96_TFH/20180530_untreated/scan/Well_A_008/TRITC COMPLETED 19-Jul-2018 16:24:05
/media/ricardo/Seagate Expansion Drive/20180530_96_TFH/20180530_untreated/scan/Well_A_009/DAPI ERROR 19-Jul-2018 16:24:06
/media/ricardo/Seagate Expansion Drive/20180530_96_TFH/20180530_untreated/scan/Well_A_009/FITC COMPLETED 19-Jul-2018 16:30:05
/media/ricardo/Seagate Expansion Drive/20180530_96_TFH/20180530_untreated/scan/Well_A_009/TRITC COMPLETED 19-Jul-2018 16:36:48
/media/ricardo/Seagate Expansion Drive/20180530_96_TFH/20180530_untreated/scan/Well_A_010/DAPI ERROR 19-Jul-2018 16:36:48
/media/ricardo/Seagate Expansion Drive/20180530_96_TFH/20180530_untreated/scan/Well_A_010/FITC COMPLETED 19-Jul-2018 16:42:39
/media/ricardo/Seagate Expansion Drive/20180530_96_TFH/20180530_untreated/scan/Well_A_010/TRITC COMPLETED 19-Jul-2018 16:48:54
/media/ricardo/Seagate Expansion Drive/20180530_96_TFH/20180530_untreated/scan/Well_A_011/DAPI ERROR 19-Jul-2018 16:48:54
/media/ricardo/Seagate Expansion Drive/20180530_96_TFH/20180530_untreated/scan/Well_A_011/FITC COMPLETED 19-Jul-2018 16:55:11
/media/ricardo/Seagate Expansion Drive/20180530_96_TFH/20180530_untreated/scan/Well_A_011/TRITC COMPLETED 19-Jul-2018 17:01:08
/media/ricardo/Seagate Expansion Drive/20180530_96_TFH/20180530_untreated/scan/Well_A_012/DAPI ERROR 19-Jul-2018 17:01:09
/media/ricardo/Seagate Expansion Drive/20180530_96_TFH/20180530_untreated/scan/Well_A_012/FITC COMPLETED 19-Jul-2018 17:07:01
/media/ricardo/Seagate Expansion Drive/20180530_96_TFH/20180530_untreated/scan/Well_A_012/TRITC COMPLETED 19-Jul-2018 17:13:18
/media/ricardo/Seagate Expansion Drive/20180530_96_TFH/20180530_untreated/scan/Well_B_001/DAPI ERROR 19-Jul-2018 17:13:19
/media/ricardo/Seagate Expansion Drive/20180530_96_TFH/20180530_untreated/scan/Well_B_001/FITC COMPLETED 19-Jul-2018 17:19:39
/media/ricardo/Seagate Expansion Drive/20180530_96_TFH/20180530_untreated/scan/Well_B_001/TRITC COMPLETED 19-Jul-2018 17:25:52
/media/ricardo/Seagate Expansion Drive/20180530_96_TFH/20180530_untreated/scan/Well_B_002/DAPI ERROR 19-Jul-2018 17:25:53
```

Figure 3.22: Example of a status file.

automatic reference mode, the velocity signals will be saved in the "vel" folder.

In order to keep track of the status of the execution, CCA will generate a status file on the same location as the jobfile (Figure 3.22). The status file will show a list of directories like the job file but at the end will show either "queued", "COMPLETED", or "ERROR". In this example, the "DAPI" only contained one image of the nuclei of the cells. CCA throws an error because it can't execute PIV, which needs a minimum of 2 images but the execution continues to the next directory in the job file.

## Exporting the Results

After analyzing all the experiments listed in the jobfile, CCA creates a comma separated value file named "CCA\_results.csv" (Figure 3.23) that contains the retrieved phase average parameters from each experiment. The .csv file can be easily imported to many other programs that will facilitate further data mining of the results of CCA such as plotting dose response curves. Note that some parameters may be missing for a specific experiment

Well	T peak	T rise	T fall	TCT	D peak	D valley	D high	D low	AUC	Power	CR
/media/ricardo/Seagate Expansion Drive/20180530_96_TFM/20180530_untreated/scan/Well_A_001/DAPI	Not Computi	Not Computi	Not Computi	Not Computi	Not Computi	Not Computi	Not Computi	Not Computi	Not Computi	Not Computi	Not Computi
/media/ricardo/Seagate Expansion Drive/20180530_96_TFM/20180530_untreated/scan/Well_A_001/FITC	0.7463	0.066851	0.13413	0.32652	0.029296	0.00070491	0.025008	0.0049936	0.0064917	0.0086986	0.388
/media/ricardo/Seagate Expansion Drive/20180530_96_TFM/20180530_untreated/scan/Well_A_001/TRITC	0.7264	0.066464	0.1599	0.35501	0.02904	0.00036847	0.024739	0.0046692	0.0068202	0.0093891	0.3
/media/ricardo/Seagate Expansion Drive/20180530_96_TFM/20180530_untreated/scan/Well_A_002/DAPI	Not Computi	Not Computi	Not Computi	Not Computi	Not Computi	Not Computi	Not Computi	Not Computi	Not Computi	Not Computi	Not Computi
/media/ricardo/Seagate Expansion Drive/20180530_96_TFM/20180530_untreated/scan/Well_A_002/FITC	0.97017	0.085854	0.11251	0.31466	0.012938	0.00065552	0.011096	0.0024979	0.0027972	0.0028832	0.128
/media/ricardo/Seagate Expansion Drive/20180530_96_TFM/20180530_untreated/scan/Well_A_002/TRITC	0.97017	0.072137	0.10876	0.31734	0.0094778	0.00033812	0.0081068	0.0017991	0.0021689	0.0022356	0.114
/media/ricardo/Seagate Expansion Drive/20180530_96_TFM/20180530_untreated/scan/Well_A_003/DAPI	Not Computi	Not Computi	Not Computi	Not Computi	Not Computi	Not Computi	Not Computi	Not Computi	Not Computi	Not Computi	Not Computi
/media/ricardo/Seagate Expansion Drive/20180530_96_TFM/20180530_untreated/scan/Well_A_003/FITC	0.85077	0.066344	0.10489	0.29249	0.016359	0.00067556	0.014006	0.003028	0.0033596	0.0039489	0.204
/media/ricardo/Seagate Expansion Drive/20180530_96_TFM/20180530_untreated/scan/Well_A_003/TRITC	0.8458	0.063643	0.10764	0.30361	0.014419	0.00038046	0.012133	0.0024863	0.0031671	0.0037445	0.204
/media/ricardo/Seagate Expansion Drive/20180530_96_TFM/20180530_untreated/scan/Well_A_004/DAPI	Not Computi	Not Computi	Not Computi	Not Computi	Not Computi	Not Computi	Not Computi	Not Computi	Not Computi	Not Computi	Not Computi
/media/ricardo/Seagate Expansion Drive/20180530_96_TFM/20180530_untreated/scan/Well_A_004/FITC	0.9652	0.089258	0.21194	0.41594	0.014246	0.00065405	0.012207	0.0026928	0.0033791	0.0035009	0.152
/media/ricardo/Seagate Expansion Drive/20180530_96_TFM/20180530_untreated/scan/Well_A_004/TRITC	0.95027	0.071005	0.11093	0.30896	0.0084083	0.00033501	0.0071973	0.001546	0.001794	0.0018878	0.097
/media/ricardo/Seagate Expansion Drive/20180530_96_TFM/20180530_untreated/scan/Well_A_005/DAPI	Not Computi	Not Computi	Not Computi	Not Computi	Not Computi	Not Computi	Not Computi	Not Computi	Not Computi	Not Computi	Not Computi
/media/ricardo/Seagate Expansion Drive/20180530_96_TFM/20180530_untreated/scan/Well_A_005/FITC	0.89057	0.071504	0.098634	0.29609	0.014504	0.0005559	0.012412	0.0026482	0.003062	0.0034382	0.174
/media/ricardo/Seagate Expansion Drive/20180530_96_TFM/20180530_untreated/scan/Well_A_005/TRITC	0.89057	0.067977	0.10349	0.30989	0.013521	0.00024611	0.01153	0.0022374	0.0030725	0.00345	0.177
/media/ricardo/Seagate Expansion Drive/20180530_96_TFM/20180530_untreated/scan/Well_A_006/DAPI	Not Computi	Not Computi	Not Computi	Not Computi	Not Computi	Not Computi	Not Computi	Not Computi	Not Computi	Not Computi	Not Computi
/media/ricardo/Seagate Expansion Drive/20180530_96_TFM/20180530_untreated/scan/Well_A_006/FITC	0.87067	0.066184	0.091255	0.27916	0.020431	0.00072048	0.017475	0.0036771	0.0040509	0.0046526	0.265
/media/ricardo/Seagate Expansion Drive/20180530_96_TFM/20180530_untreated/scan/Well_A_006/TRITC	0.86072	0.064894	0.096235	0.29947	0.019811	0.00027357	0.016881	0.003206	0.0044227	0.0051384	0.27
/media/ricardo/Seagate Expansion Drive/20180530_96_TFM/20180530_untreated/scan/Well_A_007/DAPI	Not Computi	Not Computi	Not Computi	Not Computi	Not Computi	Not Computi	Not Computi	Not Computi	Not Computi	Not Computi	Not Computi
/media/ricardo/Seagate Expansion Drive/20180530_96_TFM/20180530_untreated/scan/Well_A_007/FITC	0.78112	0.06292	0.090476	0.27163	0.014213	0.00068511	0.012184	0.0027143	0.0027075	0.0034661	0.194
/media/ricardo/Seagate Expansion Drive/20180530_96_TFM/20180530_untreated/scan/Well_A_007/TRITC	0.78112	0.060261	0.085444	0.26804	0.0070387	0.00034878	0.0060352	0.0013523	0.0013563	0.0017364	0.098
/media/ricardo/Seagate Expansion Drive/20180530_96_TFM/20180530_untreated/scan/Well_A_008/DAPI	Not Computi	Not Computi	Not Computi	Not Computi	Not Computi	Not Computi	Not Computi	Not Computi	Not Computi	Not Computi	Not Computi
/media/ricardo/Seagate Expansion Drive/20180530_96_TFM/20180530_untreated/scan/Well_A_008/FITC	0.91047	0.070825	0.10331	0.28793	0.014065	0.00052903	0.012034	0.0025594	0.0028162	0.0030931	0.165
/media/ricardo/Seagate Expansion Drive/20180530_96_TFM/20180530_untreated/scan/Well_A_008/TRITC	0.91545	0.064352	0.10661	0.29724	0.010279	0.00036725	0.0087919	0.001854	0.0021746	0.0023754	0.145
/media/ricardo/Seagate Expansion Drive/20180530_96_TFM/20180530_untreated/scan/Well_A_009/DAPI	Not Computi	Not Computi	Not Computi	Not Computi	Not Computi	Not Computi	Not Computi	Not Computi	Not Computi	Not Computi	Not Computi
/media/ricardo/Seagate Expansion Drive/20180530_96_TFM/20180530_untreated/scan/Well_A_009/FITC	0.8259	0.058552	0.10525	0.29181	0.021011	0.00056536	0.017944	0.0036322	0.0044562	0.0053956	0.305
/media/ricardo/Seagate Expansion Drive/20180530_96_TFM/20180530_untreated/scan/Well_A_009/TRITC	0.8259	0.058469	0.10554	0.29436	0.016629	0.00028507	0.014177	0.0027367	0.0036205	0.0043837	0.252
/media/ricardo/Seagate Expansion Drive/20180530_96_TFM/20180530_untreated/scan/Well_A_010/DAPI	Not Computi	Not Computi	Not Computi	Not Computi	Not Computi	Not Computi	Not Computi	Not Computi	Not Computi	Not Computi	Not Computi
/media/ricardo/Seagate Expansion Drive/20180530_96_TFM/20180530_untreated/scan/Well_A_010/FITC	0.92042	0.078137	0.10228	0.30309	0.010026	0.00066336	0.0086217	0.0020678	0.0020591	0.0022372	0.105
/media/ricardo/Seagate Expansion Drive/20180530_96_TFM/20180530_untreated/scan/Well_A_010/TRITC	0.92042	0.071748	0.11928	0.33229	0.0081784	0.0002512	0.0069893	0.0014403	0.001925	0.0020914	0.0994
/media/ricardo/Seagate Expansion Drive/20180530_96_TFM/20180530_untreated/scan/Well_A_011/DAPI	Not Computi	Not Computi	Not Computi	Not Computi	Not Computi	Not Computi	Not Computi	Not Computi	Not Computi	Not Computi	Not Computi
/media/ricardo/Seagate Expansion Drive/20180530_96_TFM/20180530_untreated/scan/Well_A_011/FITC	0.95027	0.071847	0.1048	0.30548	0.013628	0.00052927	0.011663	0.0024941	0.0029547	0.0031093	0.152
/media/ricardo/Seagate Expansion Drive/20180530_96_TFM/20180530_untreated/scan/Well_A_011/TRITC	0.9453	0.069567	0.10154	0.30878	0.011024	0.00040449	0.0094314	0.0019975	0.0024393	0.0025805	0.142

Figure 3.23: Example of CCA\_results.csv

if the PIV analysis or parameter retrieval process failed.

## 3.7 Acknowledgements

Chapter 3, in part is currently being prepared for submission for publication of the material. Serrano, Ricardo; McKeithan Wesley; Mercola, Mark; del Álamo, Juan C. The dissertation/thesis author was the primary investigator and author of this material.

# Chapter 4

## Concluding Remarks

A brief summary of the main conclusions achieved in this dissertation is presented in this chapter, a more detailed discussion can be found at the end of each chapter.

The collective build-up and transmission of cellular forces is essential to the understanding of many biological processes such as development, endothelial function and wound healing. The quantification of intracellular stress with Monolayer Stress Microscopy is delivering great advances in the basic understanding of these phenomena and poses great promise for functional screening of force generation in cardiac drug discovery. However, current MSM methods present a number of limitations: they assume that the monolayer only deforms laterally, introduce boundary artifacts at the edges of field of view, and are restricted to low-throughput applications. This dissertation has addressed these limitations and has provided the first quantification of intracellular stresses in relevant problems of biology and biotechnology, ranging from leukocyte extravasation to high-throughput functional screening of cardiomyocytes.

The three dimensionality of cellular forces is apparent in a diverse series of biological problems. For example, leukocytes undergoing endothelial transmigration generate mechanical forces that bend the endothelium at the transmigration site [19]. Furthermore, epithelial bending and invagination driven by mechanical forces play a key role in the development of most tissues and organs [60]. However, there is a lack of experimental data about the contribution of bending to intracellular tension, and also about the propagation of this me-

chanical signal throughout monolayers. Chapter 2 of this dissertation has provided with an extension of MSM to account for bending deformations of the cell monolayer. The inputs to the extended 3-D MSM method are the 3-D traction stresses at the interface between the cell monolayer and its substratum, i.e.  $[\tau_{xz}(x, y), \tau_{xz}(x, y), \tau_{zz}(x, y)]$ , which requires interrogating the 3-D deformation of the substrate in a thin volumetric slice near the surface of the substrate [36]. Similar to traction force microscopy, where global force balance yields an integral constraint for the measured deformations (i.e. zero average displacement) [51], global balance of bending moments leads to an additional constraint (i.e. zero average tilt). Given that the image processing algorithm for measuring substrate deformation involves the optimization of image cross-correlation, the constraints can be incorporated during image processing instead of during stress recovery. This approach is advantageous since it adapts the weight of the constraints in each region of the image according to its local signal to noise ratio, and it generally yields more realistic displacement measurements.

In epithelial cell sheets, the intracellular stresses caused by lateral cell contractility have been shown to propagate over distances much longer than the size of a single cell, and to contribute to collective mechanosensing [66]. However, the propagation of intracellular stresses caused by normal contractility has not been explored systematically so far. To address this question, we applied 3D MSM to confluent micropatterned cell islands of different shapes and sizes, and obtained the first measurements of intracellular tension caused by out-of-plane traction stresses. These measurements revealed that the magnitude of bending intracellular tension can exceed that of the tension caused by lateral contractility near the edges of a cell monolayer, particularly in regions of high edge curvature like corners. We also found that the internal stresses caused by bending do not propagate as far as the internal stresses caused by lateral contractility, and tend to balance out within a few ( $\sim 1$ ) cell lengths into the monolayer. This concentrated effect may be relevant for phenomena like cellular extravasation, which are accompanied by significant normal deflections of the endothelial monolayer, and which require spatially regulated changes in endothelial permeability [20, 67].

Chapter 2 of this dissertation has provided with an extension of MSM to account for bending deformations of the cell monolayer. An additional novelty of this method is that

the MSM equations were discretized numerically on a Cartesian grid using Fourier series and the boundary conditions at the edges of the monolayer were imposed via a level-set immersed interface method. Our results indicate that intracellular stresses caused by lateral deformation are transmitted across long distances, whereas bending-induced stresses remain confined to 1-2 cell lengths from bending sites. We hypothesize that the localized effect of bending-induced stresses may be important in processes such as cellular extravasation, which are accompanied by significant normal deflections of the endothelium and require localized changes in its permeability. Overall, these results suggest that bending and lateral stresses can propagate mechanical signals at different length scales, and reveal that the transmission of forces across cell junctions is three-dimensional and more complex than previously believed.

Functional screening assays of contractile force generation of iPS-CM promise great potential for new cardiac drug discovery, drug cardiotoxicity, and in vitro modeling of cardiac disease [31]. However, existing high-throughput assays for cardiac contractility rely on the measurement of surrogate variables such as the motion of the cells, and changes in the intensity of the image [73–75]. Moreover, all these assays have been realized on a stiff surface such as glass or plastic. In contrast, substrate stiffness is a feature that has proven to be of relevance, especially for iPS-CM maturity [78]. Monolayer Stress Microscopy is a powerful tool for the quantification of collective force generation and transmission but the requirement of fabricating flexible substrates make its high-throughput implementation challenging. In addition to force assays, there is a lack of functional assays that aim to quantify cardiomyocyte stiffness. The absence of stiffness-based assays contrasts with the increasing interest in myocardial mechanical properties [83], which has been associated with cardiac diseases affecting the heart’s relaxation during diastole [80].

In this dissertation we presented a protocol to manufacture SBS compatible 96 well plates with polyacrylamide gels that can be imaged with any standard High Content Screening system, enabling the realization of MSM measurements in high-throughput. The stiffness of the gels of our device can be tuned by changing the ratio of acrylamide and bis-acrylamide or, alternatively, the UV curing time, as shown before by other groups [49, 87].



We developed automatized reference selection algorithms to remove the need of manually selecting a reference frame for measuring deformations with PIV. The measured deformation maps of the polyacrylamide gels are further analyzed with MSM, yielding time-resolved two-dimensional maps of intracellular tension. The time-dependent contractility signal is defined as the spatial average magnitude of intracellular tension. From this signal we extract representative metrics such as magnitude and period of the signal as well as duration of contraction. These metrics are calculated for each well, providing a quick summary for each experimental condition. In addition to the deformations of the substrate, we also measured the deformations of the monolayer directly by adding fluorescently labeled WGA to live stain the cells's membrane. Following a process similar to that of the substrates, we were able to measure the deformation fields of the cells during contraction. The divergence of the deformation fields was calculated with direct differentiation, to obtain maps of local change of area. A contractility signal was calculated by taking the spatial average of the magnitude of the divergence field.

To illustrate an example of our analysis, we examined the variation of each metric with different concentrations of benchmark compounds. Our analysis was able to capture dose-dependent changes in frequency and amplitude of contraction caused by the compounds. The problem of variability in iPS-CM is well-known in the field. To overcome this difficulty, we imaged the device before adding the compounds, obtaining in this way internal control experiments of each plate, effectively reducing the noise caused by well-to-well variability and increasing the sensitivity of the analysis to drug-induced changes.

Finally, we examined experimental stress-strain curves obtained from comparing intracellular tension and divergence. This analysis allowed to estimate the average bulk modulus of the imaged region, providing a first-in-kind high-throughput force assay with elastographic capabilities. Additionally, the combined knowledge of substrate and cell deformations allowed to correct boundary artifacts that are inherent to MSM at the edge of the field of view.

# Bibliography

- [1] Carl-Philipp Heisenberg and Yohanns Bella-Árche. Forces in tissue morphogenesis and patterning. *Cell*, 153(5):948–962, August 2013.
- [2] Sussan Nourshargh and Ronen Alon. Leukocyte migration into inflamed tissues. *Immunity*, 41(5):694–707, November 2014.
- [3] Charla-Álne Guillot and Thomas Lecuit. Mechanics of epithelial tissue homeostasis and morphogenesis. *Science*, 340(6137):1185, June 2013.
- [4] M. Dembo and Y. L. Wang. Stresses at the cell-to-substrate interface during locomotion of fibroblasts. *Biophysical Journal*, 76(PMC1300203):2307–2316, April 1999.
- [5] J. P. Butler, I. M. Tolic-Norrelykke, B. Fabry, and J. J. Fredberg. Traction fields, moments, and strain energy that cells exert on their surroundings. *Am J Physiol Cell Physiol*, 282(3):C595–605, 2002.
- [6] U. S. Schwarz and J. R. Soine. Traction force microscopy on soft elastic substrates: A guide to recent computational advances. *Biochim Biophys Acta*, 1853(11 Pt B):3095–104, 2015.
- [7] Dennis E. Discher, David J. Mooney, and Peter W. Zandstra. Growth factors, matrices, and forces combine and control stem cells. *Science*, 324(5935):1673–1677, 2009.
- [8] S. Li, J. L. Guan, and S. Chien. Biochemistry and biomechanics of cell motility. *Annu Rev Biomed Eng*, 7:105–50, 2005.
- [9] Alexander D. Bershadsky, Nathalie Q. Balaban, and Benjamin Geiger. Adhesion-dependent cell mechanosensitivity. *Annu. Rev. Cell Dev. Biol.*, 19(1):677–695, August 2018.
- [10] B. Alvarez-Gonzalez, R. Meili, E. Bastounis, R. A. Firtel, J. C. Lasheras, and J. C. Del Alamo. Three-dimensional balance of cortical tension and axial contractility enables fast amoeboid migration. *Biophys J*, 108(4):821–32, 2015.

- [11] W. R. Legant, C. K. Choi, J. S. Miller, L. Shao, L. Gao, E. Betzig, and C. S. Chen. Multidimensional traction force microscopy reveals out-of-plane rotational moments about focal adhesions. *Proc Natl Acad Sci U S A*, 110(3):881–6, 2013.
- [12] Guillaume Charras and Alpha S. Yap. Tensile forces and mechanotransduction at cell-cell junctions. *Current Biology*, 28(8):R445–R457, April 2018.
- [13] Yanlan Mao and Buzz Baum. Tug of war—the influence of opposing physical forces on epithelial cell morphology. *Developmental Biology*, 401(1):92–102, May 2015.
- [14] S. S. Hur, J. C. del Alamo, J. S. Park, Y. S. Li, H. A. Nguyen, D. Teng, K. C. Wang, L. Flores, B. Alonso-Latorre, J. C. Lasheras, and S. Chien. Roles of cell confluency and fluid shear in 3-dimensional intracellular forces in endothelial cells. *Proceedings of the National Academy of Sciences of the United States of America*, 109(28):11110–5, 2012.
- [15] X. Trepats, M. R. Wasserman, T. E. Angelini, E. Millet, D. A. Weitz, J. P. Butler, and J. J. Fredberg. Physical forces during collective cell migration. *Nature Physics*, 5(6):426–430, 2009.
- [16] J. Zimmermann, R. L. Hayes, M. Basan, J. N. Onuchic, W. J. Rappel, and H. Levine. Intercellular stress reconstitution from traction force data. *Biophys J*, 107(3):548–54, 2014.
- [17] R. J. Hardy. Formulas for determining local properties in molecular-dynamics simulations - shock-waves. *Journal of Chemical Physics*, 76(1):622–628, 1982.
- [18] V. Nier, S. Jain, C. T. Lim, S. Ishihara, B. Ladoux, and P. Marcq. Inference of internal stress in a cell monolayer. *Biophys J*, 110(7):1625–35, 2016.
- [19] Sui Huang and Donald E. Ingber. The structural and mechanical complexity of cell-growth control. *Nature Cell Biology*, 1:E131, September 1999.
- [20] Y.-T. Yeh, R. Serrano, J. Francois, J.-J. Chiu, Y.-S. J. Li, J. C. del Alamo, S. Chien, and J. Lasheras. The 3d forces exerted by leukocytes and vascular endothelial cells dynamically facilitate diapedesis. *Proceedings of the National Academy of Sciences of the United States of America*, 115(1):113–118, 2018.
- [21] D. T. Tambe, U. Croutelle, X. Trepats, C. Y. Park, J. H. Kim, E. Millet, J. P. Butler, and J. J. Fredberg. Monolayer stress microscopy: limitations, artifacts, and accuracy of recovered intercellular stresses. *PLoS One*, 8(2):e55172, 2013.
- [22] Jean-Louis Martiel, Aldo Leal, Laetitia Kurawawa, Martial Balland, Irene Wang, Timothée Vignaud, Qingzong Tseng, Manuel ThÃ©ry, and Ewa K. Paluch. Chapter 15 - measurement of cell traction forces with imagej. In *Methods in Cell Biology*, volume 125, pages 269–287. Academic Press, January 2015.

- [23] Michael R. Zile, Catalin F. Baicu, John S. Ikonomidis, Robert E. Stroud, Paul J. Nietert, Amy D. Bradshaw, Rebecca Slater, Bradley M. Palmer, Peter Van Buren, Markus Meyer, Margaret M. Redfield, David A. Bull, Henk L. Granzier, and Martin M. LeWinter. Myocardial stiffness in patients with heart failure and a preserved ejection fraction: contributions of collagen and titin. *Circulation*, 131:1247–59, Apr 2015.
- [24] Tatyana G. Kuznetsova, Maria N. Starodubtseva, Nicolai I. Yegorenkov, Sergey A. Chizhik, and Renat I. Zhdanov. Atomic force microscopy probing of cell elasticity. *Micron*, 38(8):824–833, December 2007.
- [25] Andreas R. Bausch, Winfried MÄüller, and Erich Sackmann. Measurement of local viscoelasticity and forces in living cells by magnetic tweezers. *Biophysical Journal*, 76(1):573–579, January 1999.
- [26] Yogesh K. Mariappan, Kevin J. Glaser, and Richard L. Ehman. Magnetic resonance elastography: A review. *Clinical anatomy (New York, N.Y.)*, 23(PMC3066083):497–511, July 2010.
- [27] Rosa M. S. Sigrist, Joy Liau, Ahmed El Kaffas, Maria Cristina Chammas, and Juer-gen K. Willmann. Ultrasound elastography: Review of techniques and clinical applica-tions. *Theranostics*, 7(PMC5399595):1303–1329, January 2017.
- [28] T. Mammoto and D. E. Ingber. Mechanical control of tissue and organ development. *Development*, 137(9):1407–20, 2010.
- [29] S. Chien. Mechanotransduction and endothelial cell homeostasis: the wisdom of the cell. *Am J Physiol Heart Circ Physiol*, 292(3):H1209–24, 2007.
- [30] Adam J. Singer and Richard A.F. Clark. Cutaneous wound healing. *New England Journal of Medicine*, 341(10):738–746, 1999.
- [31] J. C. del Alamo, D. Lemons, R. Serrano, A. Savchenko, F. Cerignoli, R. Bodmer, and M. Mercola. High throughput physiological screening of ipsc-derived cardiomyocytes for drug development. *Biochim Biophys Acta*, 1863(7 Pt B):1717–27, 2016.
- [32] A. Sharma, P. W. Burridge, W. L. McKeithan, R. Serrano, P. Shukla, N. Sayed, J. M. Churko, T. Kitani, H. Wu, A. Holmstrom, E. Matsa, Y. Zhang, A. Kumar, A. C. Fan, J. C. Del Alamo, S. M. Wu, J. J. Moslehi, M. Mercola, and J. C. Wu. High-throughput screening of tyrosine kinase inhibitor cardiotoxicity with human induced pluripotent stem cells. *Sci Transl Med*, 9(377), 2017.
- [33] M. Moussus, C. der Loughian, D. Fuard, M. Courcon, D. Gulino-Debrac, H. Delanoë-Ayari, and A. Nicolas. Intracellular stresses in patterned cell assemblies. *Soft Matter*, 10(14):2414–23, 2014.

- [34] S. Timoshenko and J.N. Goodier. *Theory of elasticity*. McGraw-Hill, 1969.
- [35] J. Notbohm, J. H. Kim, A. R. Asthagiri, and G. Ravichandran. Three-dimensional analysis of the effect of epidermal growth factor on cell-cell adhesion in epithelial cell clusters. *Biophys J*, 102(6):1323–30, 2012.
- [36] A. M. Zenkour and D. S. Mashat. Exact solutions for variable-thickness inhomogeneous elastic plates under various boundary conditions. *Meccanica*, 44(4):433–447, 2009.
- [37] J. C. del Alamo, R. Meili, B. Alonso-Latorre, J. Rodriguez-Rodriguez, A. Aliseda, R. A. Firtel, and J. C. Lasheras. Spatio-temporal analysis of eukaryotic cell motility by improved force cytometry. *Proc Natl Acad Sci U S A*, 104(33):13343–8, 2007.
- [38] J. C. del Alamo, R. Meili, B. Alvarez-Gonzalez, B. Alonso-Latorre, E. Bastounis, R. Firtel, and J. C. Lasheras. Three-dimensional quantification of cellular traction forces and mechanosensing of thin substrata by fourier traction force microscopy. *PLoS One*, 8(9):e69850, 2013.
- [39] Zhilin Li. An overview of the immersed interface method and its applications. *Taiwanese journal of mathematics*, pages 1–49, 2003.
- [40] R. Sunyer, V. Conte, J. Escribano, A. Elosegui-Artola, A. Labernadie, L. Valon, D. Navajas, J. M. Garcia-Aznar, J. J. Munoz, P. Roca-Cusachs, and X. Trepat. Collective cell durotaxis emerges from long-range intercellular force transmission. *Science*, 353(6304):1157–1161, 2016.
- [41] A. Aung, Y. N. Seo, S. Lu, Y. Wang, C. Jamora, J. C. del Alamo, and S. Varghese. 3d traction stresses activate protease-dependent invasion of cancer cells. *Biophys J*, 107(11):2528–37, 2014.
- [42] S. Khuon, L. Liang, R. W. Dettman, P. H. Sporn, R. B. Wysolmerski, and T. L. Chew. Myosin light chain kinase mediates transcellular intravasation of breast cancer cells through the underlying endothelial cells: a three-dimensional fret study. *J Cell Sci*, 123(Pt 3):431–40, 2010.
- [43] Nicolas Carpi, Matthieu Piel, Ammar Azioune, and Jenny Fink. Micropatterning on glass with deep uv. *Nature Protocol Exchange.*, 2011.
- [44] R. Meili, B. Alonso-Latorre, J. C. del Alamo, R. A. Firtel, and J. C. Lasheras. Myosin ii is essential for the spatiotemporal organization of traction forces during cell motility. *Mol Biol Cell*, 21(3):405–17, 2010.
- [45] B. Alonso-Latorre, J. C. Del Alamo, R. Meili, R. A. Firtel, and J. C. Lasheras. An oscillatory contractile pole-force component dominates the traction forces exerted by migrating amoeboid cells. *Cell Mol Bioeng*, 4(4):603–615, 2011.

- [46] E. Bastounis, R. Meili, B. Alvarez-Gonzalez, J. Francois, J. C. del Alamo, R. A. Firtel, and J. C. Lasheras. Both contractile axial and lateral traction force dynamics drive amoeboid cell motility. *J Cell Biol*, 204(6):1045–61, 2014.
- [47] E. Bastounis, B. Alvarez-Gonzalez, J. C. del Alamo, J. C. Lasheras, and R. A. Firtel. Cooperative cell motility during tandem locomotion of amoeboid cells. *Mol Biol Cell*, 27(8):1262–71, 2016.
- [48] B. Alvarez-Gonzalez, S. Zhang, M. Gomez-Gonzalez, R. Meili, R. A. Firtel, J. C. Lasheras, and J. C. Del Alamo. Two-layer elastographic 3-d traction force microscopy. *Sci Rep*, 7:39315, 2017.
- [49] J. R. Tse and A. J. Engler. Preparation of hydrogel substrates with tunable mechanical properties. *Curr Protoc Cell Biol*, Chapter 10:Unit 10 16, 2010.
- [50] Ronald J Adrian and Jerry Westerweel. *Particle image velocimetry*. Cambridge University Press, 2011.
- [51] M. Dembo, T. Oliver, A. Ishihara, and K. Jacobson. Imaging the traction stresses exerted by locomoting cells with the elastic substratum method. *Biophysical Journal*, 70(4):2008–2022, April 1996.
- [52] R. C. A. Eguiluz, K. B. Kaylan, G. H. Underhill, and D. E. Leckband. Substrate stiffness and ve-cadherin mechano-transduction coordinate to regulate endothelial monolayer integrity. *Biomaterials*, 140:45–57, 2017.
- [53] C. M. Nelson, R. P. Jean, J. L. Tan, W. F. Liu, N. J. Sniadecki, A. A. Spector, and C. S. Chen. Emergent patterns of growth controlled by multicellular form and mechanics. *Proceedings of the National Academy of Sciences of the United States of America*, 102(33):11594–11599, 2005.
- [54] A. C. Ugural. *Stresses in plates and shells*. McGraw-Hill, New York, 1981.
- [55] Y. Xu, W. C. Engl, E. R. Jerison, K. J. Wallenstein, C. Hyland, L. A. Wilen, and E. R. Dufresne. Imaging in-plane and normal stresses near an interface crack using traction force microscopy. *Proc Natl Acad Sci U S A*, 107(34):14964–7, 2010.
- [56] Y. C. Lin, D. T. Tambe, C. Y. Park, M. R. Wasserman, X. Trepap, R. Krishnan, G. Lenormand, J. J. Fredberg, and J. P. Butler. Mechanosensing of substrate thickness. *Phys Rev E Stat Nonlin Soft Matter Phys*, 82(4 Pt 1):041918, 2010.
- [57] K R Rushton. Dynamic-relaxation solutions of elastic-plate problems. *Journal of Strain Analysis*, 3(1):23–32, 1968.

- [58] S. Osher and R. Fedkiw. *Level Set Methods and Dynamic Implicit Surfaces*. Applied Mathematics Series. Springer, New York, 2003.
- [59] R. Serrano, W. L. McKeithan, M. Mercola, and J. C. del Alamo. High-throughput functional screening assay of force and stiffness in ipsc derived cardiomyocytes. *Biophysical Journal*, 114(3):312a–312a, 2018.
- [60] M. Thery. Micropatterning as a tool to decipher cell morphogenesis and functions. *Journal of Cell Science*, 123(24):4201–4213, 2010.
- [61] J. Zimmermann, B. A. Camley, W. J. Rappel, and H. Levine. Contact inhibition of locomotion determines cell-cell and cell-substrate forces in tissues. *Proc Natl Acad Sci U S A*, 113(10):2660–5, 2016.
- [62] Z. Liu, J. L. Tan, D. M. Cohen, M. T. Yang, N. J. Sniadecki, S. A. Ruiz, C. M. Nelson, and C. S. Chen. Mechanical tugging force regulates the size of cell-cell junctions. *Proc Natl Acad Sci U S A*, 107(22):9944–9, 2010.
- [63] Esther J. Pearl, Jingjing Li, and Jeremy B. A. Green. Cellular systems for epithelial invagination. *Philosophical Transactions of the Royal Society B: Biological Sciences*, 372(1720), 2017.
- [64] Nathan D Bade, Randall D Kamien, Richard K Assoian, and Kathleen J Stebe. Cell and stress fiber alignment are differentially controlled by curvature and rho activation. *Submitted*, 2017.
- [65] Nathan D. Bade, Tina Xu, Randall D. Kamien, Richard K. Assoian, and Kathleen J. Stebe. Gaussian curvature directs stress fiber orientation and cell migration. *Biophysical Journal*, 114(6):1467–1476, 2018.
- [66] P. Rodriguez-Franco, A. Bruges, A. Marin-Llaurado, V. Conte, G. Solanas, E. Batlle, J. J. Fredberg, P. Roca-Cusachs, R. Sunyer, and X. Trepate. Long-lived force patterns and deformation waves at repulsive epithelial boundaries. *Nat Mater*, 16(10):1029–1037, 2017.
- [67] E. C. Lessey-Morillon, L. D. Osborne, E. Monaghan-Benson, C. Guilluy, E. T. O’Brien, R. Superfine, and K. Burridge. The rhoa guanine nucleotide exchange factor, larg, mediates icam-1-dependent mechanotransduction in endothelial cells to stimulate transendothelial migration. *J Immunol*, 192(7):3390–8, 2014.
- [68] Y. Yoshida and S. Yamanaka. Induced pluripotent stem cells 10 years later: For cardiac applications. *Circ Res*, 120(12):1958–1968, 2017.

- [69] A. D. Ebert, P. Liang, and J. C. Wu. Induced pluripotent stem cells as a disease modeling and drug screening platform. *J Cardiovasc Pharmacol*, 60(4):408–16, 2012.
- [70] B. J. van Meer, L. G. Tertoolen, and C. L. Mummery. Concise review: Measuring physiological responses of human pluripotent stem cell derived cardiomyocytes to drugs and disease. *Stem Cells*, 34(8):2008–15, 2016.
- [71] N. J. Daily, R. Santos, J. Vecchi, P. Kemanli, and T. Wakatsuki. Calcium transient assays for compound screening with human ipsc-derived cardiomyocytes: Evaluating new tools. *J Evol Stem Cell Res*, 1(2):1–11, 2017.
- [72] X. Li, R. Zhang, B. Zhao, C. Lossin, and Z. Cao. Cardiotoxicity screening: a review of rapid-throughput in vitro approaches. *Arch Toxicol*, 90(8):1803–16, 2016.
- [73] L. Sala, B. J. van Meer, L. G. J. Tertoolen, J. Bakkers, M. Bellin, R. P. Davis, C. Denning, M. A. E. Dieben, T. Eschenhagen, E. Giacomelli, C. Grandela, A. Hansen, E. R. Holman, M. R. M. Jongbloed, S. M. Kamel, C. D. Koopman, Q. Lachaud, I. Mannhardt, M. P. H. Mol, D. Mosqueira, V. V. Orlova, R. Passier, M. C. Ribeiro, U. Saleem, G. L. Smith, F. L. Burton, and C. L. Mummery. Musclemotion: A versatile open software tool to quantify cardiomyocyte and cardiac muscle contraction in vitro and in vivo. *Circ Res*, 122(3):e5–e16, 2018.
- [74] T. Hayakawa, T. Kunihiro, T. Ando, S. Kobayashi, E. Matsui, H. Yada, Y. Kanda, J. Kurokawa, and T. Furukawa. Image-based evaluation of contraction-relaxation kinetics of human-induced pluripotent stem cell-derived cardiomyocytes: Correlation and complementarity with extracellular electrophysiology. *J Mol Cell Cardiol*, 77:178–91, 2014.
- [75] M. Maddah, J. D. Heidmann, M. A. Mandegar, C. D. Walker, S. Bolouki, B. R. Conklin, and K. E. Loewke. A non-invasive platform for functional characterization of stem-cell-derived cardiomyocytes with applications in cardiotoxicity testing. *Stem Cell Reports*, 4(4):621–31, 2015.
- [76] N. Huebsch, P. Loskill, M. A. Mandegar, N. C. Marks, A. S. Sheehan, Z. Ma, A. Mathur, T. N. Nguyen, J. C. Yoo, L. M. Judge, C. I. Spencer, A. C. Chukka, C. R. Russell, P. L. So, B. R. Conklin, and K. E. Healy. Automated video-based analysis of contractility and calcium flux in human-induced pluripotent stem cell-derived cardiomyocytes cultured over different spatial scales. *Tissue Eng Part C Methods*, 21(5):467–79, 2015.
- [77] A. J. Ribeiro, Y. S. Ang, J. D. Fu, R. N. Rivas, T. M. Mohamed, G. C. Higgs, D. Srivastava, and B. L. Pruitt. Contractility of single cardiomyocytes differentiated from pluripotent stem cells depends on physiological shape and substrate stiffness. *Proc Natl Acad Sci U S A*, 112(41):12705–10, 2015.



- [78] S. D. Boothe, J. D. Myers, S. Pok, J. Sun, Y. Xi, R. M. Nieto, J. Cheng, and J. G. Jacot. The effect of substrate stiffness on cardiomyocyte action potentials. *Cell Biochem Biophys*, 74(4):527–535, 2016.
- [79] C. Y. Park, E. H. Zhou, D. Tambe, B. Chen, T. Lavoie, M. Dowell, A. Simeonov, D. J. Maloney, A. Marinkovic, D. J. Tschumperlin, S. Burger, M. Frykenberg, J. P. Butler, W. D. Stamer, M. Johnson, J. Solway, J. J. Fredberg, and R. Krishnan. High-throughput screening for modulators of cellular contractile force. *Integr Biol (Camb)*, 7(10):1318–24, 2015.
- [80] D. Westermann, M. Kasner, P. Steendijk, F. Spillmann, A. Riad, K. Weitmann, W. Hoffmann, W. Poller, M. Pauschinger, H. P. Schultheiss, and C. Tschöpe. Role of left ventricular stiffness in heart failure with normal ejection fraction. *Circulation*, 117(16):2051–60, 2008.
- [81] W. A. Linke and N. Hamdani. Gigantic business: titin properties and function through thick and thin. *Circ Res*, 114(6):1052–68, 2014.
- [82] M. M. LeWinter and H. Granzier. Cardiac titin: a multifunctional giant. *Circulation*, 121(19):2137–45, 2010.
- [83] C. Y. Chen, M. A. Caporizzo, K. Bedi, A. Vite, A. I. Bogush, P. Robison, J. G. Heffler, A. K. Salomon, N. A. Kelly, A. Babu, M. P. Morley, K. B. Margulies, and B. L. Prosser. Suppression of deetyrosinated microtubules improves cardiomyocyte function in human heart failure. *Nat Med*, 2018.
- [84] D. Borin, I. Pecorari, B. Pena, and O. Sbaizero. Novel insights into cardiomyocytes provided by atomic force microscopy. *Semin Cell Dev Biol*, 73:4–12, 2018.
- [85] P. W. Burridge, E. Matsa, P. Shukla, Z. C. Lin, J. M. Churko, A. D. Ebert, F. Lan, S. Diecke, B. Huber, N. M. Mordwinkin, J. R. Plews, O. J. Abilez, B. Cui, J. D. Gold, and J. C. Wu. Chemically defined generation of human cardiomyocytes. *Nat Methods*, 11(8):855–60, 2014.
- [86] T. J. Cunningham, M. S. Yu, W. L. McKeithan, S. Spiering, F. Carrette, C. T. Huang, P. J. Bushway, M. Tierney, S. Albin, M. Giacca, M. Mano, P. L. Puri, A. Sacco, P. Ruiz-Lozano, J. F. Riou, M. Umbhauer, G. Duyster, M. Mercola, and A. R. Colas. Id genes are essential for early heart formation. *Genes Dev*, 31(13):1325–1338, 2017.
- [87] N. Ahmed, J. Schober, L. Hill, and S. P. Zustiak. Custom multiwell plate design for rapid assembly of photopatterned hydrogels. *Tissue Engineering Part C-Methods*, 22(6):543–551, 2016.